CJS-RE : un modèle constitutif hiérarchisée pour le matériau pisé

Winarputro Adi Riyono

N° d'ordre NNT: 2017LYSEC36 Année 2017

THÈSE

opérée au sein de l'Ecole centrale de Lyon

Ecole Doctorale No 162
(Mécanique-Energétique-Génie Civil-Acoustique)

Spécialité

Génie Civil

Soutenue publiquement le 6/10/2017, par:

Winarputro Adi RIYONO

CJS-RE: A HIERARCHICAL CONSTITUTIVE MODEL FOR RAMMED EARTH

Devant le jury composé de:

D. GALLIPOLI	Président/ Rapporteur	Professeur - Université de Pau-Pays de l'Adour
P.Y. HICHER	Rapporteur	Professeur - GEM, EC Nantes
P.B. LOURENCO	Examinateur	Professeur - Universidade do Minho
N. PRIME	Examinateur	Maître de Conférences - LOCIE, USMB
E. VINCENS	Directeur de thèse	Professeur - LTDS, EC Lyon
J.P. PLASSIARD	Co-encadrant	Maître de Conférences - LOCIE, USMB

In dedication to my parents for making me be who I am and my wife and son for support me all the way....

Liste des personnes habilitées à dirigées des recherches - École Centrale de Lyon

Ampère	BEROUAL Abderrahmane	professeur	ECL
	BURET François	professeur	ECL
	JAFFREZIC-RENAULT Nicole	directeur de recherche	ECL/CNRS
	KRAHENBUHL Laurent	directeur de recherche	ECL/CNRS
	NICOLAS Alain	professeur	ECL
	NICOLAS LAURENT	directeur de recherche	ECL/CNRS
	SCORLETTI Gérard	professeur	ECL
	SIMONET Pascal	directeur de recherche	ECL/CNRS
	VOLLAIRE Christian	professeur	ECL
DER EEA	HELLOUIN Yves	maître de conférences	ECL
DER STMS	GUIRALDENQ Pierre	professeur émérite	ECL
	VINCENT Léo	professeur	ECL
ICJ	LOHEAC Jean-Pierre	maître de conférence	ECL
	MAITRE Jean-François	professeur émérite	ECL
	MARION Martine	professeur	ECL
	MIRONESCU Elisabeth	professeur	ECL
	MOUSSAOUI Mohand	professeur	ECL
	MUSY François	maître de conférence	ECL
	ZINE Abdel-Malek	maître de conférence	ECL
ICTT	DAVID Bertrand	professeur	ECL

INL	CALLARD Anne-Ségolène	professeur	ECL
	CLOAREC Jean-Pierre	maître de conférence	ECL
	DANESCU Alexandre	maître de conférence	ECL
	GAFFIOT Frédéric	professeur	ECL
	GAGNAIRE Alain	maître de conférence	ECL
	GARRIGUES Michel	directeur de recherche	ECL/CNRS
	GENDRY Michel	directeur de recherche	ECL/CNRS
	GRENET Geneviève	directeur de recherche	ECL/CNRS
	HOLLINGER Guy	directeur de recherche	ECL/CNRS
	KRAWCZYK Stanislas	directeur de recherche	ECL/CNRS
	LETERTRE Xavier	chargé de recherche	ECL/CNRS
	O'CONNORR Ian	professeur	ECL
	PHANER-GOUTORBE Magali	professeur	ECL
	ROBACH Yves	professeur	ECL
	SAINT-GIRONS Guillaume	chargé de recherche	ECL/CNRS
	SEASSAL Christian	directeur de recherche	ECL/CNRS
	SOUTYRAND Eliane	directeur de recherche	ECL/CNRS
	TARDY Jacques	directeur de recherche	ECL/CNRS
	VIKTOROVITCH Pierre	directeur de recherche	ECL/CNRS
LIRIS	CHEN Liming	professeur	ECL
LMFA	BAILLY Christophe	professeur	ECL
	BERTOGLIO Jean-Pierre	directeur de recherche	ECL/CNRS
	BLANC-BENON Philippe	directeur de recherche	ECL/CNRS
	BOGEY Christophe	chargé de recherche	ECL/CNRS
	CAMBON Claude	directeur de recherche	ECL/CNRS
	CARRIERE Philippe	directeur de recherche	ECL/CNRS
	CHAMPOUSSIN Jean-Claude	professeur émérite	ECL
	COMPTE-BELLOT Genevièvre	professeur émérite	ECL
	FERRAND Pascal	directeur de recherche	ECL/CNRS
	GALLAND Marie-Annick	professeur	ECL
	GODEFERD Fabien	directeur de recherche	ECL/CNRS
	GOROKHOVSKI Mikhail	professeur	ECL
	HENRY Daniel	directeur de recherche	ECL/CNRS
	JEANDEL Denis	professeur	ECL
	JUVE Daniel	professeur	ECL
	LE RIBAULT Catherine	chargé de recherche	ECL/CNRS
	LEBOEUF Francis	professeur	ECL

	PERKINS Richard	professeur	ECL
	ROGER Michel	professeur	ECL
	SCOTT Julian	professeur	ECL
	SHAO Liang	directeur de recherche	ECL/CNRS
	SIMOENS Serge	chargé de recherche	ECL/CNRS
	TREBINJAC Isabelle	professeur	ECL
LTDS	BENAYOUN Stéphane	professeur	ECL
	COQUILLET Bernard	maître de conférence	ECL
	FOUVRY Siegfrid	chargé de recherche	ECL/CNRS
	GEORGES Jean-Marie	professeur émérite	ECL
	GUERRET Chrystelle	chargé de recherche	ECL/CNRS
	ICHCHOU Mohamed	professeur	ECL
	JEZEQUEL Louis	professeur	ECL
	JUVZ Denyse	ingénieur de recherche	ECL
	KAPSA Philippe	directeur de recherche	ECL/CNRS
	LE BOT Alain	directeur de recherche	ECL/CNRS
	LOUBET Jean-Luc	directeur de recherche	ECL/CNRS
	MARTIN Jean-Michel	professeur	ECL
	MATHIA Thomas	directeur de recherche	ECL/CNRS
	MAZUYER Denis	professeur	ECL
	PERRET-LIAUDET Joël	maître de conférence	ECL
	SALVIA Michelle	maître de conférence	ECL
	SINOU Jean-Jacques	professeur	ECL
	STREMSDOERFER Guy	professeur	ECL
	THOUVEREZ Fabrice	professeur	ECL
	TREHEUX Daniel	professeur	ECL
	VINCENS Eric	professeur	ECL

Acknowledgements

I would like to thank all the people who contributed to the work described in this thesis. Firstly and foremost, I thank my academic advisor, Prof. Eric VINCENS for accepting me into his research group. During three year, he contributed by giving me intellectual freedom in my work, supporting my attendance at some conferences, engaging me in new ideas, and demanding a high quality of scientific work in all my endeavors. Secondly, great thank to Dr. Jean-Patrick PLASSIARD who gives me opportunity to see directly the experiment tests of rammed earth wall. Truly, it is an honor for me to work with both of you. In addition, I would like to thank to my committee members; Prof. Domenico GALLIPOLI, Prof. Pierre-Yves HICHER, Prof. Paulo B. LOURENCO, and Dr. Noemie PRIME for their interest in my work.

My special thank is extended to my colleagues Juan Carlos, Kien, Duc, Feda, Nathanael, Evandro, Aurelie, Agathe, Ophelie, Francesco, Roman and other people at laboratory building G-8. They made the office a great work environment. Thank you to Florian CHAMPIRE and also Ranime EL NABOUCH for providing the experiment data which is required in the identification and also validation in my works. My gratitude also goes to french course classmates Kaijun, Milan, Alvaro, Pablo, Yuta, Ming. It's been a beautiful experience during french class. Then, I'd like to say thank you to my Indonesian friends here at Lyon who have made my life here very enjoyable. Big thanks to Satria Damarnegara for fruitful talking in the restaurant and coffee time. See you soon in Indonesia.

A big appreciation goes to Mr. Herry Vaza and Mr. Setyo Hardono for the support from the Institute of Road Engineering, Ministry of Public Works of Indonesia. Without their reccommendation, it would be difficult to reach this achievements.

Finally, I would like to acknowledge my beloved wife Nastiti Purwaningsih and also my child Raihan Adi Praditya for memorable times during live in Lyon. Their love, strength, impatients, and wisdom have inspired me to be the best I can be through many difficult times. To end, I owe my deepest gratitude to my parents also family in Indonesia; their love is the greatest power in the world and has driven me to succeed in every goal I have dreamed of.

Winarputro Adi RIYONO, October 2017

Abstract

Rammed earth is a vernacular building technique consisting in compacting successively layers of moist earth within formworks. This technique is present worldwide and in particular in the region Auvergne-Rhône-Alpes in France. As no regulation exists for rammed earth structures in France, the owners of such structures are helpless at the time when repairing damages appearing in any aging heritage structures. Moreover, this lack of regulation tends to slow down the development of such a constructive solution in new projects though this technique answers many of the issues raised by the sustainable development. The work presented herein is part of the national research project PRIMATERRE devoted to the study of construction building involving earth.

Herein, an elasto-plastic constitutive law is developed for modeling the behavior of rammed earth. It is based on a hierarchical approach of the modeling in relation to the information available to identify the set of model parameters and the refinement of phenomena to be modelled. This model was adapted from a pre-existing CJS model used in advanced foundation engineering for the modelling of granular soils. The necessary adaptation of some mechanisms of the model in the context of rammed earth material which holds the characteristics of a quasi-brittle material is highlighted.

Two levels for the model denoted CJS-RE which can be used in the context of monotonous loadings are presented herein. The first level is a simple elastic perfectly plastic model (CJS-RE1) and the second model is an elasto-plastic model with an isotropic hardening (CJS-RE2). Two mechanisms of plastic deformation are involved, one related to purely deviatoric phenomena and one related to tensile phenomena. The validation of the model was performed based on different sets of actual tests including diagonal compression tests and pushover tests on wallets. The simple elasto-plastic model CJS-RE1 was able to capture some basic features for these two tests and may be used for a first estimate of the system resistance. The more sophisticated model CJS-RE2 was found better to retrieve the non linear behavior of rammed earth over a larger range of deformations throughout both a diagonal compression test and a pushover test.

Finally, the modelling of interfaces between layers of earth seems oversized when the resistance of the system is investigated. However, since they may influence the simulated ductility of the system, they may be used to model the behavior of rammed earth system more precisely.

Keywords: constitutive model, elasto-plastic, interfaces

Resumé

Le pisé est une technique constructive vernaculaire consistant à compacter successivement des couches de terre humide entre des coffrages. Cette technique, présente dans le monde entier, l'est en particulier en France dans la région Auvergne-Rhône-Alpes. Comme il n'existe pas de réglementation attachée à cette technique constructive, il est très difficile pour des propriétaires de réparer leur bien. Le développement de cette tehnique pour de nouveaux projets souffre aussi de cette absence alors qu'elle répond à certains enjeux posés par le Développement Durable. Le travail présenté ici fait partie intégrante du projet national PRIMATERRE dédié à l'étude des constructions impliquant de la terre.

Une loi de comportement élasto-plastique est développée dans ce travail pour modéliser le comportement du pisé. Elle s'appuie sur une approche hiérarchisée de la modélisation en lien avec le nombre d'essais disponibles pour identifier les paramètres de modèle mais aussi en lien avec la complexité de phénomènes à prendre en compte. Ce modèle s'inspire d'un modèle pré-existant, CJS, développé en géotechnique pour modéliser le comportement mécanique des matériaux granulaires. Une adaptation s'est imposée pour prendre en compte les spécificités du comportement mécanique du pisé qui possède de nombreuses similitudes avec celui des matériaux quasi-fragiles.

Deux niveaux de modélisation pour le modèle de comportement appelé CJS-RE sont présentés, pouvant être utilisés dans un contexte de sollicitation monotone. Le premier niveau CJS-RE1 est un modèle élastique parfaitement plastique alors que le second niveau CJS-RE2 est un modèle élasto-plastique à écrouissage isotrope. Deux mécanismes de déformation plastique sont présents, l'un lié aux phénomènes purement déviatoires et l'autre aux phénomènes de traction. La validation du modèle a été entreprise sur la base de la simulation d'essais en laboratoire de compression diagonale et de chargement latéral (pushover) sur des murets, issus de la littérature. Le niveau CJS-RE1 a été capable de capturer les phénomènes essentiels issus de ces deux tests et peut être utilisé comme une première approches des problèmes. Le niveau CJS-RE2 a permis de retrouver plus précisément le comportement non linéaire du pisé sur une large gamme de déformations, que ce soit dans l'essai de compression diagonale ou dans le pushover.

Enfin, la prise en compte d'interfaces entre les couches dans la modélisation semble constituer une approche surdimensionnée lorsque seule la résistance d'un système constitué en pisé est recherchée. Cependant, parce qu'elles apportent une certaine ductilité au système dans la modélisation, elles peuvent être utilisée lorsque des résultats plus détaillés sont attendus.

Mots-clés: modèle constitutif, élasto-plastique, interfaces

Contents

Acknowledgements vii

Abstract ix

Resume xi

Contents xiii

List of Figures xvii

List of Tables xxiii

List of Symbols xxiv

General introduction xxvii

1 Rammed earth: state of the art 1

1.1 Introduction . . . 1
1.2 Method of construction . . . 4
1.2.1 Soil preparation . . . 4
1.2.2 Particle Size Distribution . . . 5
1.2.3 Formwork . . . 5
1.2.4 Compaction and density . . . 7
1.3 Behaviour of quasi-brittle materials . . . 8
1.3.1 Compression behaviour . . . 9
1.3.2 Tensile behaviour . . . 9
1.3.3 Confined compression behaviour . . . 12
1.4 Mechanical behaviour of rammed earth . . . 13
1.4.1 Compressive strength . . . 13
1.4.1.1 Unconfined compression test . . . 13
1.4.1.2 Confined compression test . . . 19
1.4.2 Tensile strength . . . 20
1.4.2.1 Unconfined tensile test . . . 20
1.4.2.2 Brazilian test . . . 21
1.4.2.3 Flexural tensile test . . . 23
1.4.3 Shear strength of rammed earth panels . . . 24

1.4.3.1 Diagonal compression test on wallets 24
1.4.4 Role of interfaces in rammed earth systems 27
1.4.5 Lateral resistance of wallets 29
1.4.5.1 Pushover test - monotonous 29
1.4.5.2 Pushover test - cyclic 32
1.5 Conclusion 34

2 Modelling system with quasi-brittle materials 35
2.1 Constitutive models 35
2.1.1 Damage model 36
2.1.1.1 Mazars model 38
2.1.1.2 Total strain rotating crack model 39
2.1.2 Elasto - plastic model 44
2.1.2.1 Mohr-Coulomb model 45
2.1.3 Elastic - plastic - damage model 47
2.1.3.1 Plasticity mechanism 49
2.1.3.2 Damage part 50
2.2 Regularization method 51
2.2.1 Partial regularization 52
2.2.2 Full regularization 53
2.3 Conclusion 53

3 New elasto-plastic model for rammed earth 55
3.1 Model CJS-RE 55
3.2 Elastic mechanism 56
3.3 Plastic mechanisms 57
3.3.1 Shear yield surface 57
3.3.1.1 Plastic criterion 57
3.3.1.2 Flow rule 59
3.3.1.3 Hardening 60
3.3.1.4 Shear softening 61
3.3.2 Tensile yield surface 62
3.3.2.1 Plastic criterion 62
3.3.2.2 Flow rule 63
3.3.2.3 Tensile softening 63
3.4 Different hierarchies for the constitutive model 64
3.4.1 CJS-RE1 64
3.4.2 CJS-RE2 67

4 Validation tests 71
4.1 Reference tests 71
4.1.1 MAT-1 71
4.1.2 MAT-2 74
4.2 Validation of CJS-RE1 model for MAT-1 76
4.2.1 Identification of model parameters 76

4.2.2 Validation: Diagonal compression test . . . 78
4.2.3 Validation: Pushover test . . . 82
4.3 Validation of CJS-RE2 model for MAT-1 . . . 85
4.3.1 Further identification of parameters . . . 85
4.3.2 Validation: Diagonal compression test . . . 86
4.3.3 Validation: Pushover test . . . 90
4.4 Simulations with interfaces for MAT-1 . . . 92
4.4.1 Identification of the interface parameters . . . 92
4.4.2 Diagonal compression test . . . 93
4.4.3 Pushover test . . . 96
4.5 Validation of CJS-RE1 for MAT-2 . . . 100
4.5.1 Identification of the model parameters . . . 100
4.5.2 Pushover test . . . 100
4.6 Validation of CJS-RE2 for MAT-2 . . . 102
4.6.1 Further identification of parameters . . . 102
4.6.2 Pushover test . . . 102
4.6.3 Pushover test with the modelling of interfaces . . . 105

5 Conclusion and perspectives 109

A Identification of CJS-RE parameters 111
A.1 Elastic parameters . . . 111
A.1.1 Young modulus E . . . 111
A.1.2 Poisson ratio ν . . . 112
A.2 Plastic parameters . . . 112
A.2.1 Maximum tensile strength T_{rmax} . . . 112
A.2.2 Dissymetry of the failure surface γ . . . 112
A.2.3 Failure radius R_{fail} . . . 113
A.2.4 Initial elastic radius R_{ini} . . . 114
A.2.5 Radius of the maximum volumetric contraction R_{mvc} . . . 114
A.2.6 Parameter of dilatancy β . . . 114
A.2.7 Isotropic hardening A . . . 116
A.2.8 Shear softening parameter α_s . . . 116
A.2.9 Tensile strength T_r . . . 117
A.2.10 Tensile softening parameter α_t . . . 117

B Relationship between CJS-RE and Mohr-Coulomb model 118
B.1 MAT-1 . . . 118
B.2 MAT-2 . . . 120

C A parametric study for compression-extension tests 122
C.1 CJS-RE1 . . . 123
C.2 CJS-RE2 . . . 125

D Mesh sensitivity **127**
D.1 Mesh sensitivity 127

E Computational procedure **129**
E.1 Calculation of the principal stresses 129
E.2 Calculation of hardening and softening modulus 131
E.2.1 Hardening modulus (H_{mod}) 131
E.2.2 Shear softening modulus (S_{mod}) 132
E.2.3 Tensile softening modulus (T_{mod}) 133
E.3 Determination of plastic multiplier 134
E.4 Plastic corrections in principal stress base 138

F A parametric study in the boundary value problem **139**
F.1 Diagonal compression test 139
F.2 Pushover test 144

Bibliography **148**

List of Figures

1.1 Rammed earth construction in the world; (a): The Nk'Mip Desert Cultural Centre in Canada [Tri10], (b): Herb Center in Switzerland [Ric14] . . . 2
1.2 Rammed earth distribution in the region of Auvergne-Rhône-Alpes [CRA17] . . . 2
1.3 Social housing in the district of l'Isle d'Abeau-Rhône in France [Aur14] 3
1.4 Soil profile with different layers [Dis16] . . . 4
1.5 Range of suitable gradings for unstabilised rammed earth proposed by several researchers [MW03] . . . 6
1.6 Formwork for rammed earth; (a): Traditional wooden formwork, (b): Steel formwork . . . 6
1.7 Compaction tools; (a): hand rammer, (b): pneumatic rammer . . . 7
1.8 Cracks process zone [Maz86] . . . 8
1.9 Typical compressive stress-strain curve for concrete [Che07] . . . 9
1.10 Cyclic compression test on concrete [KJ69] . . . 10
1.11 Tensile stress-strain of concrete, after [HC66] . . . 10
1.12 Stress-strain of concrete in cyclic tension, after [Ter80] . . . 11
1.13 Cracking during loading of traction from acoustic emission method, after [MS88] . . . 12
1.14 Triaxial data of concrete for low confinement pressures; (a): meridian plane ($\theta = 0°$) and (a): deviatoric section [WW74] . . . 12
1.15 Three scales for rammed earth studied by Bui [BMHM09] . . . 14
1.16 Elastic modulus of rammed earth at three different scales [BMHM09] 15
1.17 Comparison of elastic modulus between a loading perpendicular and parallel to the interfaces layer at a RVE scale [BM09] . . . 16
1.18 Influence of water content on the compressive strength [BMHW14] . 16
1.19 Influence of suction on the compressive strength [BMHW14] . . . 17
1.20 Compression behaviour of rammed earth within three different relative humidity for soil STR; (a): Stress-strain, (b): Volumetric deformation [CFM$^+$16] . . . 17
1.21 Compression behaviour of rammed earth for soil STR (RH=25%)[CFM$^+$16] 18
1.22 Young modulus as a function of the stress level for three different relative humidity and different soil sources; (a): STR, (b): CRA, (c): ALX [CFM$^+$16] . . . 19
1.23 Specimens after triaxial tests [CWHM12] . . . 19
1.24 Specimen and apparatus for unconfined tensile test [AKS16] . . . 20

1.25 Specimen and apparatus for brazilian test [AKS16] 21
1.26 Relationship between compressive and tensile strength in an earthen layer [BBLM14] 22
1.27 Tensile strength as a function of water content for unstabilised rammed earth [AKS16] 22
1.28 Three point bending test [CA13] 23
1.29 Flexural tensile strength of rammed earth interfaces from [CA13] . . 24
1.30 Diagonal compression test 24
1.31 Internal stresses in the diagonal compression test; (a): Stress components within distance x from center and (b): Horizontal force within distance x from center [MLGB13] 26
1.32 Mohr circle at the center of the wallet [MLGB13] 26
1.33 Shear stress vs shear distortion in a diagonal compression tests [SOM+13] 27
1.34 Horizontal load vs horizontal displacement of the loading platen; large shear box test [EN17] 28
1.35 Typical cracking patterns of wall in the pushover test [Haa09] . . . 29
1.36 Displacement field of the wall [EN17] 30
1.37 Pushover test results [EN17] 31
1.38 Crack pattern and load-displacement curve throughout a pushover test; wall-2 [NBP+16] 31
1.39 Load-displacement responses throughout a pushover test [AEY17] . 32
1.40 Crack pattern after pushover test for unstabilised rammed earth [AEY17] 33

2.1 Typical loading and unloading responses for three different constitutive models; (a) : elastic-damage model, (b): elastic-plastic model, and (c): elastic-plastic-damage model [JHPCG06]. 36
2.2 a) Damage variables D as a function of κ, b) Stress-strain response during uniaxial tension [PDBBG98] 37
2.3 Comparison between experiments and simulations of a compression test on a rammed earth wallet using Mazars model [BBLM14] . . . 40
2.4 Energy absorbed in the wallets during the damage process; comparison simulations using Mazars model and experiments [BBLM14] 40
2.5 Loading and unloading responses with TSRCM [BV10] 41
2.6 Total strain rotating crack model; (a): compression behaviour, (b): tensile behaviour [MOS+14] 43
2.7 Comparison between experiments and simulations (TSRCM model) of a diagonal compression test on rammed earth wallets [MOS+14] . 43
2.8 Stress states at failure from actual triaxial tests on a dense sand compared to Mohr Coulomb failure surface ([VDB84]) 45
2.9 Failure surface of Mohr-Coulomb model in the principal stress space [VDB84] 46
2.10 Mohr Coulomb failure criterion in the plane σ_1 and σ_3 with tension cut-off [Ita09] 47

2.11 Comparison between experiments and simulations; case of compression tests on wallets [BBLM16] . . . 47
2.12 Comparison between experiments and simulations; case of the diagonal compression tests on wallet [BBLM16] . . . 48
2.13 Failure surface for two different stress paths [JHPCG06] . . . 50
2.14 Simulation of the cyclic compression test by using plastic damage model [JHPCG06] . . . 51
2.15 Influence zone in the averaging process [Sar15] . . . 53

3.1 CJS-RE failure surface in the principal stress spaces . . . 56
3.2 Shear yield/failure surface in CJS-RE model; (a): in the meridian plane (θ_s =const) and (b): in the deviatoric plane (I_1 =const). In the case of CJS-RE1, the surface of the maximum volumetric contraction state coincides with the failure surface. . . . 58
3.3 Influence of γ on the shape of the shear yield/failure surface . . . 59
3.4 Evolution of the loading radius R in the CJS-RE model . . . 61
3.5 Shear softening function . . . 62
3.6 Tensile yield surface in CJS-RE model; (a): in the meridian plane and (b): in the deviatoric plane . . . 63
3.7 Failure surfaces of CJS-RE1; (a): in the meridian plane (θ_q =const) and (b): in the deviatoric plane (I_1 =const). I_1 is the first invariant of the stress tensor, s_{II} is the second invariant of the deviatoric stress tensor, s_1, s_2 and s_3 are the principal stresses of the deviatoric stress tensor. . . . 65
3.8 Simulation of a compression stress path with CJS-RE1 model; (a): stress-strain response and (b): volumetric deformation. . . . 66
3.9 Uniaxial tensile test responses with CJS-RE1 model . . . 66
3.10 Failure surfaces of CJS-RE2; (a): in the meridian plane (θ_q =const) and (b): in the deviatoric plane (I_1 =const). I_1 is the first invariant of the stress tensor, s_{II} is the second invariant of the deviatoric stress tensor, s_1, s_2 and s_3 are the principal stresses of the deviatoric stress tensor. . . . 67
3.11 Simulation of a compression stress path with CJS-RE2 model; (a): stress-strain response and b: volumetric deformation. . . . 68
3.12 Uniaxial tensile test responses with CJS-RE2 model . . . 68

4.1 PSD of soil before and after correction [SOS+14] . . . 72
4.2 Compression tests results [SOS+14] . . . 72
4.3 (a): Shear stress-shear strain curve of diagonal compression tests, (b): Crack pattern in the wall after the test [SOS+14] . . . 73
4.4 PSD of soil [EN17] . . . 74
4.5 Pushover test results and crack patterns in the wall-3 [EN17] . . . 75
4.6 Results of the identification of CJS-RE1 parameters; simulation of a compression test; experiments from [SOS+14] . . . 77
4.7 3D numerical model for the diagonal compression of a wallet . . . 78

4.8 Stress-train response from a simulated diagonal compression test using CJS-RE1; experiments from [SOS+14] . . . 79
4.9 Evolution of the plasticity states in a simulated diagonal compression tests using CJS-RE1 at different computation stages. . . . 79
4.10 Stress path of an element in a simulated diagonal compression test (CJS-RE1). . . . 81
4.11 3D-Model for the pushover test on a wallet . . . 82
4.12 Load-displacement response from a simulated pushover test on a wallet; MAT-1 . . . 83
4.13 Evolution of the plasticity states in a simulated pushover tests using CJS-RE1 at different computation stages . . . 84
4.14 Rotation of the wallet (state 1) . . . 84
4.15 Simulation of a compression test with CJS-RE2 (MAT-1); experiments from [SOS+14] . . . 86
4.16 Stress-train response from a simulated diagonal compression test using CJS-RE2; experiments from [SOS+14] . . . 87
4.17 Evolution of the plasticity states in a simulated diagonal compression tests using CJS-RE2 at different computation stages. . . . 87
4.18 Stress path of an element in a simulated diagonal compression test (CJS-RE2). . . . 88
4.19 Load-displacement response from a simulated pushover test on wallet; MAT-1 . . . 90
4.20 Evolution of the plasticity states in a simulated pushover tests using CJS-RE2 at different computation stages. . . . 91
4.21 Model of diagonal test with interfaces . . . 92
4.22 Diagonal compression test of CJS-RE2 model without and with interfaces results; experiments from [SOS+14] . . . 94
4.23 Stress state on the interfaces together with Mohr-Coulomb criterion for the interfaces in the diagonal compression test; a: interface group, b: reference states A and B, c: state A, d: state B. . . . 95
4.24 Model of pushover test on wallet with interfaces . . . 96
4.25 Simulation of a pushover test with CJS-RE1 and CJS-RE2 model with interfaces; set 2 . . . 97
4.26 Plastic points in the wallets at the peak response; (a): CJS-RE1 + int2 (b): CJS-RE2 + int2 . . . 97
4.27 Simulation of a pushover test with CJS-RE2 with and without the modelling of the interfaces . . . 98
4.28 Stress state of the interfaces compare with Mohr Coulomb criterion in the pushover test; a: interface group, b: reference state, c: interface stress state A, and d: interface stress state B. . . . 99
4.29 Result of the identification of CJS-RE1 parameters; simulation of a compression test; experiments from [EN17] . . . 101
4.30 3D-Model for the pushover test on a wallet with MAT-2 . . . 101
4.31 Load-displacement response from a simulated pushover test on a wallet vs experiments; MAT-2 . . . 102

4.32 Plasticity states in a simulated pushover tests using CJS-RE1 at different computation stages; MAT-2 . . . 103
4.33 Result of the identification of CJS-RE2 parameters for MAT-2; simulation of a compression test . . . 104
4.34 Load-displacement response from a simulated pushover test on wallet; MAT-2 . . . 104
4.35 Plasticity states in a simulated pushover tests using CJS-RE2 at different computation stages; MAT-2 . . . 105
4.36 Pushover test with CJS-RE2 model with interfaces for MAT-2 . . . 106
4.37 Plastic points in the wallettes at failure; (a) CJS-RE1 + int 2, (b) CJS-RE2 + int 2 . . . 107

A.1 Identification of $T_{\mathrm{r\,max}}$ by two compression triaxial tests . . . 113
A.2 Identification of γ by a triaxial compression and extension test or a same confining pressure . . . 113
A.3 Influence of the parameter of dilatancy β in the behaviour through the simulation of a compression test; (a): stress-strain, (b): volumetric deformation-strain . . . 115
A.4 Effect of the variation of isotropic hardening parameter A; (a): stress-strain, (b): volumetric deformation . . . 116
A.5 Influence of the shear softening parameter α_s on the stress strain curve of a compression test . . . 117

B.1 Shape of the Mohr Coulomb model ($\phi = 37°$) and CJS-RE model ($\gamma = 0.84$) in the deviatoric plane . . . 119

C.1 Model of the compression and extension tests . . . 122
C.2 Response along a compression stress path for CJS-RE1 model . . . 123
C.3 Triaxial stress path in the meridian $s_{II} - p$ plane for CJS-RE1 model 124
C.4 Responses in the extension stress path for CJS-RE1 model . . . 124
C.5 Response along a compression stress path for CJS-RE2 model . . . 125
C.6 Response along an extension stress path for CJS-RE2 model . . . 126
C.7 Triaxial stress path with CJS-RE2 model . . . 126

D.1 3D numerical model of a diagonal compression test with three different mesh sizes; a: 20x20x10, b: 30x30x15, c: 40x40x20 . . . 127
D.2 Stress-train response in a simulated diagonal compression test with different mesh sizes (CJS-RE1) . . . 128

E.1 Flowchart implementation of the constitutive model . . . 130

F.1 Effect of the isotropic hardening parameter A in the diagonal compression test . . . 140
F.2 Effect of the radius at failure R_{fail} in the diagonal compression test . 141
F.3 Effect of shear softening parameter α_s in the diagonal compression test . . . 141
F.4 Effect of tensile parameter T_{r} in the diagonal compression test . . . 142

F.5 Effect of tensile softening parameter α_t in the diagonal compression test . . . 142
F.6 Non-dimensional relationship between the maximum shear stress and the parameters assessed (x) for the homogeneous system in the diagonal compression test. . . . 143
F.7 Effect of the isotropic hardening parameter A in the pushover test . 145
F.8 Effect of the radius at failure R_{fail} in the pushover test . . . 145
F.9 Effect of shear softening parameter α_s in the pushover test . . . 146
F.10 Effect of tensile parameter T_{r} in the pushover test . . . 146
F.11 Effect of tensile softening parameter α_t in the pushover test . . . 147
F.12 Non-dimensional relationship between the maximum horizontal load and the parameters assessed (x) for the homogeneous system in the pushover test. . . . 147

List of Tables

1.1 Specimen details for compression test [MW03] . . . 14
1.2 Soil used in the study by ([BMHW14]) . . . 16
1.3 Soil used in the study (% by weight) [BBLM14] . . . 22
1.4 Direct shear test data [EN17] . . . 28
1.5 Young modulus of the wall based on image processing [EN17] . . . 30

3.1 Features in each level of the CJS-RE model . . . 64

4.1 Consistency limits and compaction properties of soils for rammed earth ([SOS+14]) . . . 72
4.2 Compression tests data [EN17] . . . 75
4.3 Properties of MAT-2 from direct shear test data [EN17] . . . 75
4.4 Identified CJS-RE1 model parameters for MAT-1; experiments from [SOS+14] . . . 77
4.5 Identified CJS-RE2 model parameters for MAT-1; experiments from [SOS+14] . . . 85
4.6 Parameters assumed for the Mohr-Coulomb type model for the interfaces . . . 93
4.7 Identified CJS-RE1 model parameters for MAT-2; experiments from [EN17] . . . 100
4.8 Identified CJS-RE2 model parameters for MAT-2; experiments from [EN17] . . . 103
4.9 Parameters assumed for the Mohr-Coulomb type model for the interfaces . . . 106

F.1 Parameters considered in the parametric study for diagonal compression test . . . 140
F.2 Parameters considered in the parametric study for pushover test . . . 144

List of Symbols

Latin:

A	Parameter of isotropic hardening	
C	Cohesion of material (MPa)	
C_i	Cohesion of interfaces (MPa)	
E	Young's modulus (MPa)	
f_c	Compression strength of material (MPa)	
f^{mvc}	Maximum volumetric contraction surface	
f^s	Shear yield/failure surface	
f^t	Tensile failure surface	
f_t	Tensile strength of material (MPa)	
f_t^i	Tensile strength of interfaces (MPa)	
$\boldsymbol{G}$	Derivation of plastic potential in shear mechanism	$\boldsymbol{G} = \frac{\partial g^s}{\partial \boldsymbol{\sigma}}$
g	Gauge length of the wallet in the diagonal compression test (mm)	
G^e	Shear modulus (MPa)	
g^s	Plastic potential in shear mechanism	
g^t	Plastic potential in tensile mechanism	
h	Height of the wallet (m)	
H_{mod}	Hardening modulus	
ΔH	Horizontal extension of the wallet in the diagonal compression test (mm)	
I_1	First invariant of stress tensor	$I_1 = tr(\boldsymbol{\sigma})$
$\boldsymbol{I}_d$	Identity tensor	
K^e	Bulk modulus (MPa)	
k_n	Interfaces normal stiffness (GPa)	
k_s	Interfaces shear stiffness (GPa)	
$\boldsymbol{n}$	Tangent vector of plastic potential surface	
p	Mean pressure (MPa)	$p = \frac{tr(\boldsymbol{\sigma})}{3}$
p	Variable of isotropic hardening (CJS-RE)	
PI	Plasticity Index	
$\boldsymbol{q}$	Local deviatoric stress tensor	
$\boldsymbol{q}_{II}$	Second invariant of local deviatoric stress tensor	

$\boldsymbol{Q}$	Tensor deviator	$\boldsymbol{Q} = \dfrac{\partial f^s}{\partial \boldsymbol{\sigma}}$
R	Radius of the loading surface	
R_c	Radius at failure in compression stress path	
R_{fail}	Radius at failure	
R_{ini}	Initial yield radius	
R_{mvc}	Radius in the maximum volumetric contraction state	
R_t	Radius at failure in extension stress path	
$\boldsymbol{s}_{II}$	Second invariant of global deviatoric stress tensor	$s_{II} = \sqrt{\boldsymbol{s}.\boldsymbol{s}}$
$\boldsymbol{s}_{II}^{mvc}$	Second invariant of global deviatoric stress tensor in the maximum volumetric contraction state	
S_{mod}	Shear softening modulus	
$\boldsymbol{s}$	Global deviatoric stress tensor	$\boldsymbol{s} = \boldsymbol{\sigma} - \dfrac{tr(\boldsymbol{\sigma})}{3}\boldsymbol{I}_d$
t	Thickness of the wallet (m)	
T_{mod}	Tensile softening modulus	
T_{r}	Parameter which characterizes tensile strength of the material (MPa)	
$T_{\text{r max}}$	Parameter which characterizes the maximum tensile strength of the material (MPa)	
$T_{\text{r max}}^{\text{ini}}$	Initial value of $T_{\text{r max}}$	
$T_{\text{r max}}^{\text{res}}$	Residual value of $T_{\text{r max}}$	
ΔV	Vertical shortening of the wallet in the diagonal compression test (mm)	
$\boldsymbol{X}$	Tensor which characterize the center of the loading surface	

Greek:

α_s	Shear softening parameter
α_t	Tensile softening parameter
β	Parameter of dilatancy
γ	Parameter of disymmetry
γ_d	Shear strain or shear distortion
δ	Lateral displacements in the pushover test (m)
ε_1	Axial deformation
$\boldsymbol{\varepsilon}^e$	Elastic deformations
$\boldsymbol{\varepsilon}^{sp}$	Plastic deformations generated from shear mechanism
ε_{diff}^{sp}	norms of the differences between current deviatoric plastic strain and deviatoric plastic strain at peak
$\boldsymbol{\varepsilon}^{\text{p fail}}$	deviatoric plastic strain at peak
$\boldsymbol{\varepsilon}^{tp}$	Plastic deformations generated from tensile mechanism
$\boldsymbol{\varepsilon}^{total}$	Total deformations
ε_v	Volumetric deformation
θ_q	Lode angle in the local axis (°)

θ_s	Lode angle in the global axis (°)
λ_s	Plastic multiplier in shear mechanism
λ_t	Plastic multiplier in tensile mechanism
ν	Poisson's ratio
σ_1	Major principal stress
σ_2	Intermediate principal stress
σ_3	Minor principal stress
τ	Shear stress (MPa)
ϕ	Friction angle (°)
ϕ_i	Friction angle of interfaces (°)
ψ	Dilatancy angle (°)
ψ_i	Dilatancy angle of interfaces (°)

General introduction

The constructions based on primal materials (earth, stone) are several millions in Europe. Most of them have to be renovated or repair either for maintenance or simply upgrading to modern standards. Moreover, the development of this type of construction is hindered by scientific lack of knowledge (multiphysics and water content dependent) and societal bottlenecks (non industrial heritage, unrecognized skills).

Currently, there is no recommendation to guide the implementation of the primal materials and in particular earthen materials in sustainable constructions. This lack leads typically to use a method and renovation that might be unsuitable and/or prefer other building materials which might be environmentally less efficient but benefiting from standardized testing procedure.

One of the earthen material is rammed earth. It is essentially a structure made from moist earth which is compacted layer by layer to form a wall. Understanding the behaviour of rammed earth is compulsory to reduce some scientific lacks previously mentioned. In the one hand, experimental tests are required to observe phenomena at stake in the material. On the other hand, modelling is necessary to optimise the design process. To achieve this goal, there is a need to define an appropriate constitutive model for the material. A too simple model cannot be sufficient to retrieve specific phenomena in the material (eg hardening, softening, dilatancy). But a sophisticated model with numerous model parameters may be oversized if experiment tests are limited for their identification.

The work presented herein is devoted to the design of a constitutive model which can be adapted according to the level of complexity and the availability of the experimental data for the identification of the model parameters.

This work is carried out within the framework of a national research of ANR project (PRIMATERRE), "Sustainable renovation and building: the challenge of local materials".

The content of this thesis is organized into four chapters:

Chapter 1 constitutes a state of the art of rammed earth as building materials. Some previous research findings on quasi brittle materials are highlighted. Some recent experimental results concerning the behaviour of rammed earth are also presented.

Chapter 2 contains some modelling aspects related to the quasi-brittle materials. It is presented some possible approaches that can be used for the modelling of quasi-brittle materials complete and in particular for rammed earth.

Chapter 3 details the new hierarchical constitutive model CJS-RE. The general equations of the model are presented together with the asociated features. Two levels of the model are designed which can be choosen according to the level of complexity of phenomena to be modelled and the availability of experimental data to identify the model parameters.

Chapter 4 presents some numerical tests which covers the identification of the model parameters and the validation procedure of CJS-RE. The identification of the model parameters is carried out using some experiments on two different materials from the literature. The validation is performed for two different boundary value problems for the two studied materials. In more detail, both a diagonal compression test and a pushover are simulated for the two investigated materials. Finally, the role of interfaces between layers on the global simulated behaviour of wallets is highlighted.

Chapter 1

Rammed earth: state of the art

1.1 Introduction

Rammed earth is a vernacular building technique consisting in compacting successively layers of moist earth within formworks. The target mechanical strength of these structures is reached after some weeks of drying when the capillary tensions within the pore networks provides a strong bonding effect between the different particles constituting the material. Sometimes, rammed earth is mixed with cementitious materials to obtain impermeable and more durable walls.

This construction method is currently becoming more popular because it meets the requirement of sustainable development such as a low embodied energy for the production and the processing of the materials which are locally extracted [WS13, TFL08]. In addition, recent studies tend to show that rammed earth walls may contribute to the inner comfort of the houses [MMOW01].

Among two recent emblematic uses of this technique, we can cite the Nk'Mip Desert Cultural Centre at the Osoyoos Indian Reserve in British Columbia, Canada (Figure 1.1a) designed by Hotson Bakker Boniface Haden Architects and the Herb Center for Ricola designed by Herzog & de Meuron in Laufen, Switzerland (Figure 1.1b). The former structure which was completed in 2006 was at that time the largest insulated rammed earth wall in the world with 80m long, 5.5m high and 0.60m thick. The second one (100m long, 11m high and 0.45m thick) was completed in 2014 and has the particularity to have been built using 670 rammed loam elements manufactured in a temporary nearby factory.

In France, rammed earth construction is essentially present in the region of Auvergne-Rhône-Alpes (Figure 1.2) and it was a citizen from the city of Lyon from the 18t̂h

(a) (b)

FIGURE 1.1: Rammed earth construction in the world; (a): The Nk'Mip Desert Cultural Centre in Canada [Tri10], (b): Herb Center in Switzerland [Ric14]

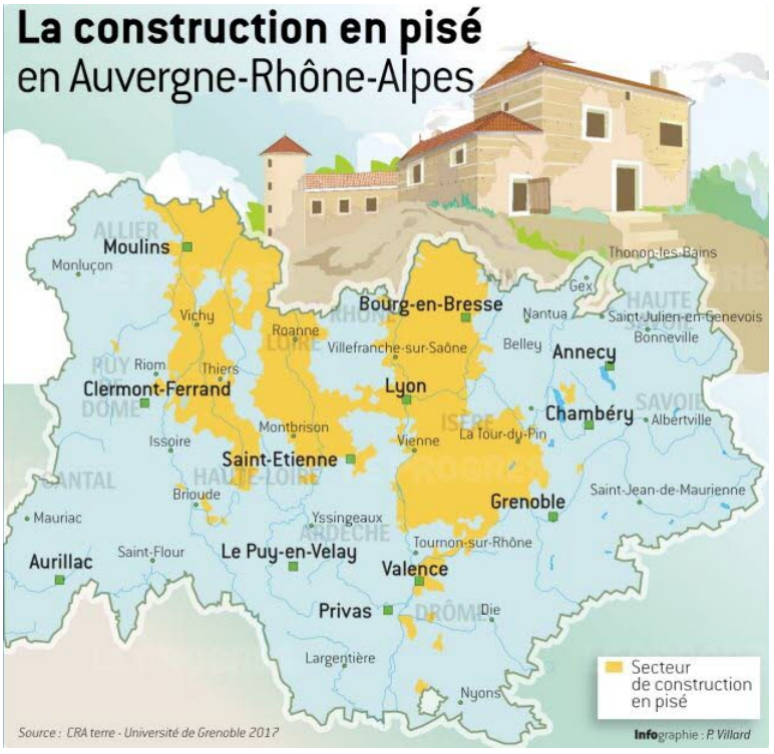

FIGURE 1.2: Rammed earth distribution in the region of Auvergne-Rhône-Alpes [CRA17]

century, Francois Cointereaux, that established the framework for such a building technique in a design book that is still a reference. After decades of abandon, the revival of this building technique in the region was motivated by the construction of a social housing located in the district of l'Isle d'Abeau, near Lyon (Figure 1.3). These buildings take part of the pilot experiments carried out in 1982 on earthen construction. The two earth buildings group are used for social housing units which have three floor levels. Most of the roof load is born by the rammed earth walls with a thickness of 0.5m including the six frontal columns.

FIGURE 1.3: Social housing in the district of l'Isle d'Abeau-Rhône in France [Aur14]

Rammed earth has a significant contribution for historic preservation because of two main reasons. First, it is an architectural style of structure which maintains the traditions and utilizes the human resources. Secondly, it is inherently environmentally suited since the material is based on local resources and can be used again after demolition. Moreover, rammed earth walls which hold a typical thickness of 0.5 to 0.6m have a phase shift temperature of twelve hours that tends to damp out the effect of variations of exterior temperature. They minimize the need for artificial air conditioning with its additional costs [Gra13].

Despite of rammed earth popularity recently, the development of rammed earth technology is confronted to several barriers. The lack of scientific knowledge related to a complex multiphysics material behaviour and also to the lack of reference documents for design, construction, and also maintenance purposes. This makes

the owners of such structures helpless at the time when they have to repair damages and insurances are reluctant to provide a ten-year guarantee. However, a given number of recent researches tends to bridge the gap between into both the mechanical and thermo-hygrometric behaviour of earthen structures.

1.2 Method of construction

This section provides some important requirements in order to build rammed earth structures. Generally, it involves the following steps:

- Choice of an adequate soil, with enough silt and clay to ensure the cohesion of rammed earth. Here the study of the particle size distribution is recommended but not mandatory;
- Screening of the soil to eliminate rock blocks and gravels;
- Preparation of the formwork;
- Wetting the soil at an ideal water content for compaction;
- Compaction of the soil in successive layers

1.2.1 Soil preparation

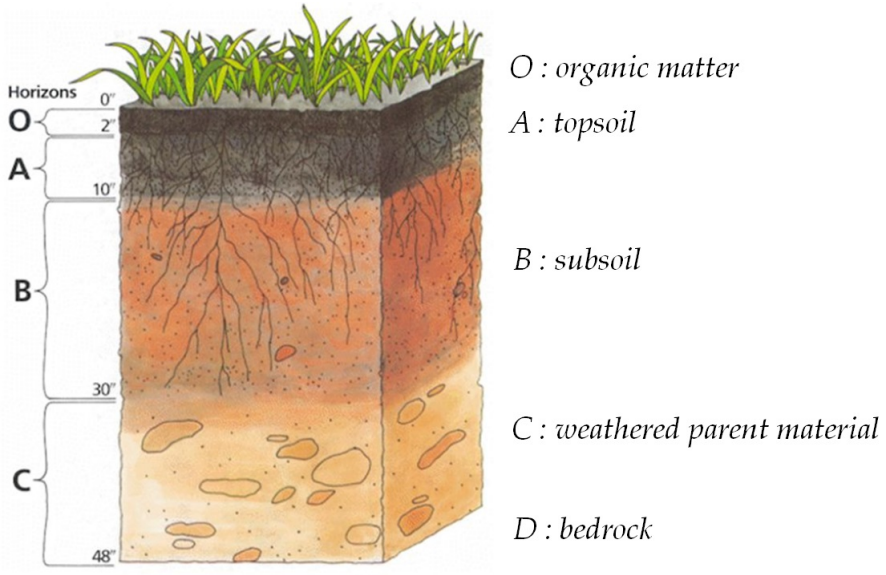

FIGURE 1.4: Soil profile with different layers [Dis16]

The suitable material for rammed earth construction is an inorganic subsoil found beneath the organic topsoil (Figure 1.4). The physical and chemical properties of subsoil are dependent on the original parent rock geology and subsequent weathering, including hydrological and hydro-geological processes, and other changes on exposure to the atmosphere. Thus, the properties of subsoil are defined by the region where the soil can be found.

1.2.2 Particle Size Distribution

Not all soil compositions are suitable for rammed earth construction and soil must be tested prior to a use to verify its suitability. Subsoil structure is made up of four main particle types. Classified according to size, they are gravel, sand, silt, and clay [Gra13, McH84]. Each particle type plays an important role in the structural integrity of rammed earth. Gravel is the skeleton that provides underlying structural stability. Together with the sand, it enhances weathering resistance of exposed surfaces and shrinkage resistance. The clay and silt are the binding agents that make possible the existence of strong capillary forces insuring the overall cohesion of the material.

For earth wall construction, the soil should contain all four elements. Ideally, the soil should have a high sand and gravel content with some silt and just enough clay to act as a binder and to assist soil compaction [Kea96]. Nevertheless, no soil is likely to be conformable with regards to all of the aspects considered [Sax95]. Then, some researchers proposed a grading range to help the artisan maker. Figure 1.5 shows the lower range and upper range for clay, silt, sand and gravel (particle size distribution by mass) for rammed earth construction as proposed by various researchers. Generally, the minimum clay content is of 5-10% and the maximum of 25-35%, then the minimum silt content is of 10-15% and the maximum of 30%. Finally, the minimum content of sand and gravel are respectively of 45-70% and of 70-80%.

1.2.3 Formwork

A formwork is used as a temporary support during soil compaction. The formwork requirements are sufficient strength, stiffness, and stability to resist to pressures during erection, placement of the soil, and demoulding. Unlike formwork for concrete, formwork for rammed earth can be removed almost immediately after compaction, enabling much faster reuse. There are several types of formwork and

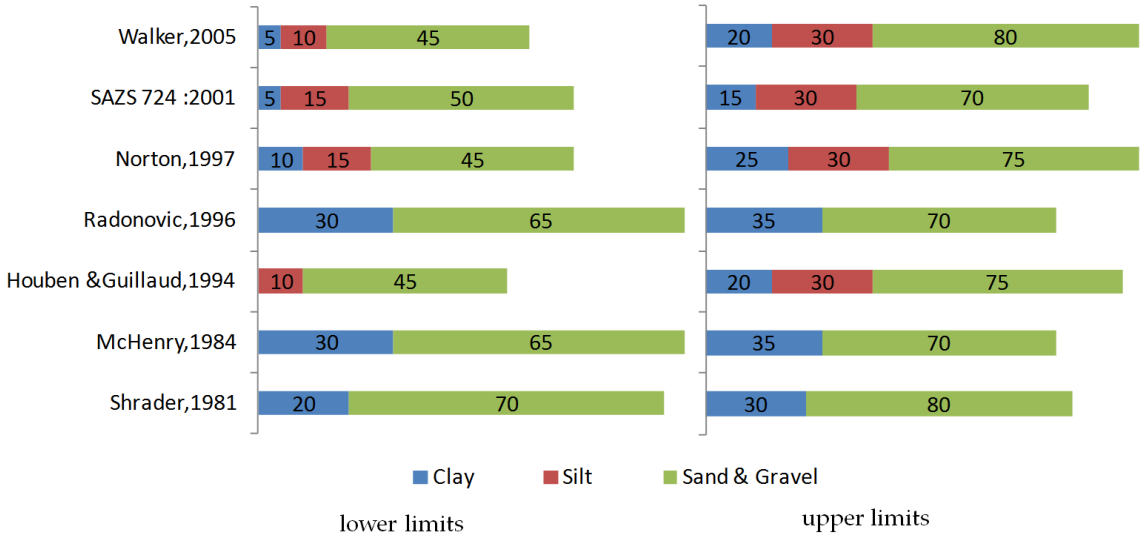

FIGURE 1.5: Range of suitable gradings for unstabilised rammed earth proposed by several researchers [MW03]

the selection of the appropriate type of moulding system for each application is important, since usually the time spent setting, aligning and stripping the forms is greater than the time spent for transporting and compacting the earth [Eas07].

(a) (b)

FIGURE 1.6: Formwork for rammed earth; (a): Traditional wooden formwork, (b): Steel formwork

Figure 1.6 depicts typical formworks used in the past or at present for rammed earth structures. Figure 1.6a is an example of wooden formwork which is the traditional one. It can be used to create rammed earth layers of height 0.4-0.5m high each step. At present, steel formworks are generally used. They prove to be stiffer and enable the creation of higher wall elements at one time (Figure 1.6b).

1.2.4 Compaction and density

Rammed earth should be compacted at or near to its optimum moisture content for the method of compaction to maximise its dry density and its final strength. The dry density depends on the soil type, the moisture content during compaction, and the compaction energy. A broad range of dry density values for rammed earth can be obtained from 1700 kg/m^3 to 2200 kg/m^3 [HGH94]. In order to achieve the maximum density, it is important to define the optimum moisture content related to the compaction energy used. Both the standard and modified Proctor tests are routinely used to determine the optimum moisture content and the maximum dry density of soils for rammed earth.

(a) (b)

FIGURE 1.7: Compaction tools; (a): hand rammer, (b): pneumatic rammer

In the field, compaction for earth construction can be processed manually or by using mechanical tools. A hand tamper composed of a heavy block of timber fitted onto a handle is generally used to achieve it (Figure 1.7a). The most important factors when considering using a manual rammer are the head material, the weight of the rammer, the shape of the head and the area of the head-face and finally the length of the handle [MW03]. This compaction method is less expensive but need an extra effort. The second method lies on the use of mechanical tools operated with compressed air to repeatedly lift and drop the striking head of the rammer (Figure 1.7b). The ideal impact rammer should have long-stroke distance, moderate speed and weight to make it safe, especially when working at the higher levels of the wall and slender tamper, to fit the corners of the forms [MW03].

1.3 Behaviour of quasi-brittle materials

Rammed earth holds all the characteristics of a quasi-brittle material like concrete. They are both composed of a granular skeleton composed of sand and gravels which are bent by smaller elements, obtained by the network of hydrates of cement in the case of concrete and obtained by the capillary forces existing in the network created by silt and clay. Quasi-brittle materials are characterized by the existence of a non linear behavior due to the creation of micro-fractures up to the maximum load followed by a post-peak softening. There is no yield plateau on the stress-strain curve [BXR91]. In the following, we will see that these characteristics will hold true for rammed earth and the general behavior of rammed earth can be understood thanks to the analysis of the behavior of concrete.

Concrete is composed of aggregates and mortar. The aggregates contributes mainly on concrete compressive strength while the binding agglomerates the aggregates. In concrete, some microcracks may develop during the loading process because of the difference in stiffness between aggregates and mortar. These differences can cause strain concentration along the interfaces between aggregates and mortar. Since the interfaces has a lower strength than the mortar, the cement matrix can be considered as the weakest link in the concrete.

Figure 1.8 shows the scheme of cracks process in the concrete [Maz86]. It can be seen that damage appears far ahead in the front of the macrocrack (zone 2). In addition, the part of the macrocrack which appears on the surface (zone 3) is not significant compared with the zone of complete separation (zone 4) inside the thickness of the material. A summary of some key facets of concrete behaviour is given in the following subsection.

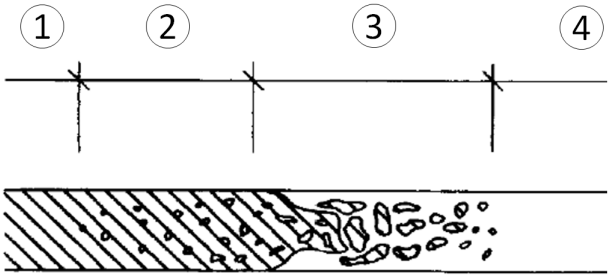

FIGURE 1.8: Cracks process zone [Maz86]

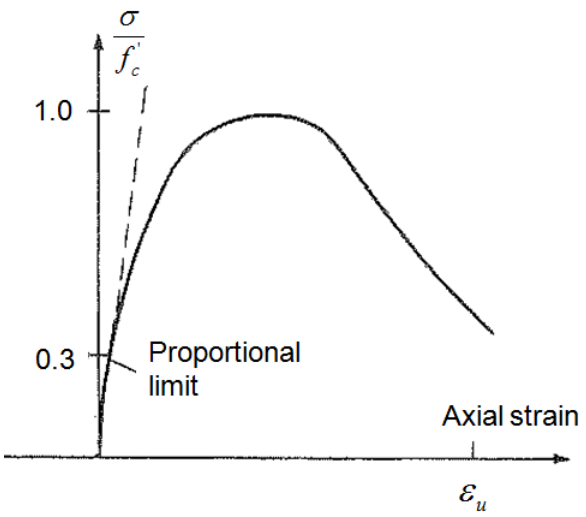

FIGURE 1.9: Typical compressive stress-strain curve for concrete [Che07]

1.3.1 Compression behaviour

A typical behaviour of concrete submitted to a monotonous compression loading is presented in Figure 1.9. The behaviour in the compression stress path shows nearly an elastic response up to about 30% of its maximum compressive strength. Beyond this point, the curves shows gradual increase in curvature up to about 80%, whereupon it bends more sharply and approaches the peak at f_c. Beyond this peak, the stress-strain curve has a descending part until crushing failure at ultimate strain ε_u [Che07].

Figure 1.10 depicts the result of a cyclic compression test on concrete where non-linear hardening and softening can be observed after it surpasses the elastic limit. It is also observed that the unloading response of concrete exhibits non linearities. At first, the loading and unloading part is similar with a similar initial stiffness, but with the increasing of the deformation, it exhibits a strong nonlinearity and a significant degradation of the stiffness can be observed. This degradation is supposed to be induced by the accumulation of micro-cracks at the origin of the internal damage of the material [Che07].

1.3.2 Tensile behaviour

The stress-strain response of concrete under a uniaxial tension can be seen in Figure 1.11 where the influence of the type of aggregates in the resulting tensile strength is reported. For example from curve 1 and 2 in Figure 1.11, the tensile

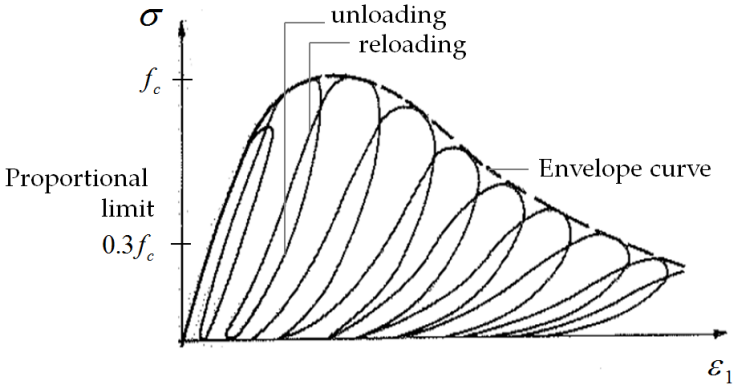

FIGURE 1.10: Cyclic compression test on concrete [KJ69]

strength of concrete with granite as aggregate gives a higher strength than concrete with gravel aggregate. It is also shown that the longer age gives a higher strength (curve 4 and 5 in the Figure 1.11). This inferred that concrete cementation (hardening process) is still active after 1 month of curing time.

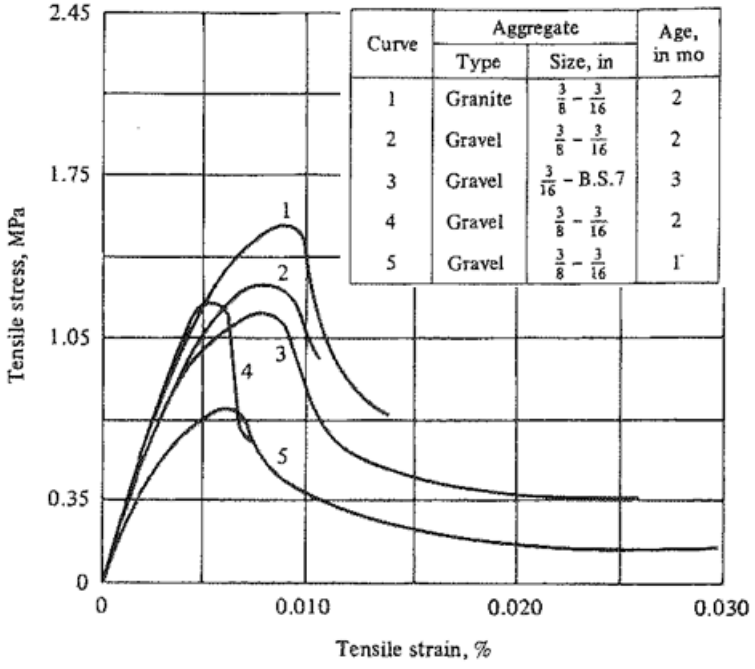

Curve	Aggregate		Age, in mo
	Type	Size, in	
1	Granite	$\frac{3}{8}-\frac{3}{16}$	2
2	Gravel	$\frac{3}{8}-\frac{3}{16}$	2
3	Gravel	$\frac{3}{16}$ - B.S.7	3
4	Gravel	$\frac{3}{8}-\frac{3}{16}$	2
5	Gravel	$\frac{3}{8}-\frac{3}{16}$	1

FIGURE 1.11: Tensile stress-strain of concrete, after [HC66]

The behaviour of the concrete in tension shows similarities with the envelope of the compression curves in Figure 1.10. For stress level less than 60% of the uniaxial tensile strength, the creation of microcracks is negligible. Thus, until this stress level the behaviour can be considered as elastic. Then, beyond 60% the unstable crack propagation starts to grow. The direction of crack propagation is perpendicular to the stress direction [Che07, NM07]. In uniaxial tension test, the crack propagation occurs rapidly and it is difficult to follow the descending part

(softening) of the stress-strain curve throughout the experiments. Nevertheless, according to [Che07], the tensile strength of concrete can be taken between 0.05 to 0.1 of the corresponding compressive strength for the material.

Similar finding also observed in the experiments by Terrien (1980) [Ter80] on the tensile behaviour of concrete as depicted in Figure 1.12. Before reaching the peak of resistance of the specimen, the cracking is diffuse. Micro-cracks appear in many parts of the test piece, mainly induced by a concentration of stresses in the vicinity of defects or pores. In this first stage, from a macroscopic point of view the material seems poorly affected by these microcracks. Hence, the uni-axial response of the material remains almost linear (Figure 1.12). After reaching the peak resistance of the specimen, the cracking is localized. The effect of the cracking are then more important and the stiffness of the uni-axial response greatly degrades. The loading-unloading responses in the descending part (dashed lines in the Figure 1.12) shows a decrease in the slope of the stress-strain response. Cracking develops in planes orthogonal to the direction of loading (Mode I). As a result, in each of these plans, the section capable of transmitting stress to ensure the cohesion of the material is reduced, which explains the loss of stiffness.

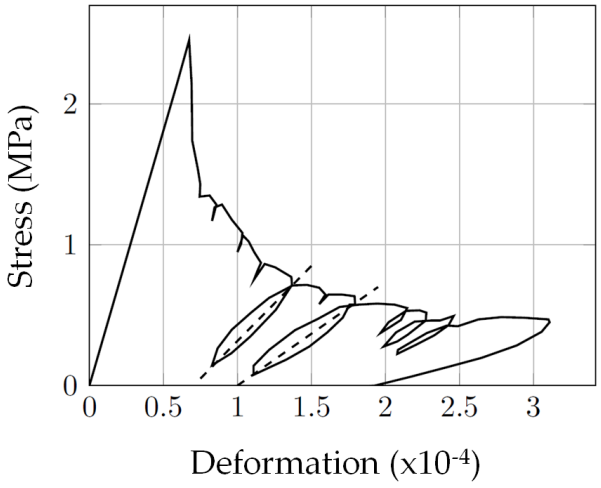

FIGURE 1.12: Stress-strain of concrete in cyclic tension, after [Ter80]

The two types of before mentioned cracking can be demonstrated by using an acoustic emission measurement technique by [MS88] as can be seen in Figure 1.13. Based on Figure 1.13, the appearance of voids (cracks) are represented by a cross on the different loading schemes. Micro-cracks first appear in a diffuse way before subsequently concentrating and forming a macro-crack.

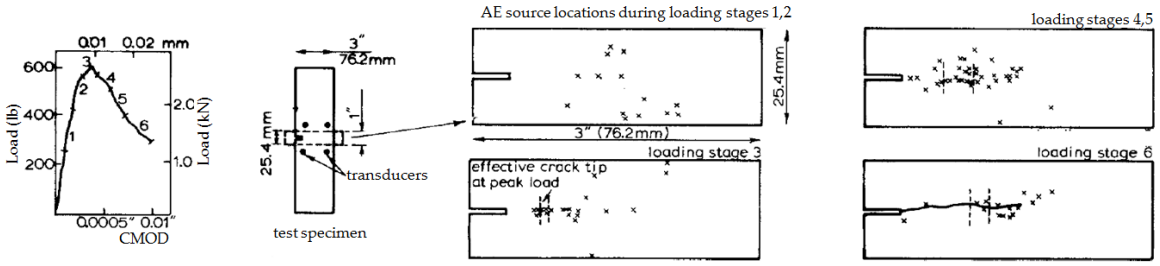

FIGURE 1.13: Cracking during loading of traction from acoustic emission method, after [MS88]

1.3.3 Confined compression behaviour

In a general triaxial stress path, concrete has a cone-shaped failure envelope with a curved meridian plane and a non circular section in the deviatoric plane. Figure 1.14 depicts the shape of the failure surface of concrete based on experiments at low compression regime (less than three times of the largest compressive stress) [LG72]. In the meridian plane (Figure 1.14a), concrete has a maximum resistance to compression which depends on the mean pressure. It is also can be observed that there is some dissymmetry in the compression and extension stress path. In the deviatoric plane (Figure 1.14b), the failure envelop holds a triangle-like shape. Figures 1.14a-b compare the results provided by the constitutive model from [WW74] with experiments where a good agreement is found at low confining pressure.

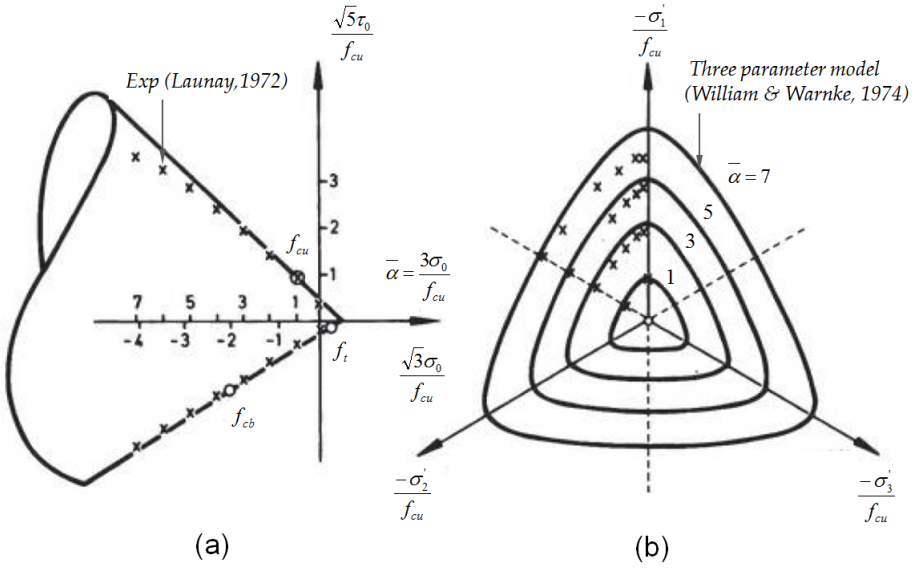

FIGURE 1.14: Triaxial data of concrete for low confinement pressures; (a): meridian plane ($\theta = 0°$) and (a): deviatoric section [WW74]

1.4 Mechanical behaviour of rammed earth

The mechanical behaviour of rammed earth can be related to the density of the soil after ramming, cohesive strength of fines content, aggregate strength, moisture condition during testing. Their influence on the mechanical strength of rammed earth can be evaluated from several tests in laboratory. This section investigates three important mechanical characteristics for the material which are the compression strength, the tensile strength, and the shear strength.

1.4.1 Compressive strength

1.4.1.1 Unconfined compression test

The laboratory tests used to determine the compressive strength (shear strength) of rammed earth are similar to those used for concrete, bricks and blocks [Uni58]. A summary of the required specimen details for compression strength testing according to various standards around the world is presented in Table 1.1. The specimens can be either cylinders or prisms (including cubes) prepared with a specified compaction effort. Specimens are capped using hardboard, plaster or similar material. This additional interfaces becomes negligible when the samples have a slenderness ratio equal to or higher than two [CG12]. A uniform load is then applied continuously until failure occurs and the maximum load is recorded. During testing, measurements of axial strain in the middle part of the sample allow the modulus of elasticity and the stress-strain relationship to be determined.

Bui et al. [BMHM09] performed an experimental study of the compressive strength at three scales including:

- Scale 1 : Full scale
- Scale 2 : Representative Volume Elements (RVE), and
- Scale 3 : Compressed Earth Block (CEB)

First, scale 1 corresponds to an on site wall (Figure 1.15a). Secondly, the RVE scale is the smallest size of volume that where stabilized properties for a heterogenous material can be found (Figure 1.15b). For the RVE scale, the sample dimensions were close to those of the in situ walls. Thirdly, the CEB scale was carried out by extracting a part of the layer in the RVE scale (Figure 1.15c). The idea was to develop a simple test method in laboratory able to allow the elastic parameters of rammed earth to be identified. For scale 1, the estimation of the elastic modulus

TABLE 1.1: Specimen details for compression test [MW03]

Specimen details	Bulletin 5; Earth wall construction, CSIRO	Australian standards (2002)	New Mexico Adobe & Rammed Earth Building Code (Tibbets,2001)	NZS
Cylinder				
- Diameter (mm)	150	150	N/A	N/A
- Height (mm)	110	300	N/A	N/A
Prism				
- Length (mm)	150	N/A	102	N/S
- Height (mm)	150	N/A	102	N/S
- Width (mm)	1.3 x height	N/A	102	2 x height
Number of specimen (min)	5	1 sample for every 25-100 m^2	N/S	5

Note: N/A = Not Available, N/S = Not Specified

was carried out by correlating of the natural frequencies measured from vibration test to the natural frequencies obtained through modelling. For the two other scales, the determination of the elastic modulus was carried out by using static schemes through compression tests in the laboratory.

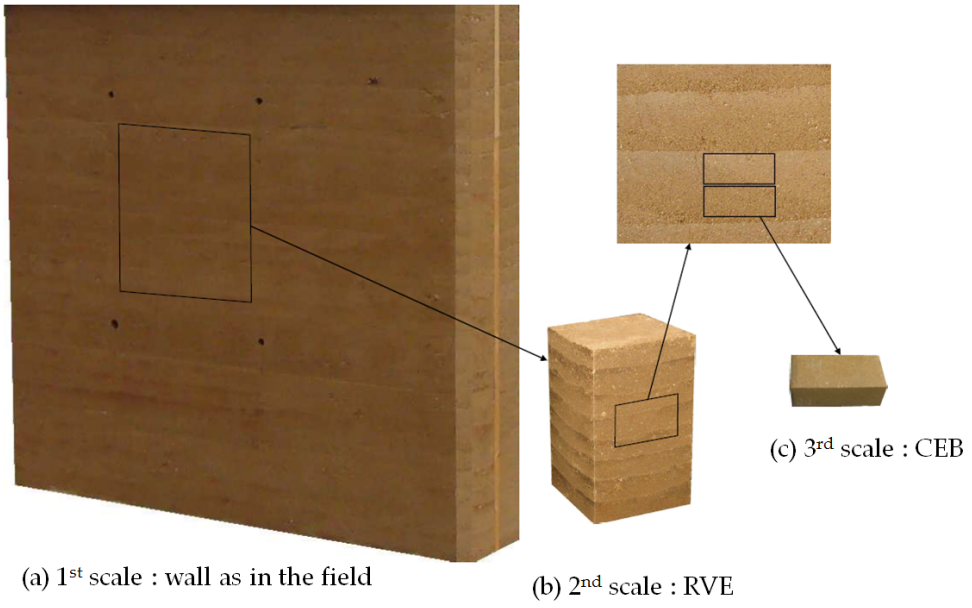

FIGURE 1.15: Three scales for rammed earth studied by Bui [BMHM09]

The summary of the results obtained with the three different approaches is presented in Figure 1.16. It can be seen that at first, when the preload is low (less than 0.2 MPa) the elastic modulus obtained from CEB samples gives a higher result than RVE samples. Nevertheless, on the average, the result from the CEB

is close to that obtained at the RVE scale. The in-situ dynamic measurements (full scale) give a higher result than with the two other approaches. This might be related to the assumption of the homogeneous model in the modelling which gives a higher natural frequency [BMHM09].

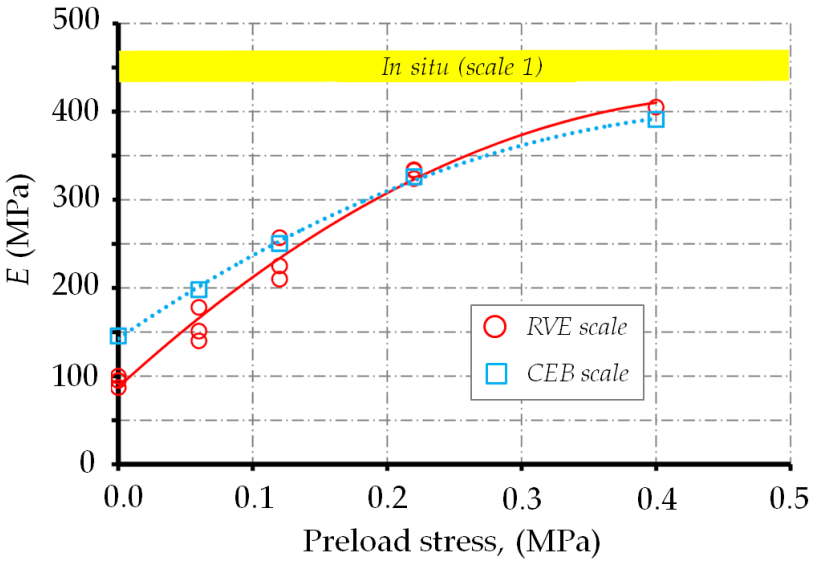

FIGURE 1.16: Elastic modulus of rammed earth at three different scales [BMHM09]

By using compression test at the RVE scale, Bui [BM09] also studied the potential anisotropic behaviour of earth material involved by the interfaces between each layers of the rammed earth. Thus, they performed a compression test on rammed earth with two different loading orientations with respect to the interfaces: perpendicular and parallel to the interfaces. The elastic modulus is found to be similar in both cases (Figure 1.17). Therefore, the elastic behavior of rammed earth can be considered as isotropic [BMHM09].

Another study by Bui et al. [BMHW14] was conducted on the effect of the current moisture content on the compressive strength of rammed earth. The moisture content at compression test varies from the wet state directly after manufacturing (11-13%) to dry state in atmospheric conditions (1-2%). Five types of soils including stabilized soil were tested. The composition of each type of soil is presented in Table 1.2. The test results are depicted in Figure 1.18. The increase of moisture content reduces the compressive strength systematically which was expected since capillary forces (suction) are only very active when the water content is very low (Figure 1.19). These findings strengthened the results from Jaquin et al. [JAGT09] in which they only performed tests on one type of soil.

Champire et al. 2016 [CFM+16] presented an experimental study focusing on the influence of relative humidity on the compressive strength of rammed earth. Three different specimen sources (STR, CRA and ALX) were used. They all come from

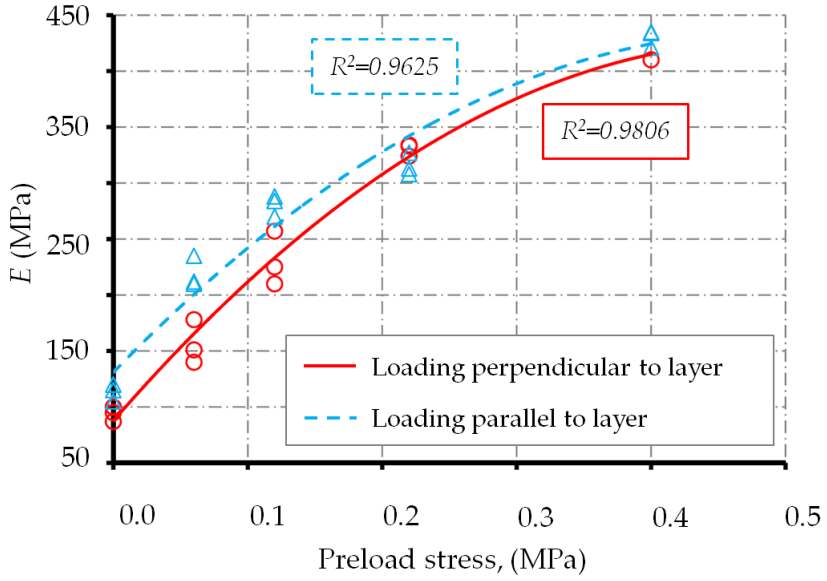

FIGURE 1.17: Comparison of elastic modulus between a loading perpendicular and parallel to the interfaces layer at a RVE scale [BM09]

TABLE 1.2: Soil used in the study by ([BMHW14])

Soil	Clay(%)	Silt(%)	Sand(%)	Gravel(%)
A	5	30	49	16
B	4	35	59	2
C	9	38	50	3
D	10	30	12	48
E	10	22	43	25

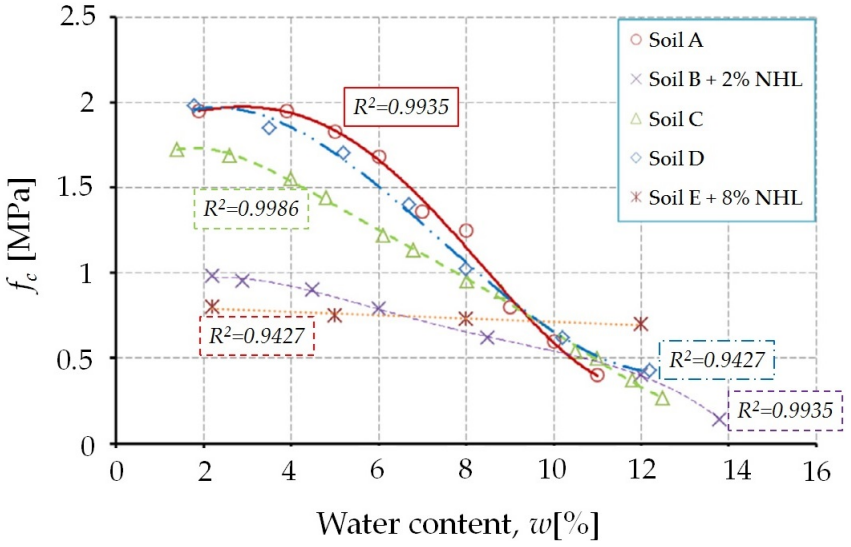

FIGURE 1.18: Influence of water content on the compressive strength [BMHW14]

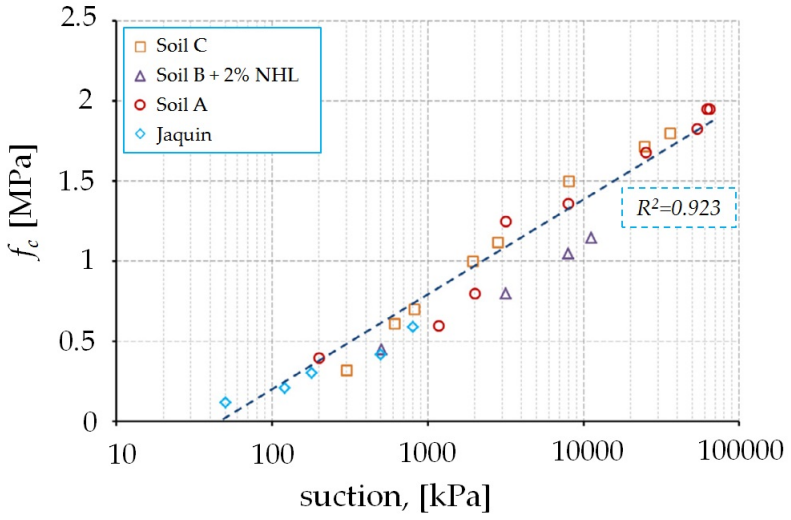

FIGURE 1.19: Influence of suction on the compressive strength [BMHW14]

existing old rammed earth constructions (dating before the 20^{th} century) located in the Auvergne-Rhône-Alpes region in the South-East of France. Unconfined compression test on cylinder samples were performed. The axial deformation field was measured with a Digital Image Correlation (DIC) process. This approach was also validated using non contact sensors in the axial and also radial direction.

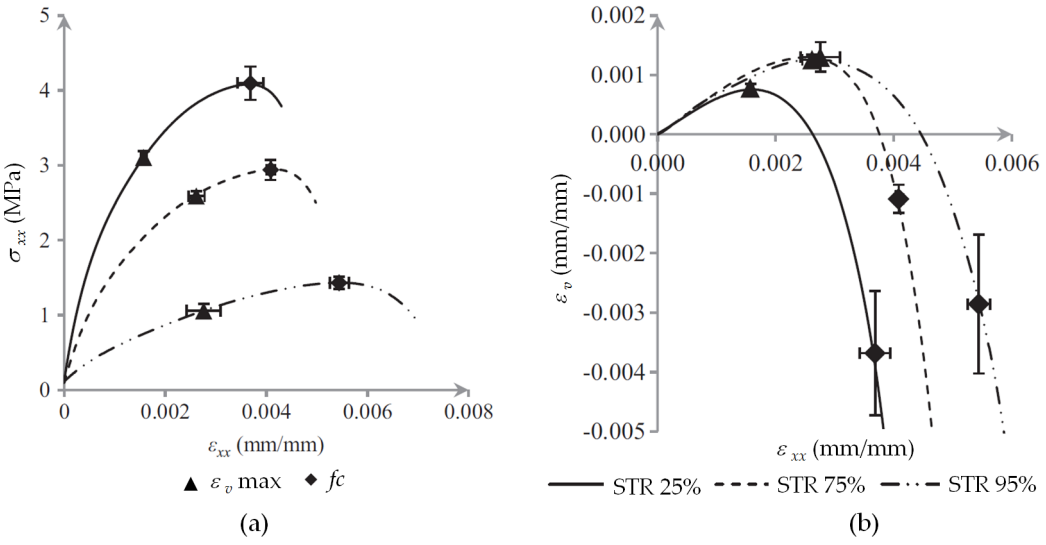

FIGURE 1.20: Compression behaviour of rammed earth within three different relative humidity for soil STR; (a): Stress-strain, (b): Volumetric deformation [CFM+16]

Figure 1.20 presents results of monotonous compression tests on homogeneous samples for three different relative humidities (25%, 75% , and 95%) for the soil STR. Figure 1.20a presents the stress-strain response and Figure 1.20b shows the volumetric deformation response. Figure 1.20a shows that the stress-strain relation is non-linear and strongly dependent on the relative humidity. From Figure 1.20a

it can also be observed that generally rammed earth has an elastic region 20 - 30% of the compressive strength. Beyond the elastic region, it continues to undergoes inelastic deformation before failure takes place. If we compare the stress-strain of rammed earth with 25% relative humidity (Figure 1.20a) and the envelope of concrete in Figure 1.10, then we can observed a similar patterns between them.

Figure 1.20b shows that for low axial strains, contractancy can be observed while at larger axial deformations, the volumetric strain reaches its peak value and decreases afterwards. Thus, the behavior becomes dilative due to decohesion of grains and the generation of numerous micro-cracks across the sample. When the axial stress is equal to f_c, the sample has a volume higher than its initial volume (ε_v negative). It is also observed that sharp dilatancy can be observed and mainly related to a structural increase of volume due to the opening of cracks.

Under some stress reversal, rammed earth shows some permanent deformation which is also observed in concrete. For example, Figure 1.21 depicts test results of a compression test on STR (RH=25%) with an unload and reload process which points out plastic phenomena. In addition, the Young modulus has slightly degraded. This reduction of elasticity is also observed for other soil types as shown in Figure 1.22 where the rate of elastic degradation is important for STR soil, but not significant for CRA and ALX. This different level of damage is influenced by the nature of the earth source. Figure 1.22 also indicates that for the same soil type, the level of damage is influenced by the relative humidity.

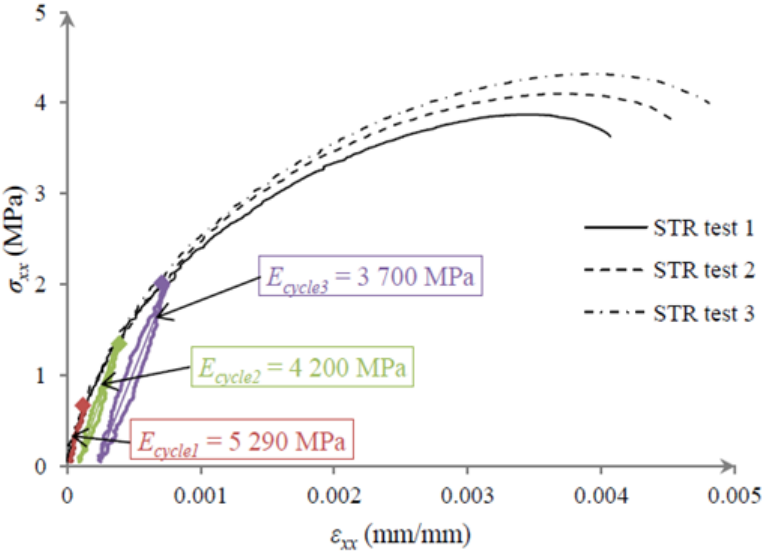

FIGURE 1.21: Compression behaviour of rammed earth for soil STR (RH=25%)[CFM+16]

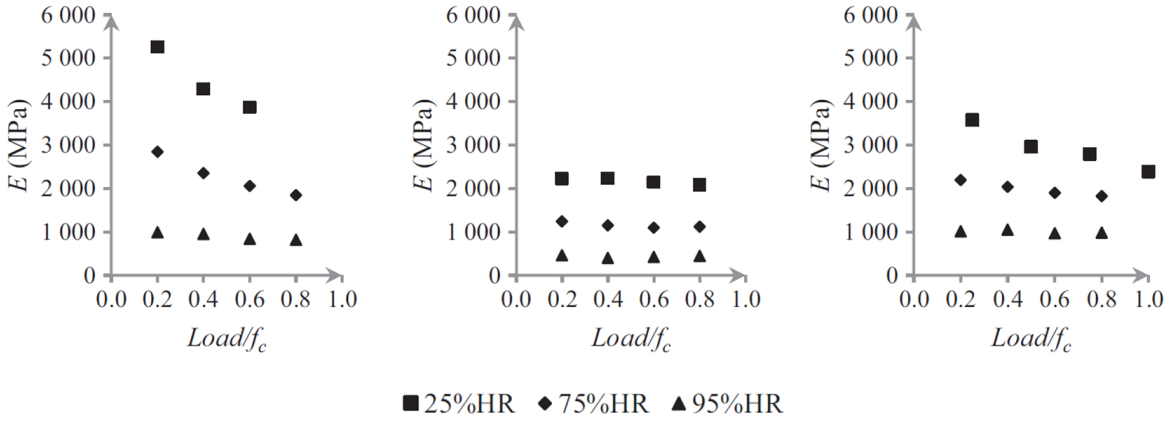

FIGURE 1.22: Young modulus as a function of the stress level for three different relative humidity and different soil sources; (a): STR, (b): CRA, (c): ALX [CFM+16]

.

1.4.1.2 Confined compression test

FIGURE 1.23: Specimens after triaxial tests [CWHM12]

Confined triaxial test can be used to estimate the shear strength of rammed earth and the influence of the mean pressure on it. Cheah et al. [CWHM12] used a triaxial test to obtained the shear strength of unstabilised rammed earth and a stabilised rammed earth material reinforced with sisal and flax fibres. It is found that the friction angle of unstabilised rammed earth is equal 45° and cohesion of 724kPa. Whereas, the friction angle measured for the stabilised rammed earth test specimens ranged between 47° and 56° with ranges of cohesion between 554kPa and 758kPa. It can be inferred that the addition of sisal and flax fibres might can increase the friction angle. But, on the other hand, it tends to reduces the cohesion of rammed earth. Figure 1.23 shows the specimen condition after the tests where failure along a diagonal shear plane can be observed.

1.4.2 Tensile strength

Like in the case of soil, generally the tensile strength of rammed earth is neglected due to its low value. But in the case of extreme loading conditions such as earthquakes, neglecting this tensile strength could be disadvantageous for the design purpose. As for many granular materials, an experimental tensile strength is difficult to process (unconfined tensile test). It can be estimated indirectly through a Brazilian test or a flexural tensile test.

1.4.2.1 Unconfined tensile test

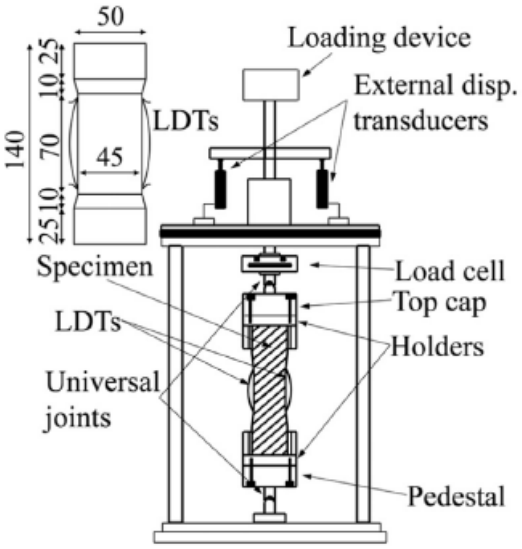

FIGURE 1.24: Specimen and apparatus for unconfined tensile test [AKS16]

In this test, the specimen is directly tensioned until it reaches failure. One difficulty performing this test is to avoid failure in the fixed portions in which tensile stresses might concentrated. [AKS16] used a cylinder specimen and trimmed it at the middle height as counter measure. It is also used an epoxy resin in the interfaces between the specimen and the loading platen to ensure strong bonding between the sample and the loading platen. Figure 1.24 depict specimen and apparatus for the unconfined tensile test. The axial displacement was measured by a pair of external displacement transducers set at an opposed position around the loading shaft, as schematically in Figure 1.24 and a pair of LDTs (Local Deformation Transducers) attached directly on the side of the specimens at middle height with a reduced diameter. A tensile load was applied to the specimen at an axial strain rate of 0.005%/min, so that the peak tensile strength was measured accurately [KTN+08].

Figure 1.27 gives the relationship between tensile strength of rammed earth as a function of water content ([AKS16]). Araki et al. [AKS16] found a tensile strength of rammed earth in the range of 7.5% until 12.5% of the compressive strength (Figure 1.27). In Figure 1.27, one can note that the tensile strength is influenced by the water content which was expected.

1.4.2.2 Brazilian test

In the Brazilian test (or splitting test), a cylinder specimen is loaded uniformly in compression along the length. This condition creates tensile forces perpendicular to the loading direction and one can evaluate the tensile strength indirectly. Due to scale effects, the tensile strength is supposed to be slightly overestimated by the brazilian test. In fact, in this latter test, the failure surface is imposed while in a uniaxial tensile test, the main crack will initiate around a local heterogeneity (defects) within the composite material.

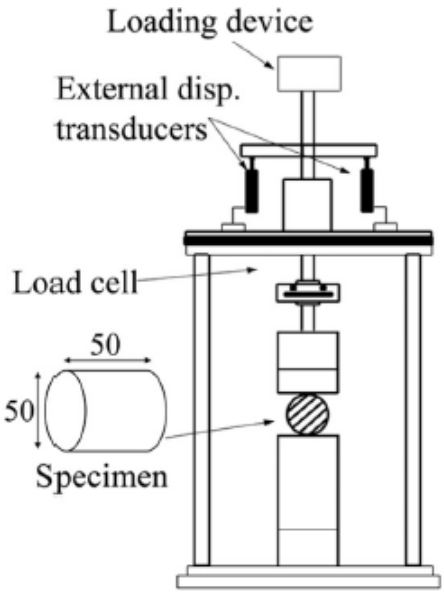

FIGURE 1.25: Specimen and apparatus for brazilian test [AKS16]

Bui et al. [BBLM14] performed brazilian tests on three different soils as mentioned in Table 1.3. According to the study, the tensile strength of rammed earth (including stabilised rammed earth) is roughly equal to 11% of the corresponding compression strength (Figure 1.26). as previously mentioned, Araki et al. [AKS16] found a tensile strength of rammed earth in the range of 7.5% until 12.5% of the compressive strength (Figure 1.27)

TABLE 1.3: Soil used in the study (% by weight) [BBLM14]

Soil	Clay(%)	Silt(%)	Sand(%)	Gravel(%)
A	10	25	18	47
B	5	30	49	16
C	8	34	8	50

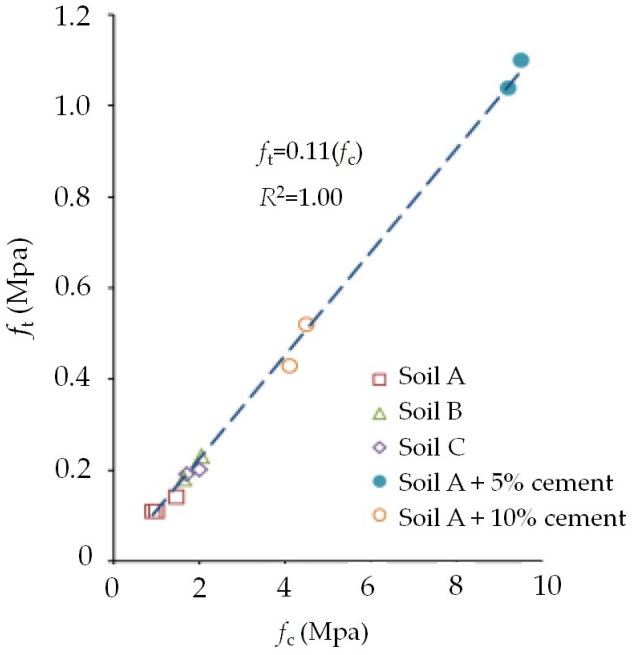

FIGURE 1.26: Relationship between compressive and tensile strength in an earthen layer [BBLM14]

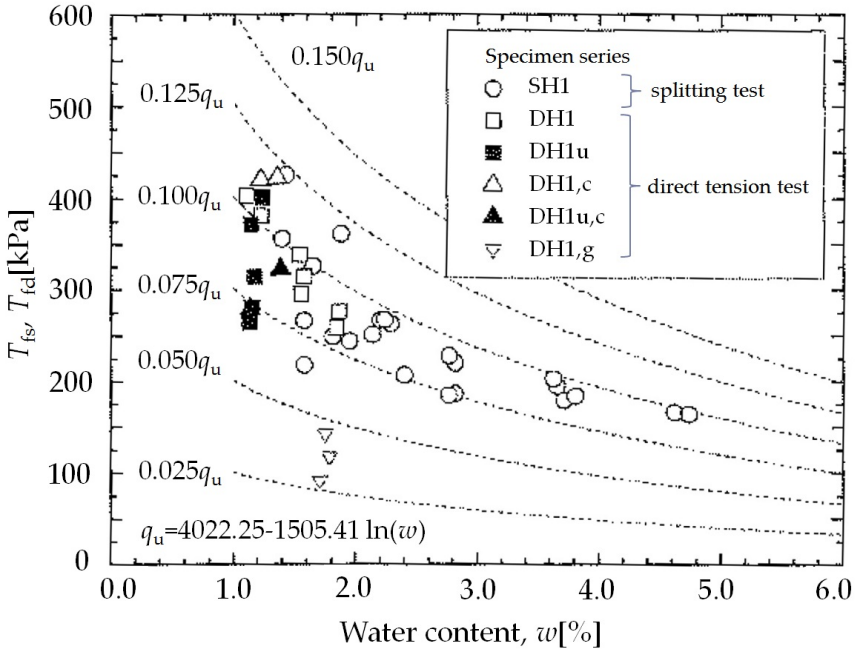

FIGURE 1.27: Tensile strength as a function of water content for unstabilised rammed earth [AKS16]

1.4.2.3 Flexural tensile test

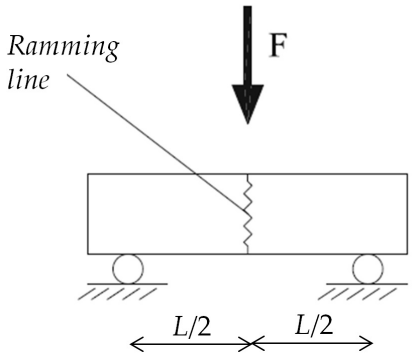

FIGURE 1.28: Three point bending test [CA13]

The tensile strength of rammed earth can be obtained by means of a flexural tensile test. It can be undertaken by three or four points bending test. In this test, a beam specimen of earth is subjected with line load in the out of plane direction on the upper center. Under this type of boundary condition, the top layer of the beam will experiences a compression stress whereas the lower layer undergoes a tensile stress leading to failure.

Ciancio et al.[CA13] used this test to obtain the tensile strength of an interface in rammed earth as depicted in Figure 1.28 where point load acting on the interface (ramming line). It is found that tensile strength at the interfaces is smaller than the indirect tensile strength. Figure 1.29 depicts the flexural tensile strength (FTS) of samples for three batches. It is shown that there are some variation of results between the 3 batches and within the samples from batch 2. This supposed to be arise from the specimens sampling for this test that were cored from the walls. The coring process might have damaged the structure of the samples [CA13].

In conclusion, it is recommended to use the Brazillian test to identify the tensile strength of an earth layer because the tensile stress is mobilized inside the compacted layers [AKS16]. In order to estimate the tensile strength of the interfaces between layers, the uniaxial tensile test or the flexural tensile test may be more appropriate.

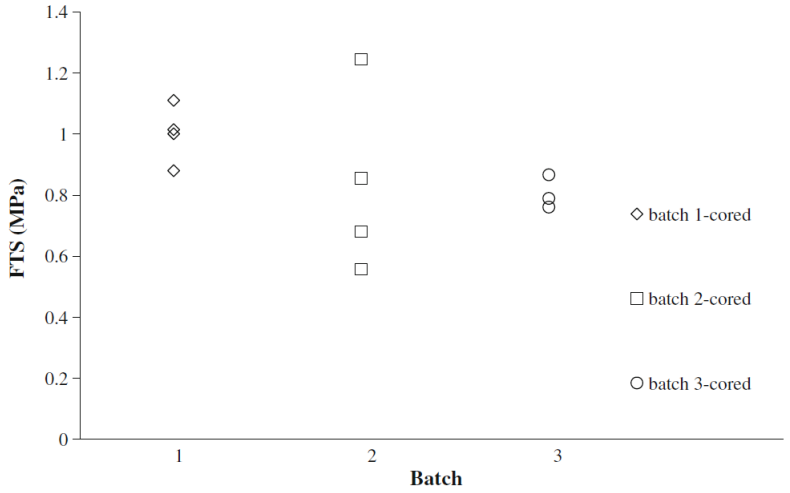

FIGURE 1.29: Flexural tensile strength of rammed earth interfaces from [CA13]

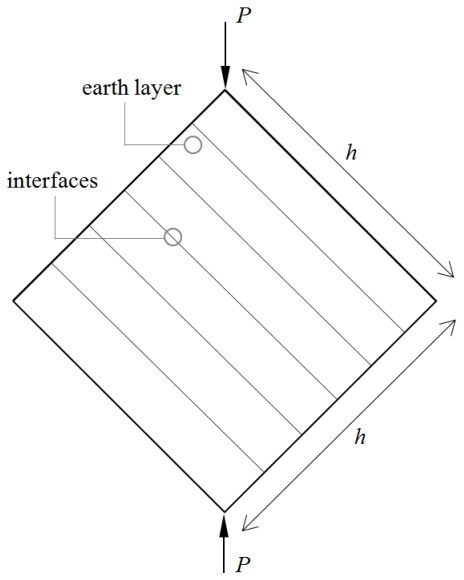

FIGURE 1.30: Diagonal compression test

1.4.3 Shear strength of rammed earth panels

1.4.3.1 Diagonal compression test on wallets

The shear strength can also be measured at a scale larger than the Representative Volumetric Element by means of a diagonal compression test which involves more clearly the possible influence of the interfaces between compacted layers. In this test, a wallet is inclined to 45° and loaded vertically using a loading shoe along the diagonal of the wallet (Figure 1.30). This test corresponds to the one defined in the standard of ASTM E-519. The diagonal compression test is used to determine the diagonal tensile or shear strength of 1200 x 1200mm^2 masonry assemblages. The deformations can be measured by using compressometers and extensometers

or by using strain gauges mounted along the two diagonals as close to their intersection as possible [AE02].

In this test, the diagonal loading induces a diagonal tension failure with the specimen splitting apart along the loading direction [AE02]. This splitting starts at the center where tensile stress is higher and then propagates to the upper and lower part of the wall. This failure mode is analytically established in the works of [MLGB13] as shown in Figure 1.31.

It is assumed that for square specimens, the vertical component of the stresses σ_v in the horizontal diagonal (perpendicular to loading) is equal to the applied load divided by the area. In addition, the stress vector along horizontal diagonal is supposed to be proportional to the ratio between the distance from the center of the panel to the point along diagonal horizontal considered (x) with the distance from center to the top corner where the load is applied (Figure 1.31a). This leading to the relation of the horizontal $\sigma_h(x)$ and vertical σ_v components of the stress as:

$$\frac{\sigma_h(x)}{\sigma_v} = \frac{x}{h\sqrt{2}/2}$$

Figure 1.31b shows that the horizontal force (N_x) assume to spreads at 45° on the vertical diagonal along a length of $2x$. Thus the horizontal stresses $\sigma_H(x)$ on the vertical axis along $2x$ can be written as:

$$\sigma_H(x) = \frac{N_x}{2xt} \tag{1.2}$$

At the intersection of the diagonal where the tensile stress is higher, the total tensile stress σ_t can be obtained by the summation of the contributions on each part of the horizontal diagonal as follows:

$$\sigma_t = \int_0^{h\sqrt{2}/2} \sigma_H(x)dx = \int_0^{h\sqrt{2}/2} \frac{P}{h^2 t}dx = \frac{P}{h\sqrt{2}t} = \sigma_v \tag{1.3}$$

The corresponding Mohr circle for a point at the center of the wallet is centered at the origin of the Cartesian system of axis and the shear stress τ is equal to the principal tensile stress σ_t (Figure 1.32 [MLGB13]).

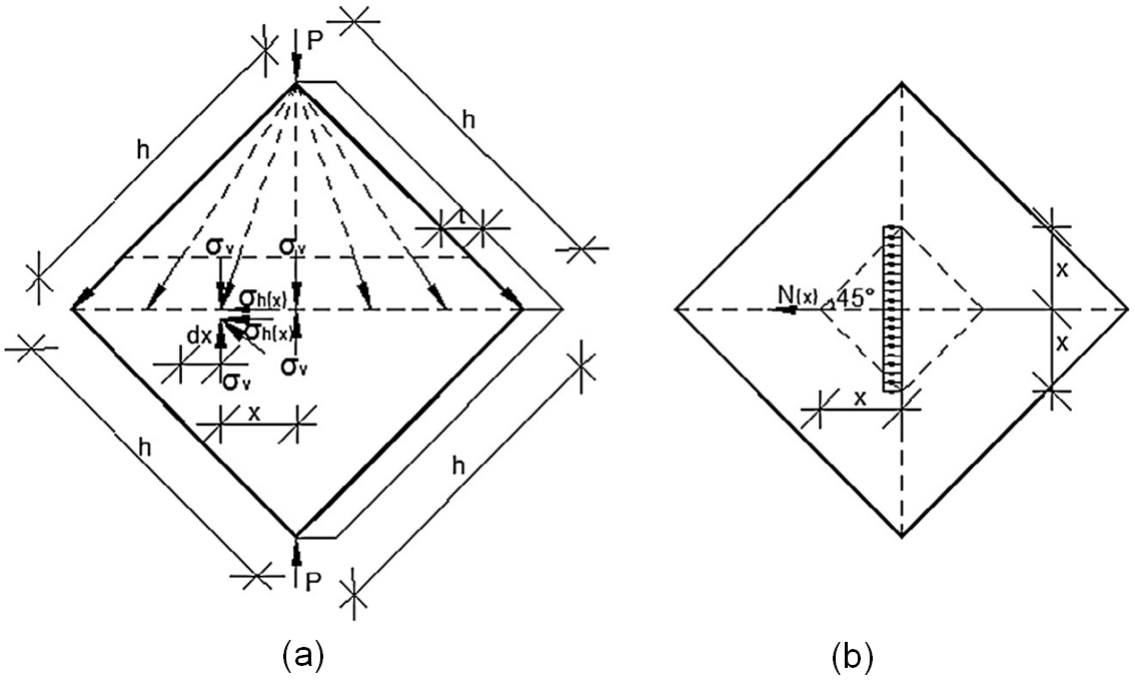

FIGURE 1.31: Internal stresses in the diagonal compression test; (a): Stress components within distance x from center and (b): Horizontal force within distance x from center [MLGB13]

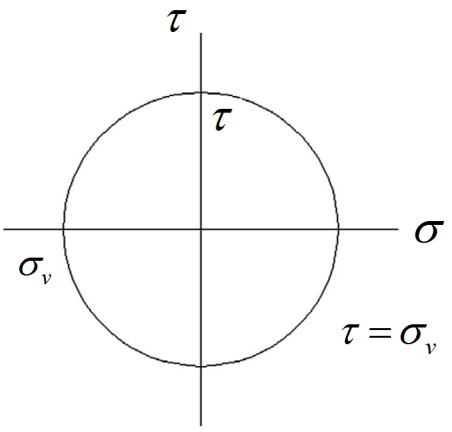

FIGURE 1.32: Mohr circle at the center of the wallet [MLGB13]

Then, the shear stress can be calculated by using the following relationship:

$$\tau = \frac{P}{h\sqrt{2}t} \tag{1.4}$$

where τ is the shear stress on the net area (MPa), P is the applied load (kN), h is specimen height (mm), and t is specimen thickness (mm). The shear strain (shear distortion) can be calculated by using following equation:

$$\gamma = \frac{\Delta V + \Delta H}{g} \tag{1.5}$$

where γ is shear strain, ΔV is vertical shortening (mm), ΔH is horizontal extension (mm), and g is gauge length (mm).

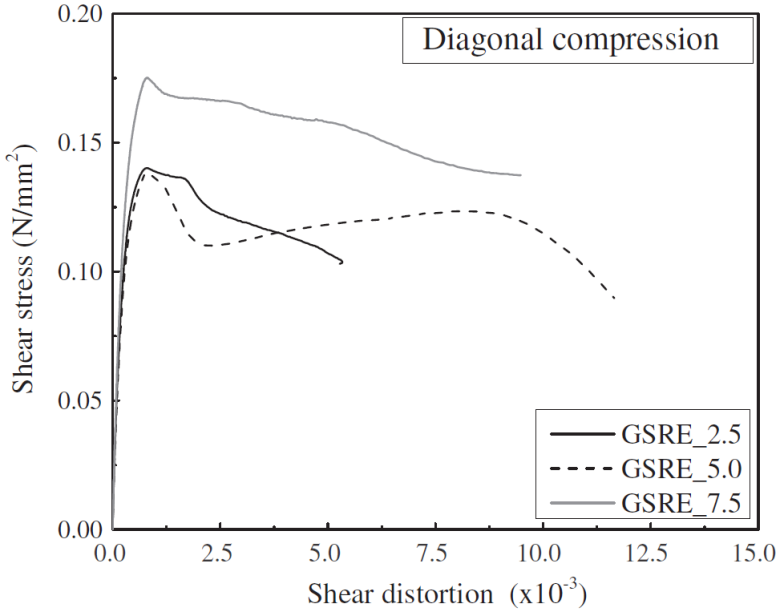

FIGURE 1.33: Shear stress vs shear distortion in a diagonal compression tests [SOM+13]

Diagonal compression test is a typical test to study the shear strength of rammed earth panels. For example, Silva et al. and Miccoli et al. [SOS+14, MOS+14] used a diagonal compression test to study the shear strength of unstabilised rammed earth. The diagonal compression tests allowed verifying a large shear deformation capacity which is thought to result from friction and interlocking of the coarse aggregates. Silva et al.[SOM+13] used a diagonal compression test on rammed earth stabilised by fly ash. The fly ash content varied from 2.5%, to 7.5% of the soil weight. The results from diagonal compression tests are given in Figure 1.33. It is found that stabilisation with fly ash gives a shear strength higher than that reported for URE (0.037MPa) and significantly higher than that reported for adobe masonry (0.022-0.032MPa)[SOM+13].

1.4.4 Role of interfaces in rammed earth systems

Interfaces between different layers are produced from the consecutive compaction process in rammed earth. In general, the existence of interfaces is supposed to constitute a weaker zone in the rammed earth system under loading. It may be due to a smaller density as in the layer where the material is better compacted.

To investigate the interfaces strength in rammed earth, El Nabouch et al. [EN17] carried out a direct shear test on a large shear box with samples size measuring 49cm x 49cm x 45cm. The test results is depicted in Table 1.4. The author found that the interfaces friction angle is about 90% of the friction angle in the layers. In addition, the cohesion of interfaces is found to be approximately equal to 80% of the cohesion in the layer. From the direct shear tests, the shear stiffness (k_s) were estimated (Figure 1.34). It led to a value of about 16.7MPa/m which is significantly lower than the one suggested by Miccoli et al. [MOS+14] which is in the order of 76GPa/m for E=760MPa. A possible cause of this small value of this elastic interface stiffness is due to the value of water content of the material at the time when the test was carried out which was on the order of 4-6%. This level of water content is quite different from typical on site water content which is on the order of 3% [EN17].

TABLE 1.4: Direct shear test data [EN17]

Type of test	Dimensions of specimens (cm)	ϕ_{layer} (°)	$\phi_{\text{interface}}$ (°)	C_{layer} (kPa)	$C_{\text{interface}}$ (kPa)
Large shear box	49 x 49 x 45	35.3	32.9	30.3	24.7

Note: water content at test 4-6%

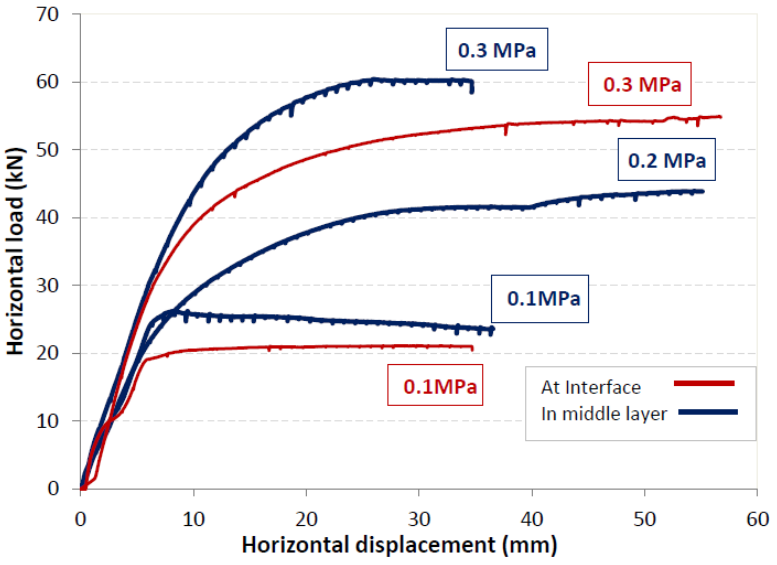

FIGURE 1.34: Horizontal load vs horizontal displacement of the loading platen; large shear box test [EN17]

Finally, another study was conducted by Holur et al. [Hol16] on the influence of the moisture content on the interface shear strength. Three conditions of moisture were defined; oven dry (0% moisture at test), ambient state ($w = 1 - 2\%$), and moist state (water content $> 4\%$). From the study, it is shown that the specimen at the dry state had the higher mechanical strength. The shear strength at the

interface was lower in the case of the specimen with the higher moisture content at the testing time. This is not surprising, since the more water content is introduces the lower suction will be obtained and hence the lower strength will be observed.

1.4.5 Lateral resistance of wallets

A pushover test can be used to estimate the resistance of wallets under a lateral loading. In this test, a wallet with a certain dimension is loaded uniformly in the upper part then laterally pushed on the wall head until failure. The walls subjected to this kind of loading are known as shear walls due to the predominance of the shear efforts. A shear wall behaves as a free standing cantilever or fixed end structural element and its stiffness depends on its aspect ratio which is defined as the relation between the height and length of the wall. In fact, the aspect ratio has a great influence on the failure mode of the walls. For low aspect ratios, shear failure predominates, whereas flexural behaviour governs the in-plane behaviour of slender walls [Haa09]. Figure 1.35 shows the distinct crack patterns associated to different stress states exhibited by shear walls.

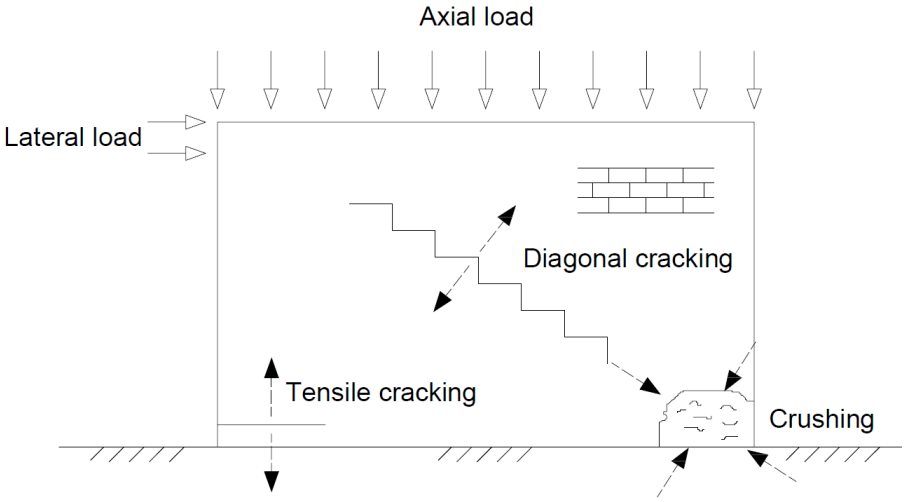

FIGURE 1.35: Typical cracking patterns of wall in the pushover test [Haa09]

1.4.5.1 Pushover test - monotonous

El Nabouch et al. [NBP+16] used this type of pushover test to estimate the seismic performance of a rammed earth wall. In this pushover test, a wallet is pushed laterally until failure. Two different wallet dimensions were used; 1500x1500x250mm^3 (Wall-2 and Wall-3) and 1000x1500x250mm^3 (Wall-1 and Wall-4). A vertical pressure equal to 0.3MPa was used to represent the typical pressure for a two storeys

house. During the test, the displacements field on the wallet are captured by using image processing (Figure 1.36). This method allows to obtain Young modulus using the following formula:

$$E_{wall} = \frac{\Delta F.H}{A.\Delta H} \tag{1.6}$$

where ΔF is the force increment, H is the reference height, A is the area loaded by the vertical loading, and ΔH is the vertical change of reference height. Table 1.5 shows the Young modulus for the material obtained from image processing method.

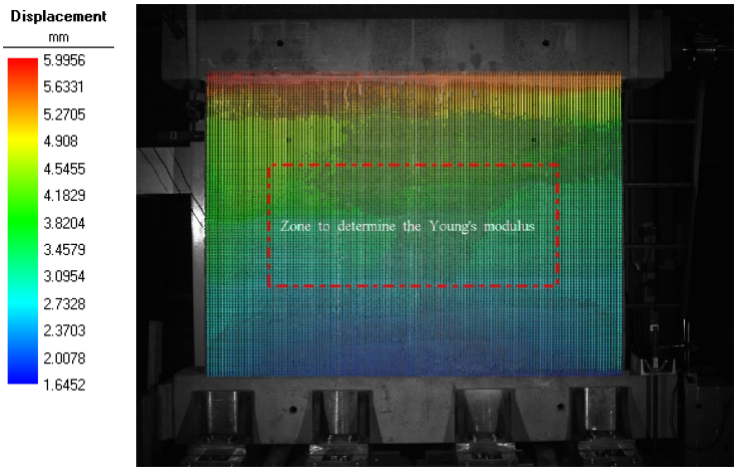

FIGURE 1.36: Displacement field of the wall [EN17]

TABLE 1.5: Young modulus of the wall based on image processing [EN17]

Wall number	Young modulus (MPa)
Wall 1	375 MPa ±20
Wall 2	391 MPa ±30
Wall 3	435 MPa ±25
Wall 4	440 MPa ±15

The pushover tests results are depicted in Figure 1.37. An unexpected wallet weakness was revealed during the test on wall-1 at the bottom of the wallet which led to a lower loading capability compared to the other walls. The initial curves for wall-2 and wall-3 that hold the same dimensions are similar but after a horizontal displacement of 3mm, wall-2 become less resistant than wall-3. This might be caused by some defects that appears somewhere in the body of the wall.

Figure 1.38 shows the force-displacement curve and also the crack pattern in the wall-2 at different loading stages from image processing. The maximum resistance was reached at the level of 40kN with a corresponding displacement of 15mm. In

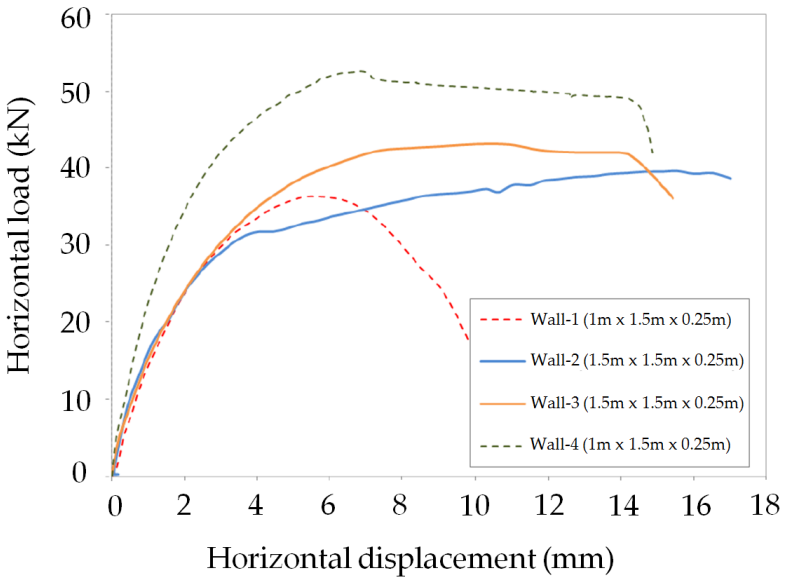

FIGURE 1.37: Pushover test results [EN17]

addition, three stages of crackings are shown in Figure 1.38. At first, some cracks are observed at the bottom left of the wall (loading is at top right). Then at the second stage, a vertical but slightly inclined crack appears and crushing at bottom left develops. Finally, the main crack developed with quasi diagonal pattern and a detachment were reported at the lower right base of the wallet.

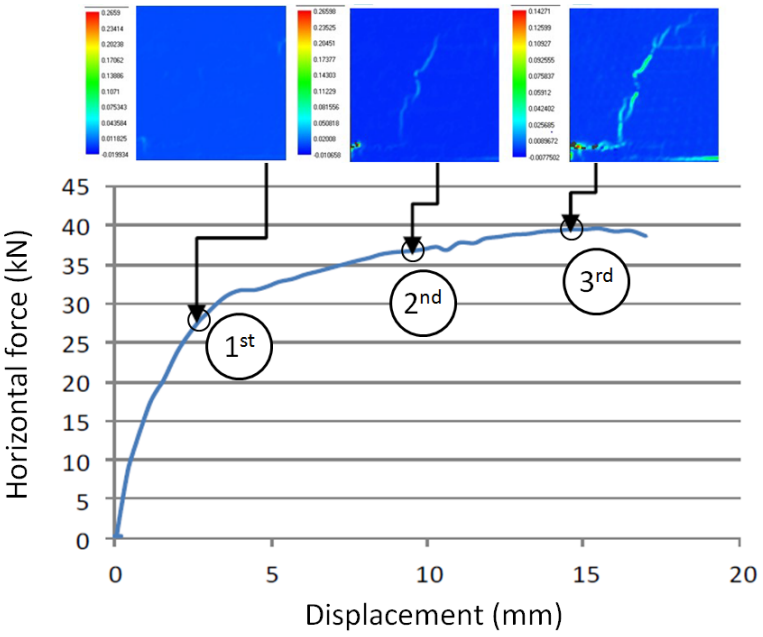

FIGURE 1.38: Crack pattern and load-displacement curve throughout a pushover test; wall-2 [NBP+16]

1.4.5.2 Pushover test - cyclic

In the cyclic pushover test, the horizontal loading is applied within two opposite directions. This type of test is close to the loading conditions of a wall subjected to an earthquake. Arslan et al. [AEY17] and Miccoli et al. [MDM16] used this type of pushover test on rammed earth wall to evaluate seismic behaviour of earth wall.

In the works of [AEY17], rammed earth wall measuring 1500x1500x200mm^3 is used and loaded horizontally with a drift ratio ranging from 0.15% to 6.5%. Hysteretic load-displacement curves obtained from a lateral reversed cyclic loading are given in Figure 1.39 for an unstabilised rammed earth panel. The behavior of the test wall are symmetrical for push and pull directions in the range of tested displacements.

The load carrying capacities and the corresponding displacements of unstabilised rammed earth for push and pull directions are 52kN-37mm and 54kN-39mm, respectively. In addition, the average load values at 1.0% and 3.5% drift ratios were respectively found equal to 40kN and to 50kN. The crack patterns after a pushover test are shown in Figure 1.40 where horizontal cracks are observed through some layers of the wallet. This might be occur due to the absence of confining pressure on the upper part of the wall and due to the lower resistance of the interfaces between compacted layers.

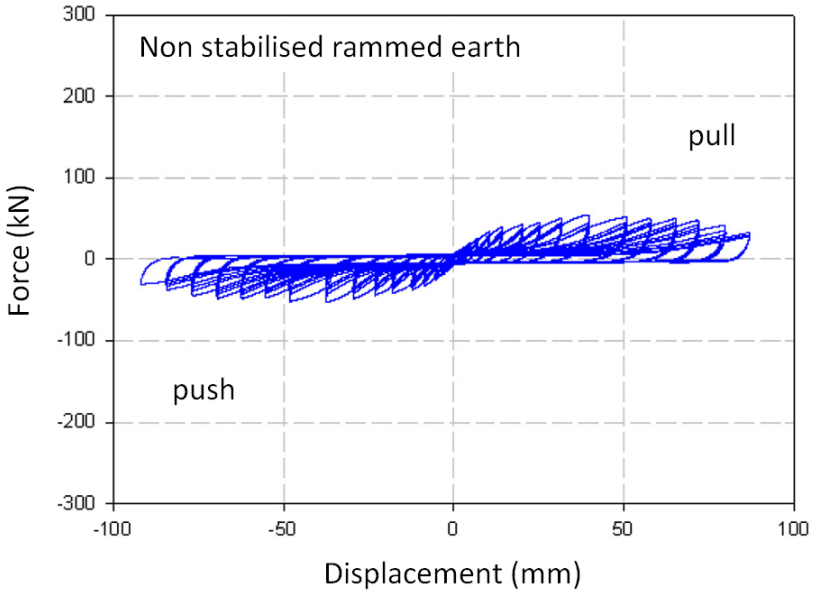

FIGURE 1.39: Load-displacement responses throughout a pushover test [AEY17]

FIGURE 1.40: Crack pattern after pushover test for unstabilised rammed earth [AEY17]

1.5 Conclusion

Rammed earth construction is created by mechanically compacting in several layers locally collected humid earth. This vernacular building technique is present worldwide and specifically in the Auvergne-Rhône-Alpes region (France). Though answering some issues raised by the Sustainable Development, several barriers have to be solved for the use of this technique for new buildings or for the repair of existing ones. This technology has not benefited from a century of studies, researches and feedback like more conventional techniques including concrete. However, lately, a certain number of scientific works devoted on the basic mechanical of rammed earth including compression, tensile, and other deviatoric stress paths emerged.

In relation to the mechanical behavior of rammed earth, in a first approach, it can be considered that the material behaves as a quasi-brittle material like concrete. Although it has different material constituents, the compression and tensile test results show similar pattern that were found for concrete. The particularity of rammed earth lies in the strong influence of the humidity or the water content that allows suction (capillary forces) to bind the different elements of the material. Other particularity lies in the existence of interfaces between the compacted layers that tend to weaken the resistance of rammed earth panels. The similarities and differences of behavior between rammed earth and concrete has not been totally addressed so far. However, the set of existing tests in the literature allows the design of a constitutive model relevant to rammed earth to be performed.

Chapter 2

Modelling system with quasi-brittle materials

2.1 Constitutive models

Apart from laboratory tests and site measurements that help to understand the behavior of materials and of structures at different scales, modelling helps to estimate safety factors against failure and to optimise sections. At this stage a constitutive model for the material is required, which is in this work rammed earth. At service, the earth has a very low water content, typically on the order of 2-4% [BMHW14]. In this range of water content, where suction plays the role of a strong binder between particles, rammed earth has some basic features of a quasi-brittle material such as concrete. Then, even if the strength of rammed earth is far lower than that of an usual concrete, one may be inclined to use a constitutive model valid for quasi-brittle materials (with probable adaptations) in this case. This chapter describes typical continuum constitutive models for quasi-brittle materials that can be used to model the mechanical behaviour of rammed earth.

There are mainly three approaches that can be taken at the macroscopic level as depicted in Figure 2.1 [JHPCG06]. First, there are models built upon the continuum damage mechanics theory (elastic theory) where elastic properties decrease according to damage variables (Figure 2.1a). Secondly, there exist models based on the plasticity theory where permanent deformations can be generated when the system is at yield (including possible failure) (Figure 2.1b). Finally, the last approach couples the continuum damage theory to plasticity (Figure 2.1c).

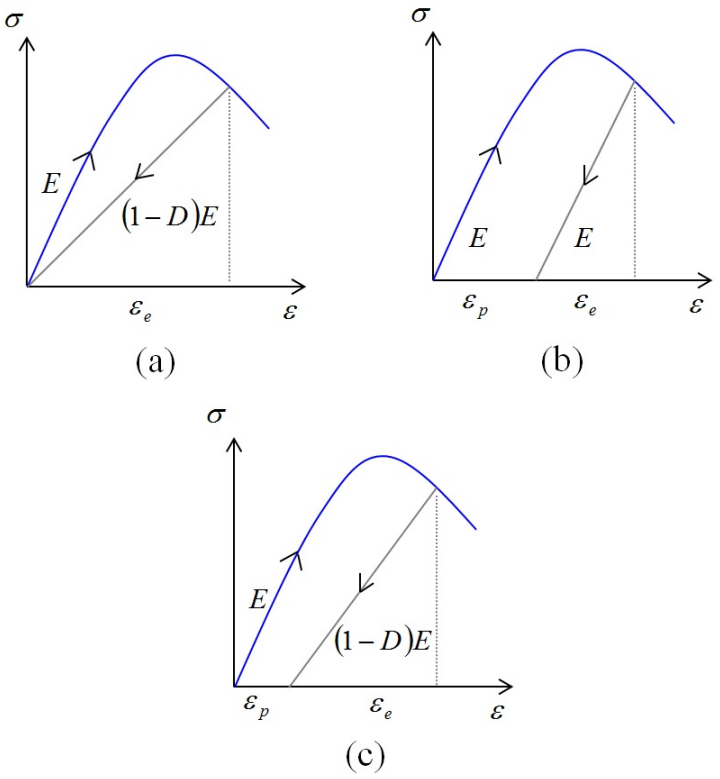

FIGURE 2.1: Typical loading and unloading responses for three different constitutive models; (a) : elastic-damage model, (b): elastic-plastic model, and (c): elastic-plastic-damage model [JHPCG06].

2.1.1 Damage model

A damage model involves constitutive relationships in which the mechanical effect of cracking and void growth is introduced through internal state variables which monitor the decrease of the elastic stiffness of the material [TB12] when loading. Generally, the underlying damage variable is defined as the ratio between the damage area surface of a tested sample to the overall material surface area of this sample. It can be a scalar, a set of scalars, or a tensor. Damage can be isotropic as in the work of Mazars [Maz86, MHG15] or anisotropic as proposed by Zhou [ZZLY02] or Cicekli et al. [CVAR07].

A simple isotropic damage continuum model describes the material degradation by means of a single scalar damage parameter D which grows monotonously from zero (undamaged material) to one (completely damaged material). The growth of damage is controlled by a threshold parameter κ which is defined as the maximum equivalent strain $\tilde{\varepsilon}$ reached during the load history up to time t. The equivalent strain $\tilde{\varepsilon}$ can be defined based on the maximum principal effective stress as [JM05]:

$$\tilde{\varepsilon} = \frac{\max(\sigma_i^{\text{eff}})}{E} \tag{2.1}$$

or by modified Rankine criterion as:

$$\tilde{\varepsilon} = \frac{\sigma_1^{\text{eff}} - c(-\sigma_2^{\text{eff}})}{E} \tag{2.2}$$

with σ_1^{eff} and σ_2^{eff} are respectively the first and second principal effective stress ($\sigma_1^{\text{eff}} > \sigma_2^{\text{eff}}$). c is a non-negative coefficient. If c is equal to zero, Equation (2.2) degenerates into Equation (2.1). Note that effective stress is defined as the stress acting in the undamaged material.

The general loading function of a damage model writes:

$$f(\tilde{\varepsilon}, \kappa) = \tilde{\varepsilon} - (\max(\kappa, \kappa_0)) \tag{2.3}$$

where κ_0 is the initial value of κ when damage begins. Damage develops if the loading function f is positive. Throughout a monotonous loading, the variable κ increases (it coincides with $\tilde{\varepsilon}$) and during unloading and reloading it remains constant. Peerlings [PDBBG98] defines a damage evolution in the tensile regime as:

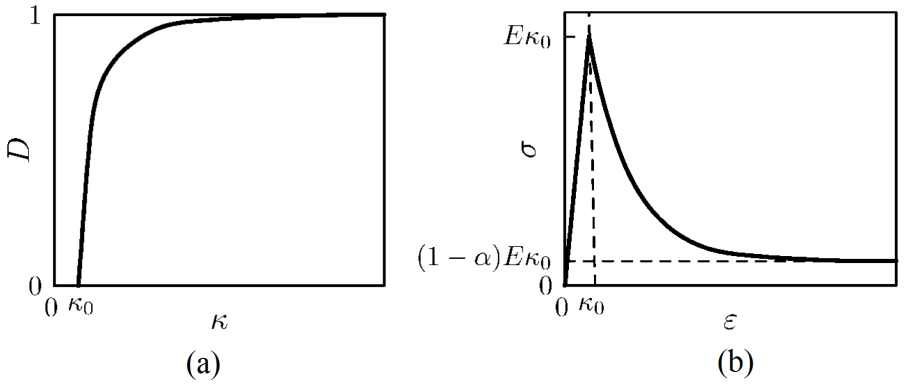

FIGURE 2.2: a) Damage variables D as a function of κ, b) Stress-strain response during uniaxial tension [PDBBG98]

$$D = 1 - \frac{\kappa_0}{\kappa}(1 - \alpha + \alpha * e^{-\beta(\kappa - \kappa_0)}) \tag{2.4}$$

with κ_0 is the damage threshold parameter and α, β are model parameters. Parameter β determines the rate at which damage grows. A higher value results in a faster growth of damage and thus in a more brittle response. The use of Equation (2.4) gives a typical stress-strain response as in Figure 2.2 where damage starts

once the system reaches failure.

In the following subsection, two typical damage models which are used to capture the behaviour of quasi-brittle materials are discussed. First, Mazars model is described followed by the Total Strain Rotating Crack model.

2.1.1.1 Mazars model

One of the most famous damage models for concrete was designed by Jacky Mazars and is called Mazars model [Maz86]. The relationship between stress and strain in Mazars model is given by the following equation:

$$\boldsymbol{\sigma} = (1 - D)E\boldsymbol{\varepsilon}^e \tag{2.5}$$

where E is the Hooke matrix, D is the damage variable, and $\boldsymbol{\varepsilon}^e$ is the elastic strain. The elastic strain is computed as:

$$\varepsilon^e = \varepsilon - \varepsilon^{th} - \varepsilon^{rd} - \varepsilon^{re} \tag{2.6}$$

with ε^{th} is the thermal dilation, ε^{re} is the shrinkage related to hydration, and ε^{rd} is the shrinkage related to drying. Both are strain components of phenomena that are known to initiate cracks within concrete. In order to model different responses along a tensile and compression stress path, the damage variable D in Equation (2.5) is split into a tensile part D_t and compression part D_c:

$$D = \alpha_t D_t + \alpha_c D_c \tag{2.7}$$

with weight coefficients α_t and α_c defined as functions of principal strains in tension ε_i^t and principal strains in compression ε_i^c.

$$\alpha_t = \sum_{i=1}^{3} \left(\frac{\langle \varepsilon_i^t \rangle \langle \varepsilon_i^e \rangle_+}{\tilde{\varepsilon}^2} \right)^\beta \qquad \text{and} \qquad \alpha_c = \sum_{i=1}^{3} \left(\frac{\langle \varepsilon_i^c \rangle \langle \varepsilon_i^e \rangle_+}{\tilde{\varepsilon}^2} \right)^\beta \tag{2.8}$$

Therefore if the stress state corresponds to a compressive state then $\alpha_t = 0.0$ and if the stress state corresponds to a tensile state then $\alpha_c = 0.0$. $\tilde{\varepsilon}$ is the equivalent strain which is given by:

$$\tilde{\varepsilon} = \sqrt{\sum_i \langle \varepsilon_i^e \rangle_+^2} \tag{2.9}$$

with ε_i is the principal strain and $\langle\rangle_+$ is the positive operator where:

$$\begin{aligned} &\text{if } \varepsilon_i < 0.0 \quad &&\text{then} \quad &&\langle\varepsilon_i\rangle_+ = 0.0 \\ &\text{if } \varepsilon_i \geq 0.0; \quad &&\text{then} \quad &&\langle\varepsilon_i\rangle_+ = \varepsilon_i. \end{aligned} \tag{2.10}$$

β is the parameter used to reduce the effect of damage under a shear loading compared to a tensile loading. The evolution of damage is ruled by the following relationships:

$$\begin{aligned} D_t &= 1 - \frac{\kappa_0(1-A_t)}{\kappa} - \frac{A_t}{\exp(B_t(\kappa-\kappa_0))} \\ D_c &= 1 - \frac{\kappa_0(1-A_c)}{\kappa} - \frac{A_c}{\exp(B_c(\kappa-\kappa_0))} \end{aligned} \tag{2.11}$$

where κ_0 is the initial value of κ when damage begins as in Equation (2.3). The value of κ is related to the equivalent strain $\tilde{\varepsilon}$.

Mazars model holds eight model parameters: two elastic parameters (E and ν) and six damage parameters (κ_0, β, A_t, B_t, A_c, and B_c). The set of parameters can be obtained from compression and tensile tests.

The latest improvements in Mazars model were aimed to take into account strain rate effects and confinement effects [MHG15]. It was designed to handle concrete responses under severe loading cases such as blasts, earthquakes and impact loads. Indeed, such aspects can be critical in the case of like power plant, nuclear reactor, or concrete dam.

Bui et al. [BBLM14] used Mazars model to simulate the behavior of rammed earth wallets under a compression loading. Figure 2.3 shows the comparison of the load-displacements between experiments and the simulation. Is is shown that Mazars model was able to retrieve the initial stiffness and the level of the maximum response of the stress-strain curve that was found throughout experiments. Mazars model also captured well the absorbed energy during the damage process (Figure 2.4). On the other hand, the pre-peak and post-peak behaviour was not retrieved correctly. In Mazars model, no permanent strain can be generated, thus when unloading, the stress-strain response will return to the origin. This feature can be acceptable when unloading after a tensile loading path but not when unloading after a compression loading path [Jir11]. Nevertheless, Mazars model remains popular in terms of applications because it is relatively simple to handle, stable and computationally efficient.

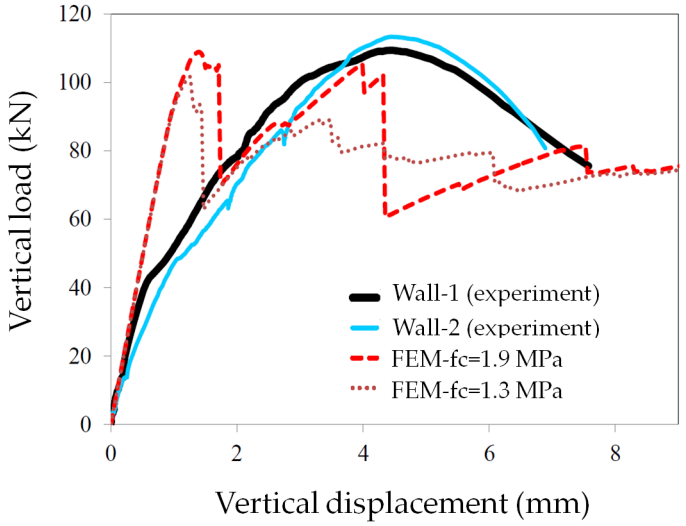

FIGURE 2.3: Comparison between experiments and simulations of a compression test on a rammed earth wallet using Mazars model [BBLM14]

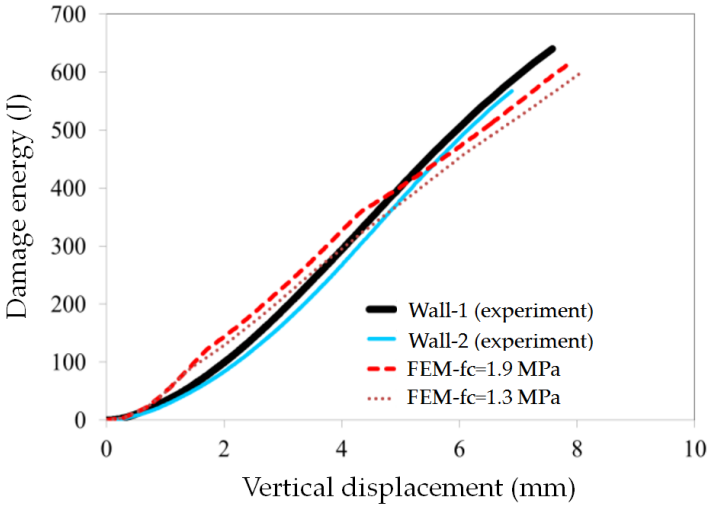

FIGURE 2.4: Energy absorbed in the wallets during the damage process; comparison simulations using Mazars model and experiments [BBLM14]

2.1.1.2 Total strain rotating crack model

The Total Strain Rotating Crack Model (TSRCM) is another constitutive model based on damage which is induced by cracks. The TSRCM follow a smeared cracks approach for the fracture energy [BV10]. It corresponds to a model of distributed and rotating cracks based on total strains, where the crack direction rotates with the principal strain axes [Fig83, Póv91, JZ98].

TSRCM belongs to the class of elastic-damage models since it involves the degradation of the elastic properties like in Mazars model. In the TSRCM, the degradation of the material due to cracking and crushing is monitored by six internal damage

variables α_k, collected through the vector α. Internal variables k = 1,...,n_{str} monitor the maximum strain whereas variables k = n_{str}+1,..., 2 x n_{str} monitor the minimum strain (Figure 2.5). It is assumed that damage is irrecoverable which implies that the absolute values of the internal damage variables are increasing.

The loading-unloading-reloading condition is monitored by r_k which is determined for both tension and compression to model the stiffness degradation in tension and compression. In a tension loading path r_k is given by:

$$\begin{aligned} &\text{if } \varepsilon_k > \alpha_k \quad \text{then} \quad r_k = 0.0 \\ &\text{if } \varepsilon_k \leq \alpha_k \quad \text{then} \quad r_k = 1.0 \end{aligned} \tag{2.12}$$

and in a compression loading path, r_k is written:

$$\begin{aligned} &\text{if } \varepsilon_k < \alpha_k \quad \text{then} \quad r_k = 0.0 \\ &\text{if } \varepsilon_k \geq \alpha_k \quad \text{then} \quad r_k = 1.0 \end{aligned} \tag{2.13}$$

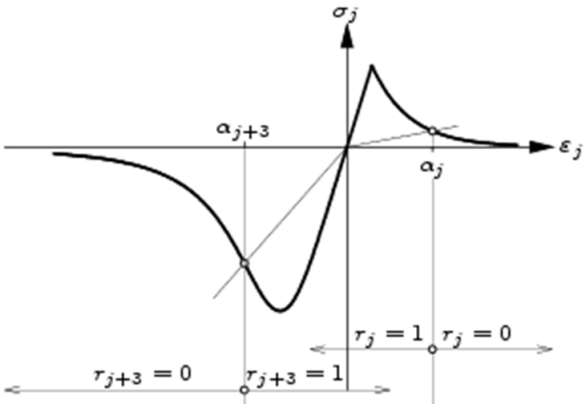

FIGURE 2.5: Loading and unloading responses with TSRCM [BV10]

In the rotating crack model, the strain is decomposed into an elastic strain and a crack strain. The elastic strain is related to the elasticity, while the crack strain is generated from up to three mutually orthogonal cracks that keep aligned with the principal direction [JZ98]:

$$\dot{\varepsilon} = \dot{\varepsilon}^e + \dot{\varepsilon}^c \tag{2.14}$$

where $\dot{\varepsilon}^e$ is the increment of the elastic deformation and $\dot{\varepsilon}^c$ is the increment of the cracks deformation. The latter one is defined by:

$$\dot{\varepsilon}^c = \boldsymbol{T}^e \boldsymbol{e}^c \tag{2.15}$$

with $\boldsymbol{T}^e$ the strain transformation matrix which transforms the principal strain into global strain components. $\boldsymbol{e}^c$ is the crack strain tensor corresponding to the individual principal strain directions. The TSRCM model can involve several possible non-linear stress-strain relationships according to the type of involved stress, either of compression or tensile type.

Along a compression stress path, a parabolic relationship of the stress-strain curve is used which is based on the fracture energy concept (Figure 2.6a). The second point of the parabolic relationship was defined at the level of $0.3f_c$ by taking into account the experimental Young modulus. The prepeak response in the compression regime is formulated by the following relationships:

$$f = f_c\left(\frac{1}{3}\right)\left(1 + 4\left(\frac{\alpha_j - \alpha_{c/3}}{\alpha_c - \alpha_{c/3}}\right) - 2\left(\frac{\alpha_j - \alpha_{c/3}}{\alpha_c - \alpha_{c/3}}\right)^2\right) \tag{2.16}$$

with $\alpha_{c/3}$ is the strain for the stress state corresponding to one-third of the maximum compressive strength f_c:

$$\alpha_{c/3} = \frac{1}{3}\frac{f_c}{E} \tag{2.17}$$

and α_c is the strain when the maximum compressive strength f_c is reached.

The peak and the post-peak responses is obtained through a parabolic curve:

$$f = f_c\left(1 - \left(\frac{\alpha_j - \alpha_c}{\alpha_u - \alpha_c}\right)^2\right) \tag{2.18}$$

with α_u the strain at the residual state when softening does not evolve anymore:

$$\alpha_u = \alpha_c\frac{3}{2}\frac{G_c}{hf_c} \tag{2.19}$$

where G_c is the fracture energy due to a compression loading and h is the characteristic length. The latter one can be defined by taking the square root of the element area for 2-D problem.

A stress-strain response along a compression stress path can also be retrieved using multilinear relationships. The tensile softening is assumed to be exponential as depicted in Figure 2.6b. The area under the tensile curve corresponds to a tensile I-mode fracture energy (G_f^I).

The TSRCM model involves six parameters: two elastic parameters (E and ν) and four parameters associated with cracks in the compression and tensile loading path (f_c, G_c, f_t, and G_f^I).

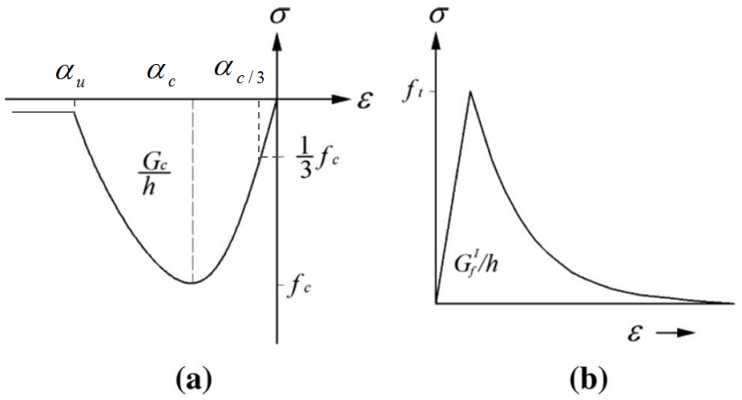

FIGURE 2.6: Total strain rotating crack model; (a): compression behaviour, (b): tensile behaviour [MOS+14]

The TSRCM has less number of parameters than Mazars model which gives less effort for the identification process. The introduction of the characteristic length (h) which is dependent on the mesh size is also useful to obtain mesh independent results. On the other hand, as in the Mazars model, the rotating crack model can not generate permanent deformations (Figure 2.5) which does not match experimental evidence.

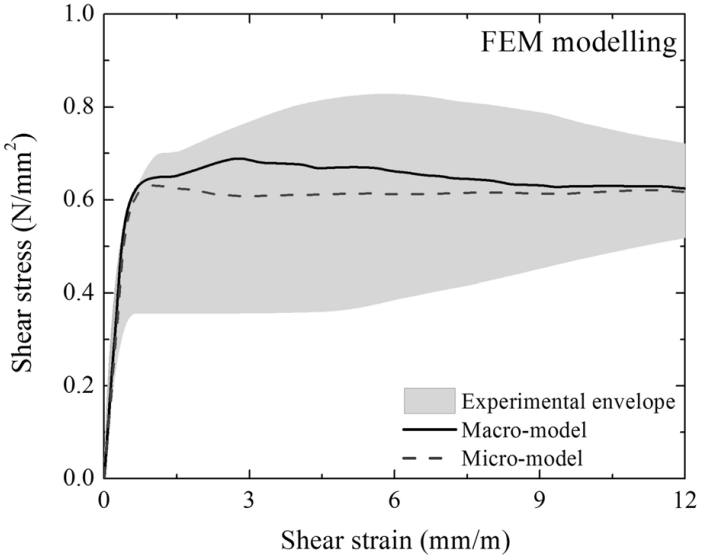

FIGURE 2.7: Comparison between experiments and simulations (TSRCM model) of a diagonal compression test on rammed earth wallets [MOS+14]

There are some existing works that used this model for rammed earth problem modelling, for example [MOS+14, SOS+14]. They used the TSRCM to model the behaviour of a rammed earth wallet throughout a diagonal compression test.

The wallet was modelled as a homogeneous model (macro-model) and also as non-homogeneous medium by introducing interfaces (micro-model) between compacted layers. Figure 2.7 shows the comparison between experiments and simulations by using these two approaches [MOS+14]. The results from the simulations were found within the average of the experiments envelope. One can note the broad departure of experimental responses between the different wallets due to the difficulty to create similar wallets with a same material. It is shown that interfaces did not bring about a significant improvement of the simulation of the experimental wallet response. It may be due to the chosen set of model parameters for the interfaces that is not enough different from the one for the layer (the parameters were stated) but one must also remind that the interfaces are partly loaded normally in the case of diagonal compression test. On that case, their role is less significant than when they are loaded parallel to them.

2.1.2 Elasto - plastic model

The second approach related to the constitutive models belongs to the framework of plasticity. The classical theory of plasticity grew out of the study of metals in the late nineteenth century. It started with the works of Tresca in 1864, when he undertook an experimental program into the extrusion of metals and published his famous Tresca yield criterion for metals [Hil98]. In metals and other crystalline materials the occurrence of plastic deformations at the micro-scale level is due to the motion of dislocations and the migration of grain boundaries on the micro-level. In sands and other granular materials plastic flow is due both to the irreversible rearrangement of individual particles and to the irreversible crushing of individual particles. In quasi brittle materials, permanent deformation might be exists due to the irreversible process of cracks opening in the system.

The basic assumption of plasticity is that the increment of the total deformation is decomposed into an elastic and a plastic part as:

$$\dot{\boldsymbol{\varepsilon}}^{total} = \dot{\boldsymbol{\varepsilon}}^{e} + \dot{\boldsymbol{\varepsilon}}^{p} \tag{2.20}$$

where $\dot{\varepsilon}^e$ is the increment of the elastic deformation and $\dot{\varepsilon}^p$ is the increment of the plastic deformation. Mohr-Coulomb model and Drucker-Prager model are two of typical plastic models used for modeling the behavior of geomaterials. According to [VDB84], Drucker-Prager model is suitable for the case of soft clay with a low friction angle. In other cases, Mohr-Coulomb model is generally used as a first approach to model possible irreversible strains in geotechnical boundary value problems. There is also the Cam-Clay model for clay which is very typical.

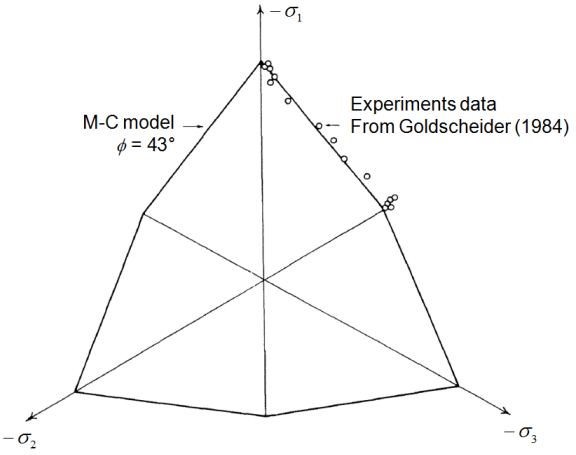

FIGURE 2.8: Stress states at failure from actual triaxial tests on a dense sand compared to Mohr Coulomb failure surface ([VDB84])

2.1.2.1 Mohr-Coulomb model

The popular elasto-plastic constitutive Mohr-Coulomb model is a constitutive model used to represent shear failure in soils and rocks. Vermeer and de Borst [VDB84] reported laboratory test results for sand and concrete that match well with Mohr-Coulomb model (Figure 2.8). Mohr-Coulomb model holds five model parameters: two related to Hooke law (Young modulus and Poisson ratio) and three plastic parameters (friction angle ϕ, cohesion c, dilatancy angle ψ). Mohr-Coulomb failure surface which is a plastic surface writes:

$$f = -\sigma_1 + \sigma_3(N_\phi) - 2c\sqrt{N_\phi} \qquad \text{with} \qquad N_\phi = \frac{(1+\sin\phi)}{(1-\sin\phi)} \tag{2.21}$$

where σ_1 is the major principal stress, σ_3 is the minor principal stress. In Equation (2.21), the intermediate principal stres is not involved in the plastic criterion which is the characteristics and the drawback of Mohr-Coulomb model [VDB84].

Figure 2.9 shows the shape of the Mohr-Coulomb failure surface in the principal stress space. It is noticed that the irregular shape of Mohr-Coulomb model gives a problem of numerical convergence. This problem can be overcome using a modified Mohr-Coulomb model, such in Abbo et al. [AS95]. Nevertheless, several authors used Mohr-Coulomb model to study the behaviour of rammed earth systems, for example [Jaq08] and [BBLM16]. Jaquin et al. [Jaq08] used this model to capture the in-plane failure of rammed earth walls observed in the lab tests. According to these authors, it is possible to used Mohr Coulomb model to represent the behaviour of rammed earth walls including a refinement by modelling the interfaces between different compacted layers. In this latter case, it was assumed that the

strength of the interface layer was proportional to the normal load across it.

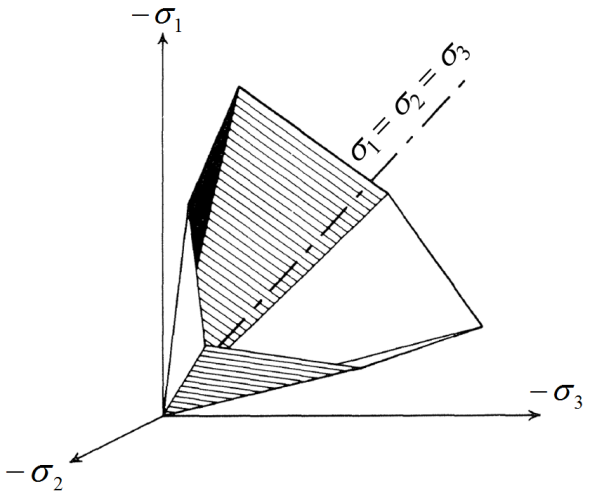

FIGURE 2.9: Failure surface of Mohr-Coulomb model in the principal stress space [VDB84]

Bui et al. [BBLM16] studied the behaviour of rammed earth walls by using a three dimensional Discrete Element Method (3D-DEM). The failure envelope used in their study was the Mohr-Coulomb criterion with a tension cut-off (Figure 2.10). The failure surface consists of two sub-surfaces which correspond to a shear plastic failure (line A-B) and tensile plastic failure (line B-C). The basic version of Mohr-Coulomb model does not involve either hardening or softening in the shearing mechanism. Moreover, by default, the tensile failure is characterized as a sudden softening where the tensile strength σ^t is reset to zero. By using Mohr Coulomb model for the earth mass and the interfaces, Bui et al. [BBLM16] found that Mohr Coulomb model could capture the peak response and also the initial stiffness of the stress-strain curve throughout a compression test on a wallet (Figure 2.11).

Simulations were also performed for the case of a diagonal compression test on wallets. The experiments reference for the study was taken from the works of [SOM+13] on rammed earth walls stabilised by fly ashes. Two modellings were performed, one considering the wallet as a homogenous material and another approach were the interfaces between successive compacted layers of earth were modelled. The result of the simulations is given in Figure 2.12. The pre-peak behaviour of the wall using interfaces leads to a softer behaviour than when the wall is considered as a homogenous system, which fits the experiments better. However, it induces an oversized softening. The fluctuations of the simulations are generally due to a too large loading velocity in the simulations or to a state that is far from the equilibrium. However, on the overall, there is no significant differences between a simulation with and without interfaces.

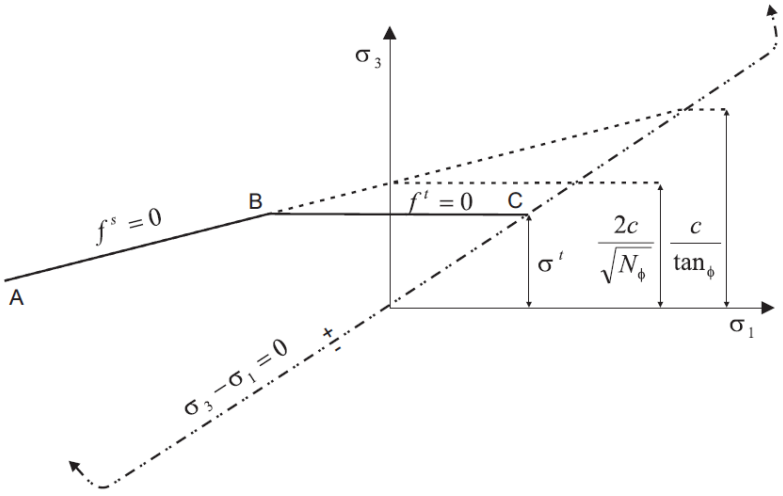

FIGURE 2.10: Mohr Coulomb failure criterion in the plane σ_1 and σ_3 with tension cut-off [Ita09]

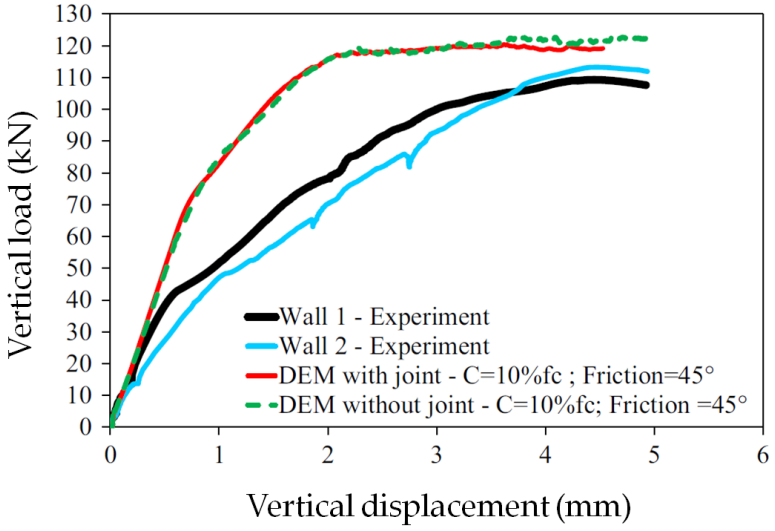

FIGURE 2.11: Comparison between experiments and simulations; case of compression tests on wallets [BBLM16]

2.1.3 Elastic - plastic - damage model

Damage mechanics models or plasticity models cannot retrieve, when they are used separately, the different phenomena at stake in quasi brittle materials. Plasticity is based on constant elastic properties and cannot model any evolution of reversible properties due to damage mechanisms (stiffness degradation due to the accumulation of microcracks). On the other hand, damage mechanics is not able to model irreversible deformations due to the creation of cracks when loading the material.

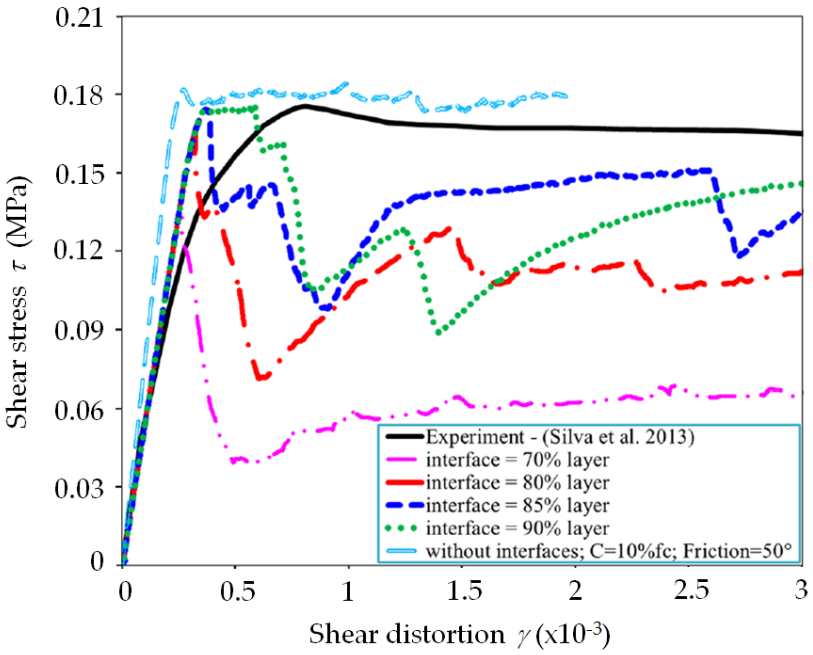

FIGURE 2.12: Comparison between experiments and simulations; case of the diagonal compression tests on wallet [BBLM16]

A plastic damage model takes into account both plasticity and degradation of the elastic properties. This class of constitutive model was used for studies involving concrete. For example, Lee and Fenves [LF98] developed a plastic damage constitutive model for the seismic analysis of concrete dams. A simple scalar degradation model was used to simulate the effects of damage on the elastic stiffness and the stiffness recovery after cracks closure. The plastic part was written on the basis of the effective stresses (undamaged part) and damage is monitored by a function of the plastic strain. Similar works were also performed by Grassl and Jirasek [GJ06].

The general stress-strain relationship for this class of models writes:

$$\sigma = (1-\omega)\mathbf{D_e} : (\varepsilon - \varepsilon_p) = (1-\omega)\bar{\sigma} \tag{2.22}$$

where ω is the damage variable (which evolves between 0 and 1), $\mathbf{D}_e$ is the elastic stiffness and $\bar{\sigma}$ is the effective stress.

If $\omega = 0$, Equation (2.22) reduces to the stress strain of an elasto-plastic model, whereas if $\varepsilon_p = 0$, the model becomes a purely elastic damage model. The plastic part of the model is based on the standard theory of plasticity, where all the equations are written in terms of the effective stress while damage is generated through a function involving the plastic strain. The plastic damage model in the work of [JHPCG06] belongs to this class of model, and therefore will be further studied.

2.1.3.1 Plasticity mechanism

The plastic mechanism is formulated in a three-dimensional framework with a pressure-sensitive yield surface, hardening, and non-associated flow rule. The components of it are the yield function, the flow rule, and the evolution law for the hardening variable.

The yield function is defined as:

$$F = \overline{\rho}^2 - \frac{\hat{k}\overline{\rho}_c^2}{r^2} \tag{2.23}$$

with $\overline{\rho}$ is the normalised deviatoric effective stress invariant. $\hat{k}$ is the hardening function which quantifies the growth of the loading surface with respect to the plastic deformation which reads:

$$\hat{k} = k^{2p}\left(1 - \frac{\overline{\xi}^2}{\xi_h^2}\right) \tag{2.24}$$

with

$$\xi_h^2 = \frac{A}{1-k} \qquad \text{and} \qquad k = k_0 + (1 - k_0\sqrt{k_h(2-k_h)}) \tag{2.25}$$

where p, A, and k_0 are three parameters of the model. $\overline{\rho}_c$ is the deviatoric invariant given as

$$\overline{\rho}_c = \left(\frac{1}{6}\right)^{\gamma}\sqrt{\frac{2}{3}}\left(-n + \sqrt{n^2 - 12\sqrt{3}n\overline{\xi} + 36}\right)^{\gamma} \tag{2.26}$$

with

$$n = \frac{3(1-\overline{f}_t^{\gamma})}{\overline{f}_t + \overline{f}_t^{\gamma}} \qquad \text{and} \qquad \overline{f}_t = \frac{r_t}{r_c} \tag{2.27}$$

where γ, r_t, and r_c are model constants. r is the deviatoric shape function which corresponds to an elliptic surface as:

$$r = \frac{2d_0}{d_1 - \sqrt{d_1^2 - 4d_0d_2}} \tag{2.28}$$

where d_0, d_1, and d_2 are the geometric variables depending on the Lode angle (θ). Figure 2.13 shows the shape of the failure surface for different stress paths. At

this stage, the internal variable k_h has reached the limit and thus the hardening process is over.

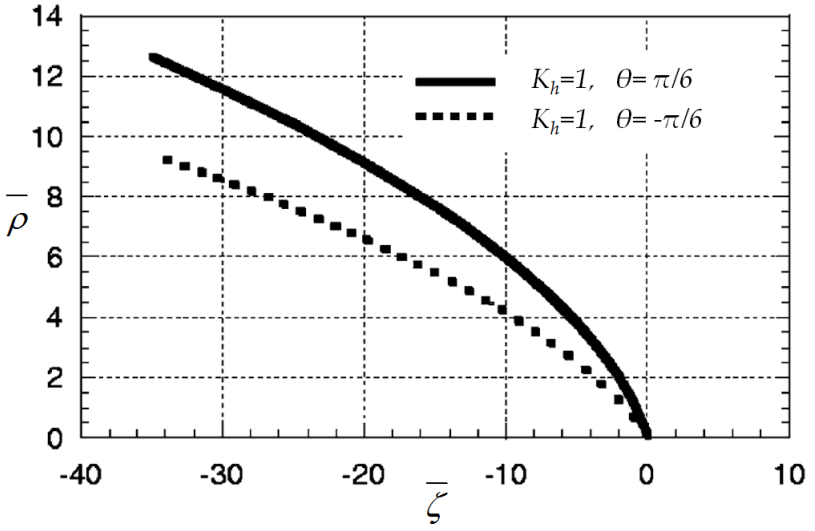

FIGURE 2.13: Failure surface for two different stress paths [JHPCG06]

2.1.3.2 Damage part

Damage within the material is defined based on the isotropic damage model from Mazars. The damage evolution was controlled by equivalent strain ε_{eq}. The damage loading surface is defined as

$$g(\varepsilon^e, D) = \tilde{d}(\varepsilon^e) - D \tag{2.29}$$

where D is a variable taking the maximum value of $\tilde{d}$ during a loading process given by

$$D = \max(\tilde{d}, 0) \tag{2.30}$$

with $\tilde{d}$ is the evolution law which separates the mechanical responses in tension and compression. Thus,

$$\begin{aligned} \text{if } \varepsilon_{eq} \geq \varepsilon_{D0} \quad & \text{then} \quad \tilde{d} \neq 0.0 \\ \text{else} \quad & \text{then} \quad \tilde{d} = 0.0 \end{aligned} \tag{2.31}$$

For the complete description of the plastic damage model by [JHPCG06], seventeen model parameters must be identified with two elastic parameters (E and ν), five damage parameters (A_t, B_t, A_c, B_c, and ε_{D0}) and ten plastic parameters (r_c,

r_t, p, B_h, C_h, A, α, γ, A_h, and k_0). This large amount of parameters are directly related to the refinement of the model and the phenomena that are supposed to be retrieved.

It can be noted that for tensile loading, damage and plasticity are initiated when the equivalent applied stress reaches the uniaxial tensile strength f_t. Whereas under compressive loading, damage is initiated earlier than ultimate stress [CVAR07] when the yield surface is activated.

Figure 2.14 depicts the results of a simulation of a cyclic compression test by using a plastic damage model. As can be seen, damage part contributes to induce a global softening of the behaviour while plasticity contributes to the generate permanent deformations. Therefore, it is shown that plastic damage model is appropriate to capture both degradation of elastic stiffness and also non reversible phenomena in the material. Nevertheless, the model from [JHPCG06] still dependent on the mesh size. In a more general context, regularization method should be included in the formulation to give a result that tends to be mesh independent.

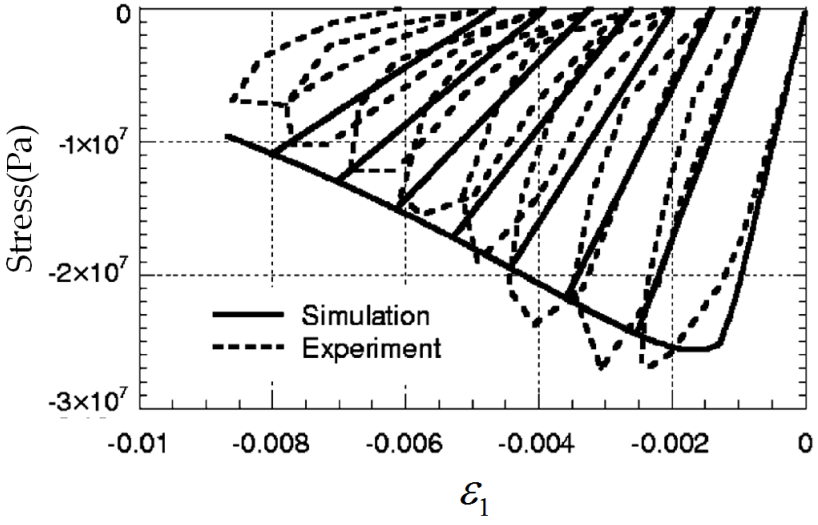

FIGURE 2.14: Simulation of the cyclic compression test by using plastic damage model [JHPCG06]

2.2 Regularization method

Simulations of the behaviour of materials with strain localization within continuum mechanics cannot describe properly both the thickness of localization and distance between them. They suffer from mesh sensitivity (its size and alignment) and produce unreliable results. The strains concentrate in one wide element and the

computed force-displacement curves are mesh dependent (especially in the post-peak part). There are two possible approaches to solve this problem including a partial regularization or a full regularization.

2.2.1 Partial regularization

Partial regularization essentially means that the energy based adjustment of the stress-strain diagram depends on the size of the element in the model. In this regard, the model makes use of the softening law which depends on the characteristic length (l_c) of the fractured domain. This characteristic length of the fractured domain actually partially contributes to regularize the model.

The characteristic length of the element can be computed from the dimensions of the element. In two-dimensional analysis, for instance, the characteristic length l_c of the element can be defined as the diameter of the circle that contains the area of the element A_c as:

$$l_c = \sqrt{\frac{4A_c}{\pi}} \tag{2.32}$$

Namikawa et al. [NM07] used partial regularization by inserting the characteristic length in the tensile softening part of the elasto-plastic model. The tensile criterion is defined as:

$$\sigma_3 = -(1-\omega)T_f \tag{2.33}$$

where ω is the internal variable for softening defined in such a way

$$\begin{aligned} \text{if } 0 \le \omega \le 0.75 \quad &\text{then} \quad \omega = l_c \frac{T_f}{G_f}(\varepsilon_3^p - \varepsilon_{3\,\text{peak}}^p) \\ \text{if } 0.75 \le \omega \le 1.0 \quad &\text{then} \quad \omega = \frac{12}{17} - \frac{1}{17} l_c \frac{T_f}{G_f}(\varepsilon_3^p - \varepsilon_{3\,\text{peak}}^p) \end{aligned} \tag{2.34}$$

where T_f is tensile strength of material, G_f is tensile fracture energy, ε_3^p is current minor principal stress, and $\varepsilon_{3\,\text{peak}}^p$ is minor principal stress at peak.

By using partial regularization, a correct energy dissipation in a localized damage band might be obtained, but the width of the numerically resolved fracture process zone depends on the element size and tends to zero as the mesh is refined. Thus, this approach cannot be considered as a true localization limiter [Sar15]. It only provides a partial regularization of the problem in the sense that the global

response characteristics do not exhibit spurious mesh sensitivity, but the mesh-induced directional bias is still present. Nevertheless, this method is quite popular because of less effort in the computation technique.

2.2.2 Full regularization

Full regularization is achieved by a proper generalization of the underlying continuum theory. One popular approach consists in using an integral type non-local approach where it is assumed that the stress at a certain point does not only depends on the state variables at that point, but also on the distribution of the state variables over the whole body, or over a finite neighbourhood of the point under consideration.

For example, the equivalent strain $\tilde{\varepsilon_{eq}}$ in Mazars model is transformed into a non-local measurement by using a weighted spatial average

$$\tilde{\varepsilon_{eq}} = \int_V \alpha(x,\xi)\varepsilon_{eq}(\xi)d\xi \tag{2.35}$$

where $\alpha(x,\xi)$ is the non-local weighting function. It holds the meaning of an influence function which is calculated based on the distance $D = \|x - \xi\|$, where x is the receiver point and ξ is the source point. The closer the distance of D, the bigger the influence value is. Figure 2.15 shows an example of the influence radius of an element on its neighbourhood.

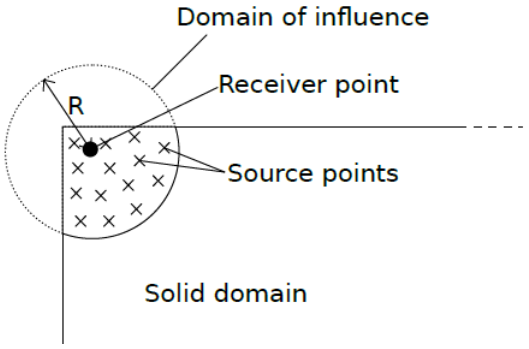

FIGURE 2.15: Influence zone in the averaging process [Sar15]

This method needs huge effort in the computation technique since it requires to find all the Gauss points ξ whose distance from x is smaller than R.

2.3 Conclusion

Within the framework of a continuum approach of the behaviour of quasi brittle materials, there are three families of constitutive modeling that can be used for rammed earth. First, we can find an elastic damage approach, secondly an elastic-plastic model, and finally a mixed damage and plasticity model.

It is shown that plastic damage model can better capture the behaviour of the quasi brittle material. But, it involves large amount of the parameters which is sometimes not available or difficult to obtain. To bridge the number of available experiments to identify the model parameters and the complexity of the model, a hierarchical approach is proposed in this work. This approach can be used as a basis for the development of a new constitutive model for rammed earth. Obviously, one cannot expect to model sophisticated phenomena if few experimental tests are available and any user must keep in mind this aspect when solving a boundary value problem.

Chapter 3

New elasto-plastic model for rammed earth

3.1 Model CJS-RE

CJS model is a constitutive model based on the elasto-plasticity theory. This model was initially created by three authors (Cambou, Jafari, and Sidoroff) and the primary relationships can be found in the PhD thesis of Jafari [CJE89]. This constitutive model which was developed several decades ago at Ecole Centrale de Lyon has initially been developed to model the behaviour of sandy soils. Different works have improved or extend the usage of this model to embrace more complex granular materials or loading conditions [Ela92, MDC00, Pur06, Bag11, DV15].

In this work, a new hierarchical constitutive model denoted CJS-RE (stands for CJS for Rammed Earth) was developed on the basis of CJS model for the modeling of the behavior of rammed earth. The failure surface of CJS-RE model in the three dimensional principal stress space can be seen in Figure 3.1. It holds a conical shape with a non-circular base section. This shape is typical of granular material or quasi brittle material (eg concrete) where there exists a dissymetry of behavior along a compression stress path and an extension stress path. Moreover, there is a linear dependency of the maximum shearing resistance on the mean pressure. For the sake of simplicity, there is no cap closing the failure surface in this model. It is justified by the range of typical stresses in rammed earth houses which is low (ie: around 0.3 MPa for two storey house [NBP+16]), which implies that failure cannot result from an excessive mean pressure.

Basically, CJS-RE model consists of an elastic mechanism of deformation and two plastic mechanisms of deformation. The plastic mechanisms cover two possible

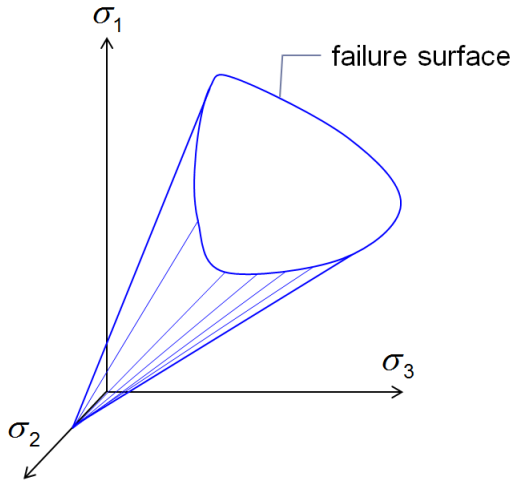

FIGURE 3.1: CJS-RE failure surface in the principal stress spaces

modes for the creation of irreversible strains: shearing and tension. Thus, the increment of deformation writes:

$$\dot{\varepsilon}^{total} = \dot{\varepsilon}^{e} + \dot{\varepsilon}^{sp} + \dot{\varepsilon}^{tp} \tag{3.1}$$

where $\dot{\varepsilon}^{total}$ is the increment of deformation, $\dot{\varepsilon}^{e}$ is the increment of elastic deformation, $\dot{\varepsilon}^{sp}$ is the increment of plastic deformation due to shearing and $\dot{\varepsilon}^{tp}$ is the increment of plastic deformation due to tension.

CJS-RE model is designed in a hierarchical way from a simple and basic version to more complex one according to the available experiment data for the identification of the model parameters and the sophistication of the phenomena that are to be modeled. In this work, two levels (degrees of complexity) of the model are designed to model the behavior of rammed earth. For the sake of simplicity, all of the main constitutive equations will be presented first before addressing the different hierarchies of the model.

3.2 Elastic mechanism

The elastic deformations are computed according to Hooke's law:

$$\dot{\boldsymbol{\varepsilon}}^{e} = \frac{\dot{S}}{2G^{e}} + \frac{\dot{I}_1}{9K^{e}}\boldsymbol{I}_d \tag{3.2}$$

with $\boldsymbol{S}$ the deviatoric stress tensor, $\boldsymbol{I}_1$ the first invariant of the stress tensor, and $\boldsymbol{I}_d$ the identity tensor. Herein, the elastic properties (G^e and K^e) are taken as

constants which lead to a linear elasticity. The alternative form of Equation (3.2) can be written as

$$\dot{\boldsymbol{\varepsilon}}^e = \left(\frac{1+\nu}{E}\right)\boldsymbol{\sigma} - \left(\frac{\nu}{E}\right) tr(\boldsymbol{\sigma})\boldsymbol{I}_d \tag{3.3}$$

with E the Young modulus and ν the Poisson ratio.

3.3 Plastic mechanisms

In this model, plasticity is generated by two different modes including shearing and tension. The relationships for these two plastic mechanisms are described briefly in the following subsection.

3.3.1 Shear yield surface

The shear yield surface limits the elastic domain and can isotropically and/or kinematically expands depending of the kind of considered hardening. It can also soften after the maximum shearing resistance is reached. For the sake of simplicity, the shape of the shear yield surface is similar to that of the shear failure surface (Figure 3.2). Figure 3.2a depicts the typical section of the model in the meridian plane and Figure 3.2b depicts that in the deviatoric plane. In Figure 3.2, the initial state of stress is supposed to be isotropic which implies that the shear yield surface is centered on the hydrostatic axis. R_{ini} is the initial yield radius, R_{mvc} is the maximum volumetric contraction radius (see below for the physical meaning) and R_{fail} is the radius of the shear failure surface. Note that, in the level-1 model (CJS-RE1), for the sake of simplicity, R_{ini} and R_{mvc} are supposed to be equal to R_{fail}.

3.3.1.1 Plastic criterion

The yield function of the shear or deviatoric mechanism writes:

$$f^s(\boldsymbol{\sigma}, R_{\text{fail}}) = q_{II} h(\theta_q) - R_{\text{fail}}(I_1 + 3T_{\text{r max}}) \leq 0 \tag{3.4}$$

where q_{II} is the second invariant of the local deviatoric stress tensor written as

$$q_{II} = \sqrt{\boldsymbol{q}.\boldsymbol{q}} \qquad \text{with} \qquad \boldsymbol{q} = \boldsymbol{s} - I_1 \boldsymbol{X} \tag{3.5}$$

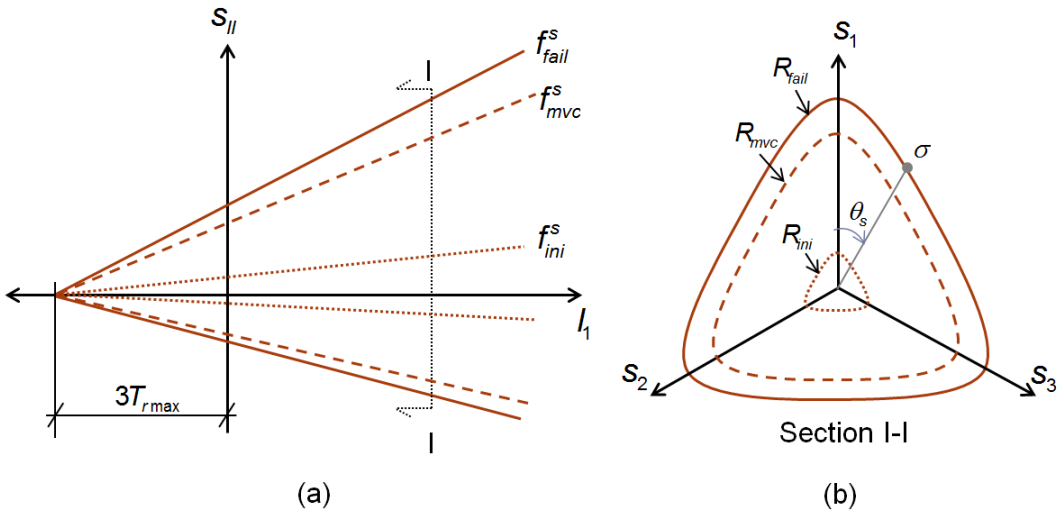

FIGURE 3.2: Shear yield/failure surface in CJS-RE model; (a): in the meridian plane (θ_s =const) and (b): in the deviatoric plane (I_1 =const). In the case of CJS-RE1, the surface of the maximum volumetric contraction state coincides with the failure surface.

In Equation (3.5)

$$\boldsymbol{s} = \boldsymbol{\sigma} - \frac{tr(\boldsymbol{\sigma})}{3}\boldsymbol{I}_d \tag{3.6}$$

where $\boldsymbol{s}$ is the deviatoric stress tensor, R_{fail} is the average radius of the shear failure surface, $h(\theta_q)$ is the shape factor of the yield surface, I_1 the first invariant of the stress tensor, $\boldsymbol{X}$ is a tensor which defines the center of yield surface, and $T_{\text{r max}}$ is a model parameter corresponding to the apex of the yield surface.

In Equation (3.4), the shape factor $h(\theta_q)$ is defined as a function of Lode angle as follows:

$$h(\theta_q) = (1 - \gamma\cos(3\theta_q))^{1/6} \tag{3.7}$$

where θ_q is the Lode angle in the deviatoric plane such that when 0^o, the stress path corresponds to a compression stress path and 60^o to an extension stress path. The reference direction of the Lode angle can be seen in Figure 3.2b. γ is model parameter which quantifies the dissymmetry of the failure surface. It is supposed to take into account the different behaviour along the compression and extension stress path as found in the experiments of quasi brittle materials (Figure 1.14). Figure 3.3 depict the influence of γ on the shape of the shear yield/failure. If γ is equal to zero, the failure surface (and the yield surface) is a circular cone equivalent to Drucker-Prager model. There is some limits in the use of such relationship for the shape factor since it is not warranty the convexity for any value of γ. The yield surface is still convex if γ is smaller than 0.85 (Figure 3.3). Other shape functions that do not hold such limitation can be found in [BP04].

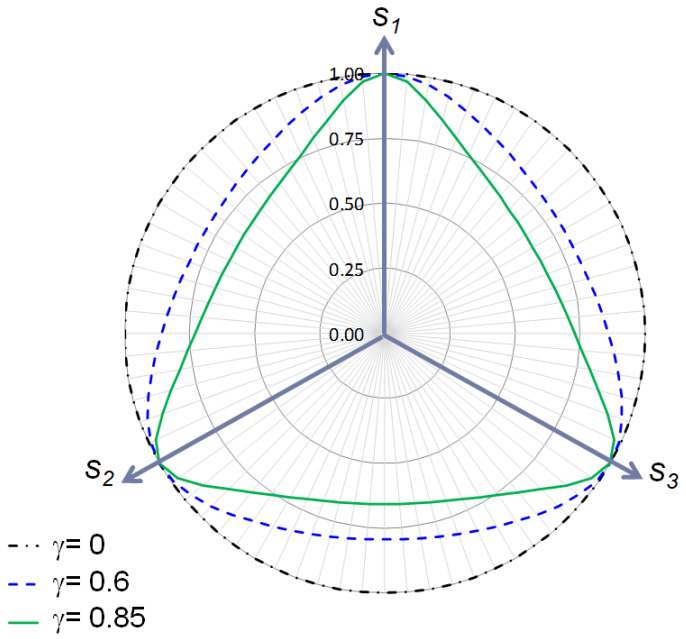

FIGURE 3.3: Influence of γ on the shape of the shear yield/failure surface

3.3.1.2 Flow rule

The flow rule of the plastic shear mechanism is non-associated and the direction of the plastic deformation induced by this mechanism is derived from a potential surface g^s. The flow rule is defined by the following relationship:

$$\dot{\boldsymbol{\varepsilon}}^{sp} = \dot{\lambda}_s \boldsymbol{G}^s = \dot{\lambda}_s \frac{\partial g^s}{\partial \boldsymbol{\sigma}} \tag{3.8}$$

with λ_s the plastic multiplier for the shear plastic mechanism. Instead of defining the potential surface, the direction $\boldsymbol{G}$ of the increment of plastic deformation is directly computed. To allow phases of contractancy and dilatancy to be generated when shearing, $\boldsymbol{G}$ is computed in order to satisfy the following dilatancy law:

$$\dot{\varepsilon}_v^{sp} = \beta \left(\frac{s_{II}}{s_{II}^{\text{mvc}}} - 1 \right) \frac{|\boldsymbol{s} : \dot{\boldsymbol{e}}^{sp}|}{s_{II}} \tag{3.9}$$

where β is a parameter that controls the dilatancy rate. s_{II}^{mvc} is the second deviatoric stress at the Maximum Volumetric Contraction (MVC) state. The Maximum Volumetric Contraction surface is an isotropic surface defined as:

$$f^{\text{mvc}} = s_{II}^{\text{mvc}} h(\theta_q) - R_{\text{mvc}}(I_1 + 3T_{\text{r max}}) \tag{3.10}$$

For the sake of simplicity, the shape of the MVC surface is similar to that of the shear failure surface and its size is controlled by the radius R_{mvc} which is a model parameter. Volumetric deformations are associated to contraction when $s_{II} < s_{II}^{\text{mvc}}$ otherwise to dilation. In Equation 3.9, β is a model parameter that ensures that positive volumetric deformations take place for contraction, according to the chosen convention. In fact, tensor $\boldsymbol{G}^s$ is defined in such a way the increment of plastic deviatoric deformation is orthogonal to the tangent vector $\boldsymbol{n}$ of the potential plastic surface . In other words, the following kinematic condition must be satisfied:

$$\dot{\boldsymbol{\varepsilon}}^{sp}\boldsymbol{n} = 0 \tag{3.11}$$

The expression of $\boldsymbol{n}$ can be described as follows:

$$\boldsymbol{n} = \frac{\beta' \frac{\boldsymbol{s}}{s_{II}} - \boldsymbol{I}_d}{\sqrt{\beta'^2 + 3}} \qquad \text{with} \qquad \beta' = \beta\left(\frac{s_{II}}{s_{II}^{mvc}} - 1\right) sign(\boldsymbol{s} : \dot{\boldsymbol{e}^{sp}}) \tag{3.12}$$

Tensor $\boldsymbol{G}$ can be therefore expressed as a function of the yield surface f^s.

$$\boldsymbol{G} = \frac{\partial f^s}{\partial \boldsymbol{\sigma}} - \left(\frac{\partial f^s}{\partial \boldsymbol{\sigma}}.\boldsymbol{n}\right)\boldsymbol{n} \tag{3.13}$$

3.3.1.3 Hardening

The size of the yield surface can initially be set to limit the domain of reversible deformations and can isotropically expand depending on the chosen degree of sophistication (level) of the model. Herein, for monotonous loading modelling, the hardening is isotropic and allows the yield surface radius R to increase according to:

$$\dot{R} = A(R_{\text{fail}} - R_{\text{ini}})\exp(-Ap)\dot{p} \tag{3.14}$$

where $\dot{p}$ is the increment of the hardening variable and A is a model parameter which controls the velocity of the isotropic hardening. R_{ini} and R_{fail} represent the initial value of yield radius and the maximal size of the yield surface. $\dot{p}$ is given by the normality relationship:

$$\dot{p} = -\dot{\lambda}_s \frac{\partial f^s}{\partial R} = \dot{\lambda}_s (I_1 + 3T_{\text{r max}}) \tag{3.15}$$

Equation (3.14) can be integrated which allows to directly determine the yield radius by:

$$R = R_{\text{fail}} - (R_{\text{fail}} - R_{\text{ini}})\exp(-Ap) \tag{3.16}$$

Therefore, at the beginning when the system is at elastic state ($p = 0$), R is equal to R_{ini} and when $p \to \infty$ R tends to R_{fail}. The evolution of the loading radius according to the proposed hardening function is depicted in Figure 3.4.

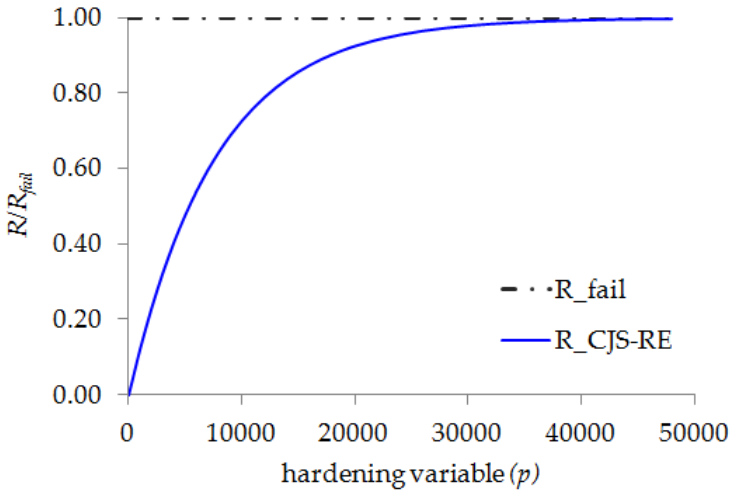

FIGURE 3.4: Evolution of the loading radius R in the CJS-RE model

3.3.1.4 Shear softening

In a quasi brittle materials like rammed earth, softening of the mechanical behaviour can occur from the development of cracks and decohesion of grains. In this study, shear softening is modelled by decreasing the maximum tensile resistance $T_{\text{r max}}$ associated to both the shear yield surface and the shear failure surface. Thus, $T_{\text{r max}}$ will degrade exponentially from $T^{\text{ini}}_{\text{r max}}$ to the residual value $T^{\text{res}}_{\text{r max}}$ (Figure 3.5). The shear softening law writes:

$$T_{\text{r max}} = (T^{\text{ini}}_{\text{r max}} - T^{\text{res}}_{\text{r max}}).\exp(\alpha_s \varepsilon^{sp}_{\text{diff}}) + T^{\text{res}}_{\text{r max}} \tag{3.17}$$

$$\varepsilon^{sp}_{\text{diff}} = \|\boldsymbol{\varepsilon}^{sp} - \boldsymbol{\varepsilon}^{\text{p fail}}_{s}\| \tag{3.18}$$

with $T^{\text{ini}}_{\text{r max}}$ is the initial value of $T_{\text{r max}}$ and $T^{\text{res}}_{\text{r max}}$ is the residual value of $T_{\text{r max}}$ which in our study is stated to be equal to 20% $T^{\text{ini}}_{\text{r max}}$. This residual level is also the one used by Namikawa et al. [NM07] in the modelling of quasi brittle materials. α_s is the shear softening parameter that controls the rate of shear softening and ε^{sp}_{diff} is the norm of the difference between the current deviatoric plastic strain $\boldsymbol{\varepsilon}^{sp}$

and the deviatoric plastic strain at peak $\boldsymbol{\varepsilon}_s^{\mathrm{p\,fail}}$. The latter tensor is first set to zero and then is equal to the tensor of plastic deformation when the stress path reaches any failure surface, either tensile failure surface or shear failure surface. It implies that if the tensile failure surface is first reached, the capacity of the material to resist to shearing decreases according to the model.

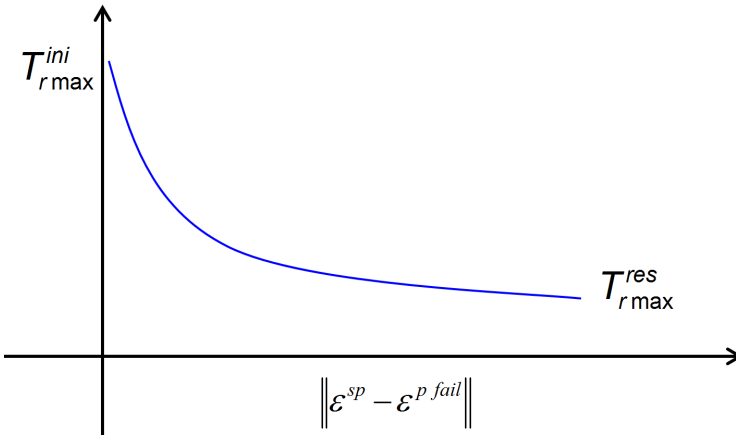

FIGURE 3.5: Shear softening function

3.3.2 Tensile yield surface

The tensile yield surface which is also a failure surface corresponds to another mechanism of plastic deformation which is different from that observed under a shear loading. The tensile yield surface is similar to the maximum tensile stress criterion of Rankine for brittle fracture in concrete [Che07]. It reduces the domain of acceptable stresses given by the shear failure surface (Figure 3.6). Figure 3.6a gives a typical section in the meridian plane while Figure 3.6b gives the tensile yield surface of the constitutive model in the deviatoric plane. The relationships for the tensile plastic mechanism, flow rule, and also the tensile softening rule are described in the following subsection.

3.3.2.1 Plastic criterion

The tensile yield surface is confounded with the tensile failure surface. This yield surface is able to soften when the tensile failure is triggered. This yield surface writes:

$$f^t(\sigma_3) = \sigma_3 - T_{\mathrm{r}} \leq 0 \tag{3.19}$$

with σ_3 is the minor principal stress and T_{r} is a model parameter which characterizes the tensile strength of the material. Therefore, once σ_3 reaches T_{r}, then

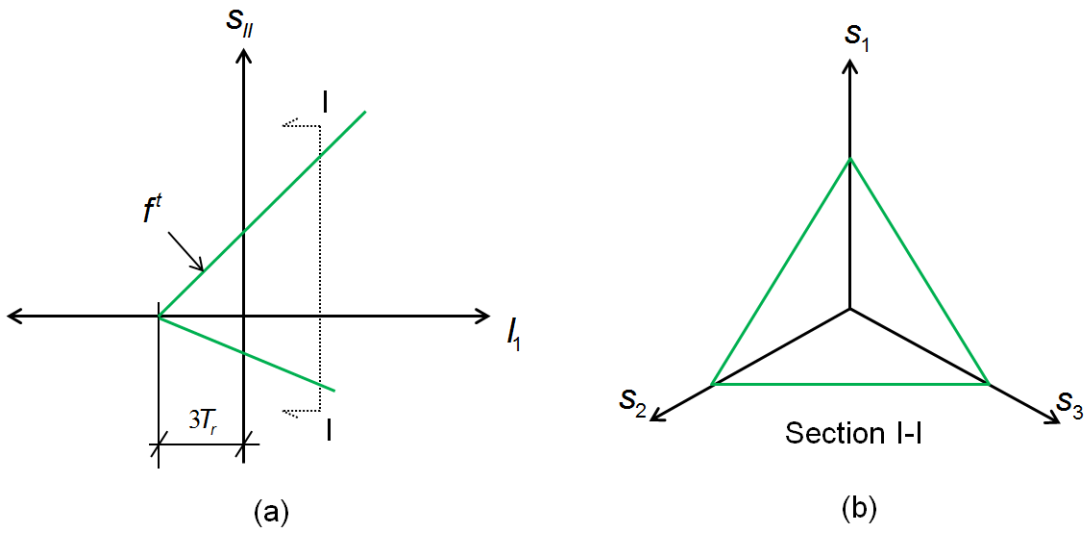

FIGURE 3.6: Tensile yield surface in CJS-RE model; (a): in the meridian plane and (b): in the deviatoric plane

tensile failure occurs. The determination of σ_3 in CJS-RE model can be seen in Appendix E.1.

3.3.2.2 Flow rule

Based on the experiments evidence in the quasi-brittle material, tensile failure zones tend to be perpendicular to the direction of the minor principal stress, indicating that the tensile plastic strain occurs in the same direction as the minor principal stress. It tends to justify that the plastic flow rule for this mechanism is associated.

$$\dot{\boldsymbol{\varepsilon}}^{tp} = \dot{\lambda}_t \boldsymbol{G}^t = \dot{\lambda}_t \frac{\partial g^t}{\partial \sigma_3} \tag{3.20}$$

where λ_t is the plastic multiplier for the tensile mechanism and $\boldsymbol{G}^t$ is a tensor defining the direction of the plastic deformations.

3.3.2.3 Tensile softening

After the tensile stress reaches its maximum resistance, then tensile softening occurs. Tensile softening is modelled as a degradation of tensile strength (T_r) by using exponential function as:

$$T_r = T_r^{\text{ini}} \exp(\alpha_t \int \dot{\varepsilon}^{tp} dt) \tag{3.21}$$

with T_r^{ini} is the initial value of T_r and α_t is a tensile softening parameter that will be set to a default value for different levels of model.

3.4 Different hierarchies for the constitutive model

CJS-RE model is designed in a hierarchical way which depends on the complexity of the phenomena that need to be modeled together with the amount of information available to identify the model parameters. In this work, two levels of the model are created with general features given in Table 3.1. They concern modelling involving monotonous loadings and not cyclic loadings.

3.4.1 CJS-RE1

The level-1 (CJS-RE1 model) is the basic level for the model. It holds the basic features of an elasto-plastic model such as Mohr-Coulomb model adapted to take into account the specificities of quasi brittle materials. The advantage of CJS-RE1 is that the shear failure surface is continuously derivable contrary to Mohr-Coulomb model. Plasticity is generated when the current state of stress reaches the yield surfaces that are also failure surfaces. The shape of the failure surface in CJS-RE1 is depicted in Figure 3.7. The inner envelop of these two surfaces (solid lines) splits the stress space into an inner space where the state of stress is acceptable for the material from an outer space that is not physically reachable for it.

Table 3.1: Features in each level of the CJS-RE model

Model	Elasticity	Plasticity		
		Shear		Tensile
		Hardening	Softening	Softening
CJS-RE1	Linear	No (perfectly plastic)	No	Yes (stated)
CJS-RE2	Linear	Yes (isotropic hardening)	Yes*	Yes (identified)

*Note: Shear softening is triggered either by shear failure or tensile failure

The typical responses of CJS-RE1 throughout a compression stress path can be seen in Figure 3.8 where the yield shear surface is activated. Figure 3.8a shows

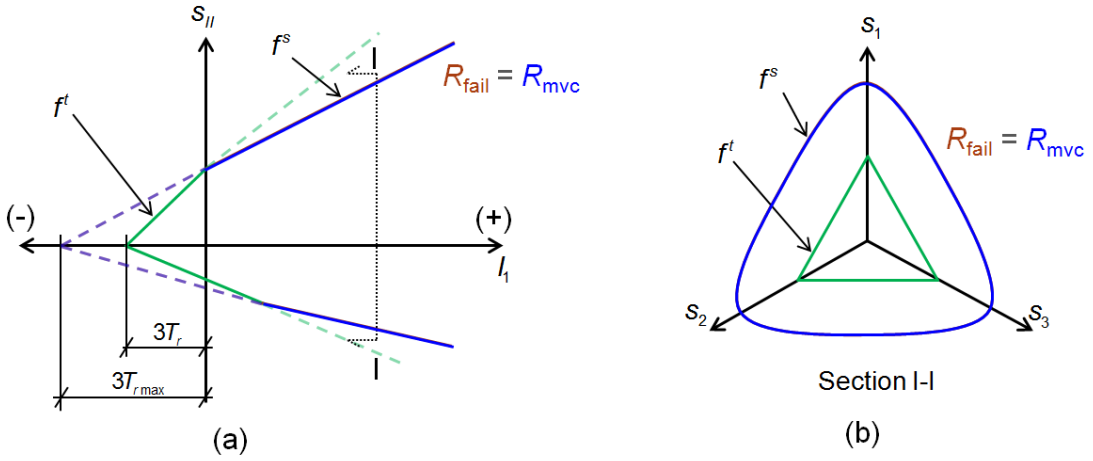

FIGURE 3.7: Failure surfaces of CJS-RE1; (a): in the meridian plane (θ_q =const) and (b): in the deviatoric plane (I_1 =const). I_1 is the first invariant of the stress tensor, s_{II} is the second invariant of the deviatoric stress tensor, s_1, s_2 and s_3 are the principal stresses of the deviatoric stress tensor.

the stress-strain curve and Figure 3.8b shows the corresponding volumetric deformation curve. In the first level of the model, the volumetric deformations are depicted by a bilinear curve associated to successive phases of contractancy and dilatancy. Dilatancy is generated when the shear yield surface is reached and its rate is controlled by the parameter β.

In CJS-RE1 model, the tensile behaviour is elastic until the tensile failure surface is reached. When the tensile strength of the material is reached, the tensile failure surface softens sharply (Figure 3.9). A default value for α_t which is equal to -1.0 is given and no identification is allowed. Therefore, for the use of the first level of the model, eight parameters with seven to identify:

- 2 elastic parameters : E and ν
- 6 plastic parameters : γ, R_{fail}, T_r, $T_{\text{r max}}$, β, and α_t

The process for the identification of the parameters is given in Appendix A where some model parameters can be identified through relationships with Mohr-Coulomb model and others which hold less significance in the stress strain response can be stated.

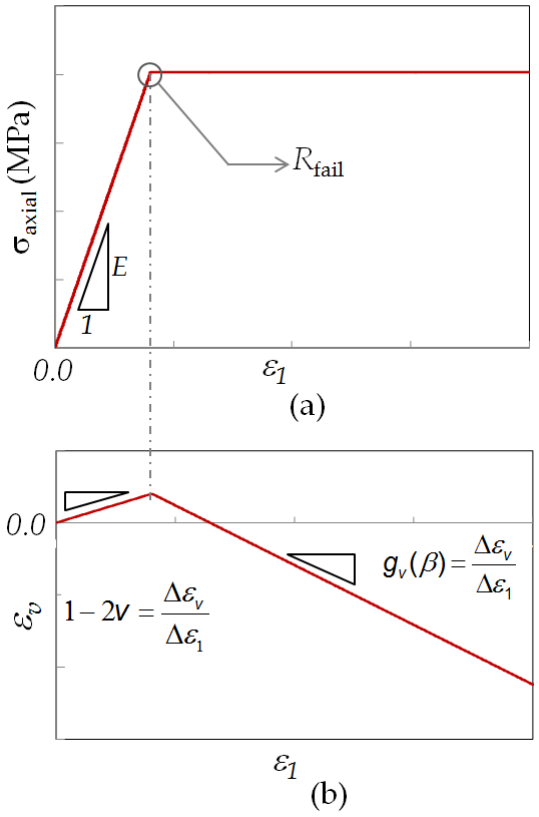

FIGURE 3.8: Simulation of a compression stress path with CJS-RE1 model; (a): stress-strain response and (b): volumetric deformation.

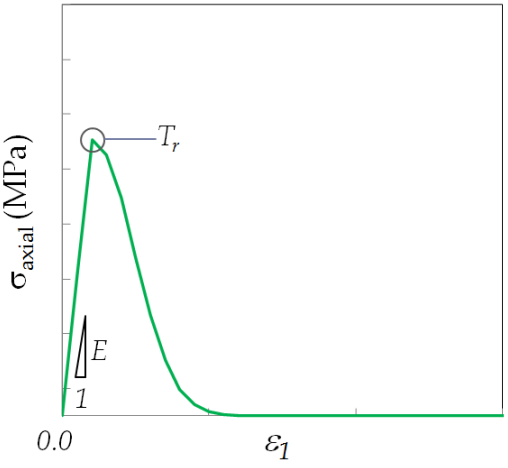

FIGURE 3.9: Uniaxial tensile test responses with CJS-RE1 model

3.4.2 CJS-RE2

The second level of the model is an elasto-plastic model having the same features as CJS-RE1 but a refinement is introduced with the use of a shear yield surface different from the shear failure surface. It allows the domain of elasticity to be far smaller than that of CJS-RE1 (Figure 3.10). An isotropic hardening of the deviatoric yield surface is added which is suitable when just monotonous loadings are to be simulated. Beside hardening, CJS-RE2 model can also exhibit a shear softening and a controlled tensile softening which was not the case of CJS-RE1.

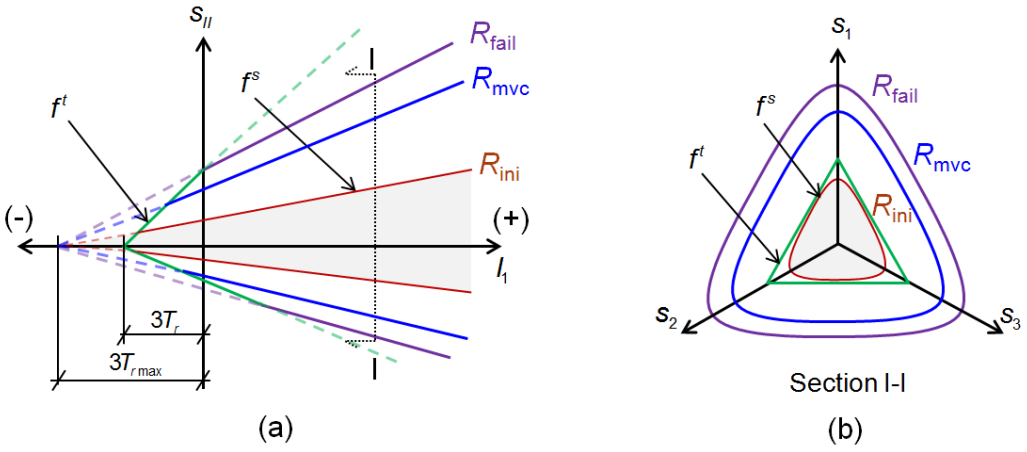

FIGURE 3.10: Failure surfaces of CJS-RE2; (a): in the meridian plane (θ_q =const) and (b): in the deviatoric plane (I_1 =const). I_1 is the first invariant of the stress tensor, s_{II} is the second invariant of the deviatoric stress tensor, s_1, s_2 and s_3 are the principal stresses of the deviatoric stress tensor.

The typical response of CJS-RE2 throughout a compression stress path can be seen in Figure 3.11. Figure 3.11a shows the stress-strain curve and Figure 3.11b shows the corresponding volumetric deformation curve. In this level of model, the maximum volumetric contraction state that separates contractive plastic volumetric deformations from dilative plastic volumetric deformations can be different from the shear failure state (Figure 3.11b). The tensile behaviour in CJS-RE2 is characterized by a softening which may be more gradual than in the first level of the model (Figure 3.12).

The use of CJS-RE2 requires twelve model parameters to identify:

- 2 elastic parameters : E and ν
- 10 plastic parameters : γ, R_{fail}, $T^{\text{ini}}_{\text{r max}}$, $T^{\text{res}}_{\text{r max}}$, T^{ini}_{r}, β, R_{ini}, A, α_s and α_t

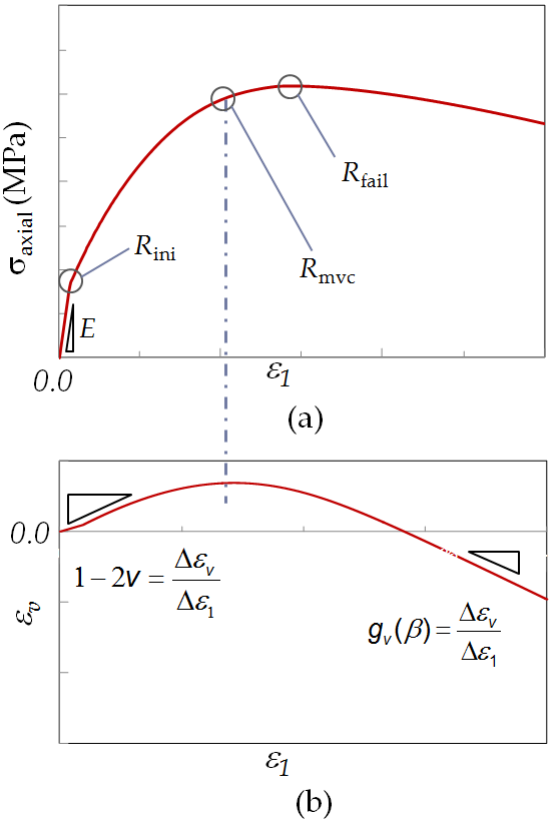

FIGURE 3.11: Simulation of a compression stress path with CJS-RE2 model; (a): stress-strain response and b: volumetric deformation.

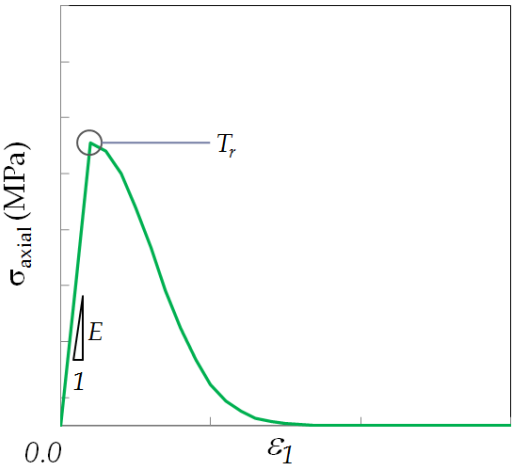

FIGURE 3.12: Uniaxial tensile test responses with CJS-RE2 model

The process for the identification of the parameters is given in Appendix A where some model parameters can be identified through relationships with Mohr-Coulomb model and others which hold less significance in the stress strain response can be stated.

Chapter 4

Validation tests

4.1 Reference tests

The validation of the hierarchical model CJS-RE is based on two sets of experiment references, one from Silva et al. [SOS+14], the second one from El Nabouch [EN17]. For the sake of simplicity, the first material will be denoted MAT-1 and the second one MAT-2.

4.1.1 MAT-1

The soil that was used for creating samples was not supposed to be suitable to be used for rammed earth structure due to an excessive clay content. Furthermore, the Particle Size Distribution (PSD) did not conform with the recommendations from [HGH94]. A correction of particle size distribution was carried out by adding some river sand and gravel into the original soil. The consistency limits and compaction properties before and after correction can be seen in Table 4.1. After correction, the plasticity index reduced almost by 50% and the dry density increased by about 20%. The corresponding particle size distribution is given in Figure **??** where the addition of sand and gravel was able to conform the material to the PSD recommended by [HGH94]. Six compression tests were performed on rammed earth samples made with this corrected material in order to investigate the repeatability of the tests (Figure 4.2).

The second test which will be used to validate CJS-RE model is a diagonal compression test which is a non homogenous test. More precisely, eleven wallets sized 550x550x200mm^3 were produced and tested under displacement control conditions

TABLE 4.1: Consistency limits and compaction properties of soils for rammed earth ([SOS+14])

Soil	LL (%)	PL (%)	PI (%)	ρ_{dmax} (gr/cm^3)	OWC (%)	G_s
before correction	30	18	12	1.83	13.4	2.68
after correction	23	16	7	2.1	10.1	2.68

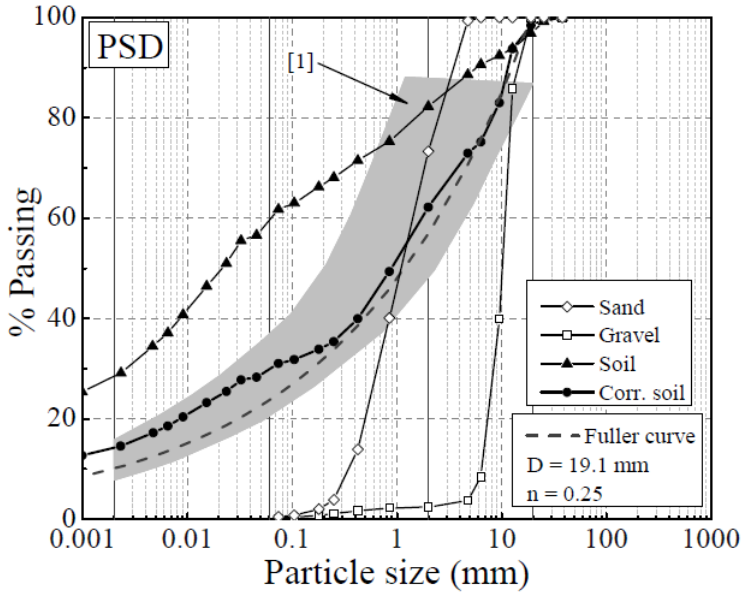

FIGURE 4.1: PSD of soil before and after correction [SOS+14]

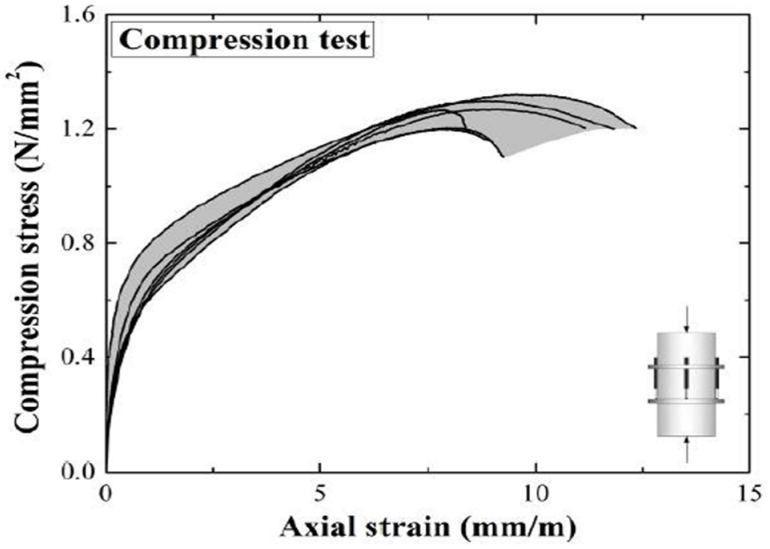

FIGURE 4.2: Compression tests results [SOS+14]

with a rate of 2 μm/s. The results are given in Figure 4.3a. It can be observed there are three possible types of behavior from the eleven tested samples. First, for some tests a first peak has been reached at small deformations (about 1mm/m) followed by a small softening; eventually, the shear resistance slightly re-increased with peak level similar to the first local peak. In the second case, for other tests there is no softening after the first peak and eventually, the shear resistance re-increased with a peak higher than the first local peak. In the third case, the first peak is followed by softening without re-increase of resistance. One must note that the upper and lower limits of the envelope of this set of tests are very different from 0.11MPa to 0.18MPa. This great departure implies that the repeatability of tests seems hard to achieve due to inherent heterogeneity of the wallet composed of different layers of compacted material. At the end of test, the crack pattern shows a vertical cracks along the wallet and also some cracks at the edge of the specimen (Figure 4.3b).

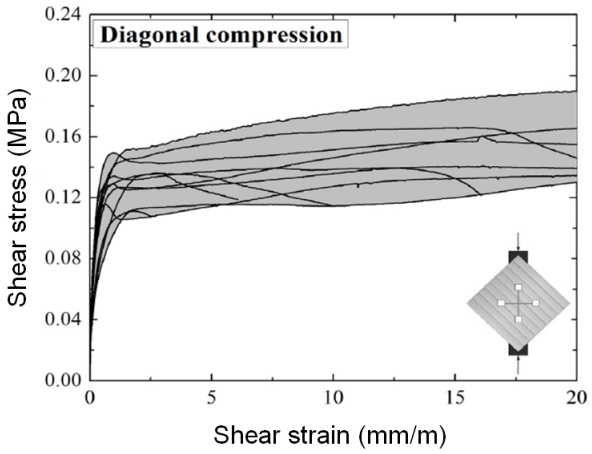

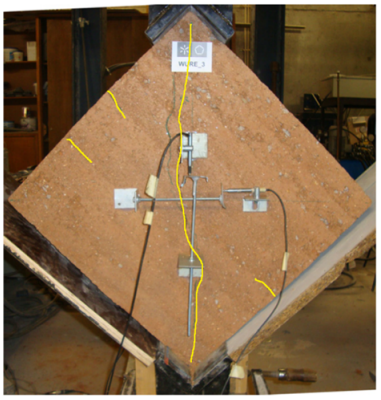

FIGURE 4.3: (a): Shear stress-shear strain curve of diagonal compression tests, (b): Crack pattern in the wall after the test [SOS+14]

4.1.2 MAT-2

MAT-2 material was used by El Nabouch to perform a series of pushover tests. Rammed earth materials were sourced from the demolition of an old farmhouse that was no longer in use. It is located in Dagneux, a village located in the Auvergne-Rhone-Alpes where many existing earth structures are found in this region. The PSD is depicted in Figure 4.4. From Figure 4.4, the soil consists mostly of fine particles (clay and silt). According to [EN17], the distribution of particles consists of sand (15%), silt (65%), and clay (20%).

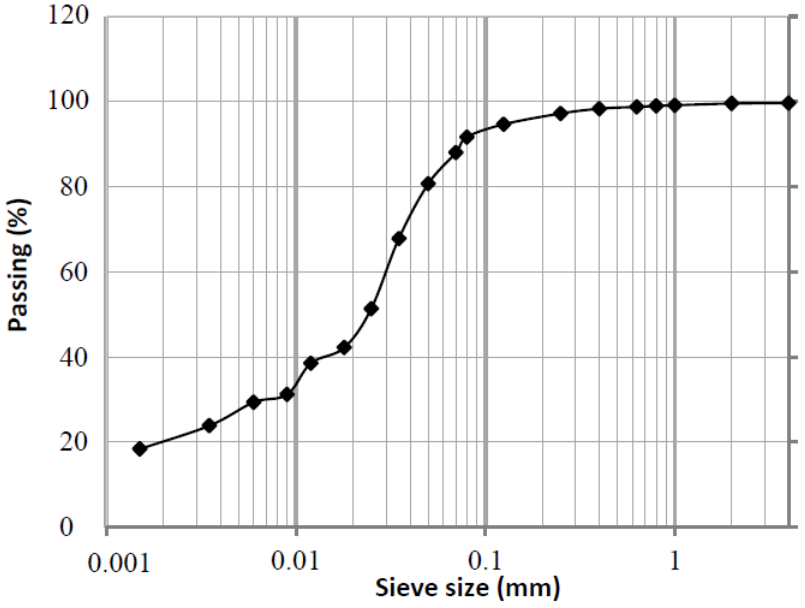

FIGURE 4.4: PSD of soil [EN17]

Three compression tests were performed using the soil. The results are presented in Table 4.2.

Then, a direct shear test was performed to identify some properties of the layers. A layer of material was extracted at mid-height wall and three different slices were identified: an upper slice, a mid-height slice and a bottom slice. The direct shear tests were performed to identified the properties of the upper slice and the mid-height slice. The resulting properties of MAT-2 are given in Table 4.3.

The third type of tests that was performed was a monotonous pushover tests on a wallets. In the pushover test, a wallet is pushed laterally until failure. A wallet measuring 1000x1500x250mm^3 (Wall-3) is used. A vertical pressure equal to 0.3MPa was used to represent the typical pressure of a two storey houses. The pushover tests results are depicted in Figure 4.5. In Figure 4.5a, the curve for

TABLE 4.2: Compression tests data [EN17]

Specimen	Dimensions of specimens (cm)	Dry density (gr/cm^3)	Water content (%)	f_c (MPa)	E (MPa)
Cylinder	d=20, h=40	1.878	3.4	2.0	760

Note: properties are averaged from three specimens

TABLE 4.3: Properties of MAT-2 from direct shear test data [EN17]

Type of test	Dimensions of specimens (cm)	ϕ_{us} (°)	ϕ_{ms} (°)	C_{us} (kPa)	C_{ms} (kPa)
Small shear box	10 x 10 x 4	44.1	45.6	263	135

us: upper slice of a layer, ms: mid-height slice of a layer

wall-3 reaches a peak for 40kN with a corresponding horizontal displacement of 9mm. The cracks pattern shows that shear failure at the bottom left and a quasi diagonal cracks can be observed (Figure 4.5b).

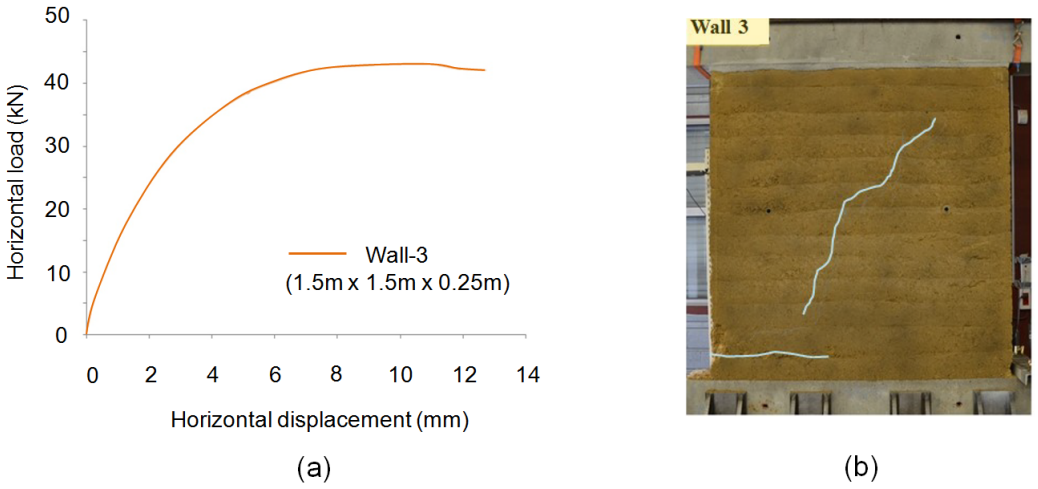

FIGURE 4.5: Pushover test results and crack patterns in the wall-3 [EN17]

4.2 Validation of CJS-RE1 model for MAT-1

The first validation of CJS-RE involves the first level of the model (CJS-RE1). First, some parameters are derived from compression tests on small samples (Figure 4.2). Due to the scarcity of available reference tests required to identify the whole set of model parameters (a compression and an extension test with a confining pressure different from zero, a tensile test), some relationships or usual equivalence with the Mohr-Coulomb model are used (Appendix B.1). Then, the proper validation of the model is carried out on the basis of a diagonal compression test which is a non homogeneous test and then very different from the test used to identify the model parameters. Finally, to investigate the lateral resistance of the wall, a simulation of a pushover test is carried out.

4.2.1 Identification of model parameters

The basic level for the model involves eight parameters (in fact, one of them holds a default value). A compression test allows the two elastic model parameters E and ν to be identified. They are defined as the initial tangential properties of the experimental stress-strain curves. The parameters related to the shear plastic mechanism (R_{fail}, $T_{\text{r max}}$, and γ) can be determined from two compression tests with different confining pressures and from a confined extension test. In the absence of a confined compression test and of the extension test, R_{fail}, γ and $T_{\text{r max}}$ can be estimated from Mohr-Coulomb model following the process shown in Appendix B.1. For the level-1 model, the maximum volumetric contraction state coincides with the failure state. It means that dilation takes place at the moment when shear failure is reached. Parameter β involved in the flow rule can be estimated from the volumetric deformation curve of the compression test. The initial slope of dilation after the maximum volumetric contraction state is just taken into account since after this short regime, dilation mainly results from opening cracks in a strong discontinuous medium.

The tensile strength property T_r can directly be obtained from a tensile test. If the tensile test is not available, the usual relationship between the maximum uniaxial compression resistance f_c and maximum uniaxial tensile resistance f_t of rammed earth can be used where f_t lies between 5% f_c and 12.5% f_c [AKS16]. In this study, it is stated that f_t or T_r is equal to 8% f_c which is an average trend.

From the reference of compression test mentioned in section 4.1.1, the set of model parameters for CJS-RE1 model was identified and is given in Table 4.4. One must

note that the relationships in Appendix B.1 were used to identify R_{fail}, γ, T_{rmax}, and β.

TABLE 4.4: Identified CJS-RE1 model parameters for MAT-1; experiments from [SOS+14]

Elastic		Plastic	
E	= 1036 MPa	β	= 3.0
ν	= 0.25 MPa	γ	= 0.84
		R_{fail}	= 0.22
		T_r	= 100.8 kPa
		T_{rmax}	= 730 kPa
		α_t	= -1.0 kPa

The result of the identification process is given in Figure 4.6. To achieve it, the model was implemented in FLAC-3D (code ITASCA) software and a compression test was simulated. As expected, the model fairly succeeded in retrieving the initial tangent of the stress strain curve and the peak of response, but the general stress path is excessively stiff. This feature is related to the linear elastic behavior that is imposed as long as the actual stress state has not reached the shear failure surface. A parametric study is proposed in Appendix C.1 to better reveal the characteristics of the model response under different triaxial stress paths.

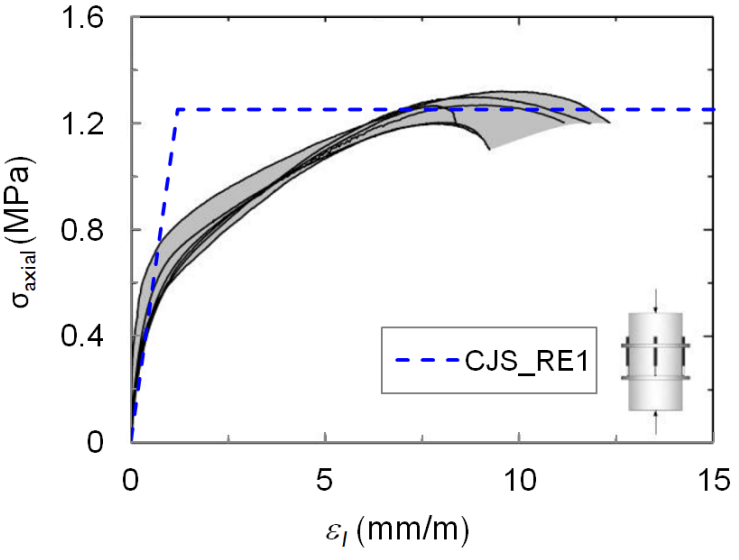

FIGURE 4.6: Results of the identification of CJS-RE1 parameters; simulation of a compression test; experiments from [SOS+14]

4.2.2 Validation: Diagonal compression test

A numerical simulation of a diagonal compression test was then performed. The material used for the construction of the wallets is the same as the one used for the compression tests. The geometry of the model together with the imposed boundary conditions are depicted in Figure 4.7. The quantities monitored in the simulation are those indicated by [AE02] where:

$$\tau = \frac{P}{h\sqrt{2}t} \tag{4.1}$$

τ is the shear stress acting on the net area of the specimen (MPa), P is the applied load (kN), h is the specimen height (mm), and t is the specimen thickness (mm). The shear distortion or shear strain can be calculated as follows:

$$\gamma_d = \frac{\Delta V + \Delta H}{g} \tag{4.2}$$

where γ_d is the shear strain, ΔV is the vertical shortening (mm), ΔH is the horizontal extension (mm) and g is gauge length (mm). The gauge length is taken to be equal to $h\sqrt{2}/3$ [SOS+14]. The loading is applied as a downward displacement acting on the upper part of the wallet with the velocity of 0.01μm/s.

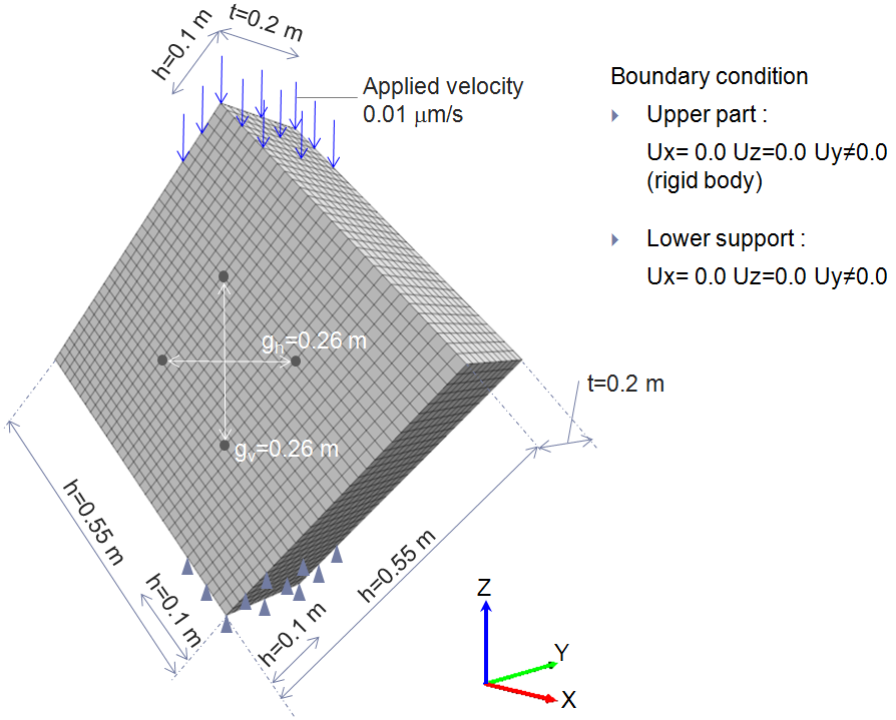

FIGURE 4.7: 3D numerical model for the diagonal compression of a wallet

The global stress-strain response is given in Figure 4.8. The simulation with CJS-RE1 model shows a local peak at about 0.16MPa before a small drop of the shear

resistance. This value is 20% higher compared with the average first peak of the experiments which is of 0.13MPa. Afterwards, it can be observed a re-increase of shear strength in the simulation which was not found in the experiments.

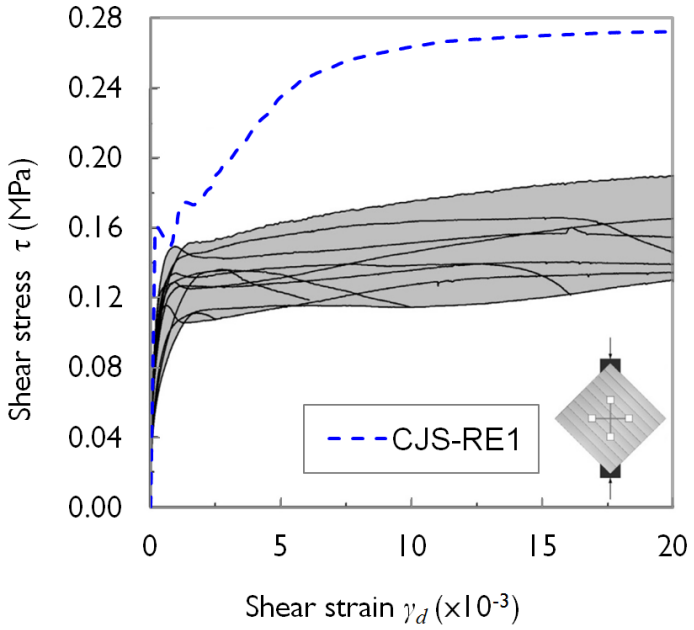

FIGURE 4.8: Stress-train response from a simulated diagonal compression test using CJS-RE1; experiments from [SOS+14]

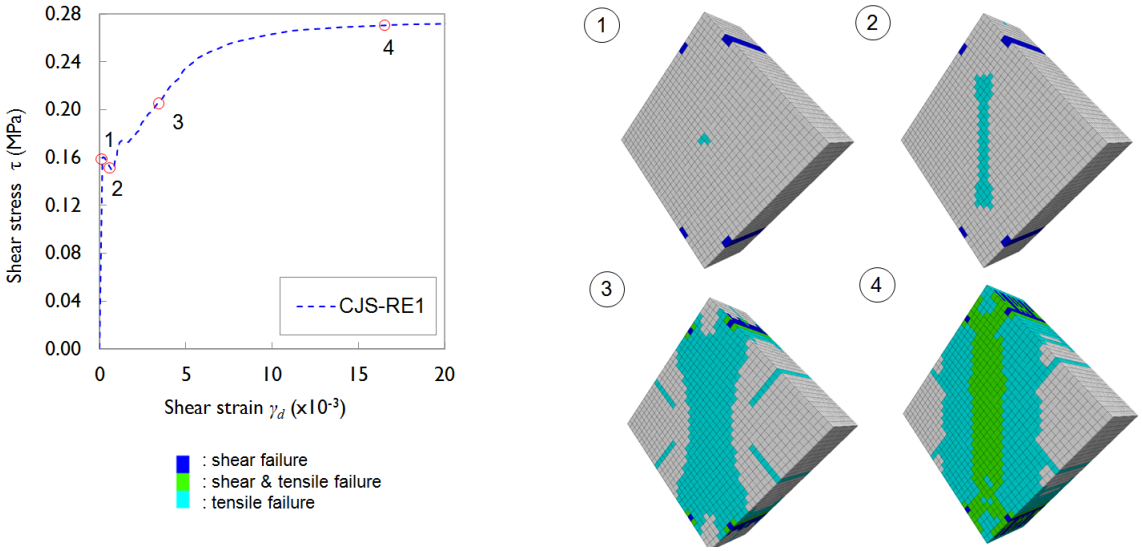

FIGURE 4.9: Evolution of the plasticity states in a simulated diagonal compression tests using CJS-RE1 at different computation stages.

Figure 4.9 shows the evolution of the plasticity states throughout the simulation of a diagonal compression test. At state 1 which corresponds to a transitory peak of resistance, a tensile failure emerges from the the center (on the outer surface)

of the wallet. At the top and bottom edge of the specimen, some elements of the meshing experience a shear failure. Between state 1 and state 2, when the drop of resistance is completed, the tensile failure has propagated upwards and downwards respecting the symmetry of the system crossing the whole wallet. While the extent of the pattern is important in the simulation, the phenomena are much more concentrated in the actual experiments (Figure 4.3b). This pattern is typical of the continuum approaches as can also be seen in [MOS+14] and [SOS+14]. The propagation of the tensile failure zones splits into two parts close to the top and bottom edges of the specimens in the direction of the previously mentioned zones at failure by shearing. Eventually, the tensile failure extents laterally and developed at the edges which can be observed at state 3. Between state 3 and state 4, the extent of the zones that reached the tensile failure is not significant indicating a rather stabilized process. At state 4, zone that already reached the tensile failure surface touched the shear failure surface. The evolution of the number of zones experiencing tensile failure shows that the behavior of the wallet throughout a diagonal compression tests is mainly monitored by the tensile failure criterion.

To get more insight onto the stress path of a typical element of the wallet, Figure 4.10 depicts the stress path of an element at the center but outer surface of the wallet. While Figures 4.10a-c-e-g give information throughout the simulation in the meridian plane, Figure 4.10b-d-f-h give other information in a given deviatoric plane indicated in the former figures.

Figures 4.10a-b give the stress path of the chosen element until reaching state 1. The stress path is elastic and this element reaches the tensile failure criterion at state 1. From state 1 to state 2 (Figures 4.10c-d), the tensile failure surface softens until T_r is equal to zero (state 2). The drop of resistance in Figure 4.8 is then related to the softening of the tensile failure surface of the elements at failure by tension. Finally from state 2 to state 3 (Figures 4.10e-f), the stress path follows the tensile failure surface while the mean pressure increases due to the processing compression of the wallet (consequently there is an increase of the overall resistance due to the increase of the actual mean pressure). In Figures 4.10g-h, one can see that at state 4, the chosen element reaches the shear failure surface. From now, the state of stress can only evolve at the junction of the two failure surfaces. The stabilisation of the response in Figure 4.9 can be explained by an existing continuous chains of zones crossing the wallet that reached the shear failure surface.

As a conclusion, even if the main features of a homogeneous compression test were retrieved by the elastoplastic model CJS-RE1, the validation of the model using a non homogeneous test shows its limitations. Even if the local peak of resistance

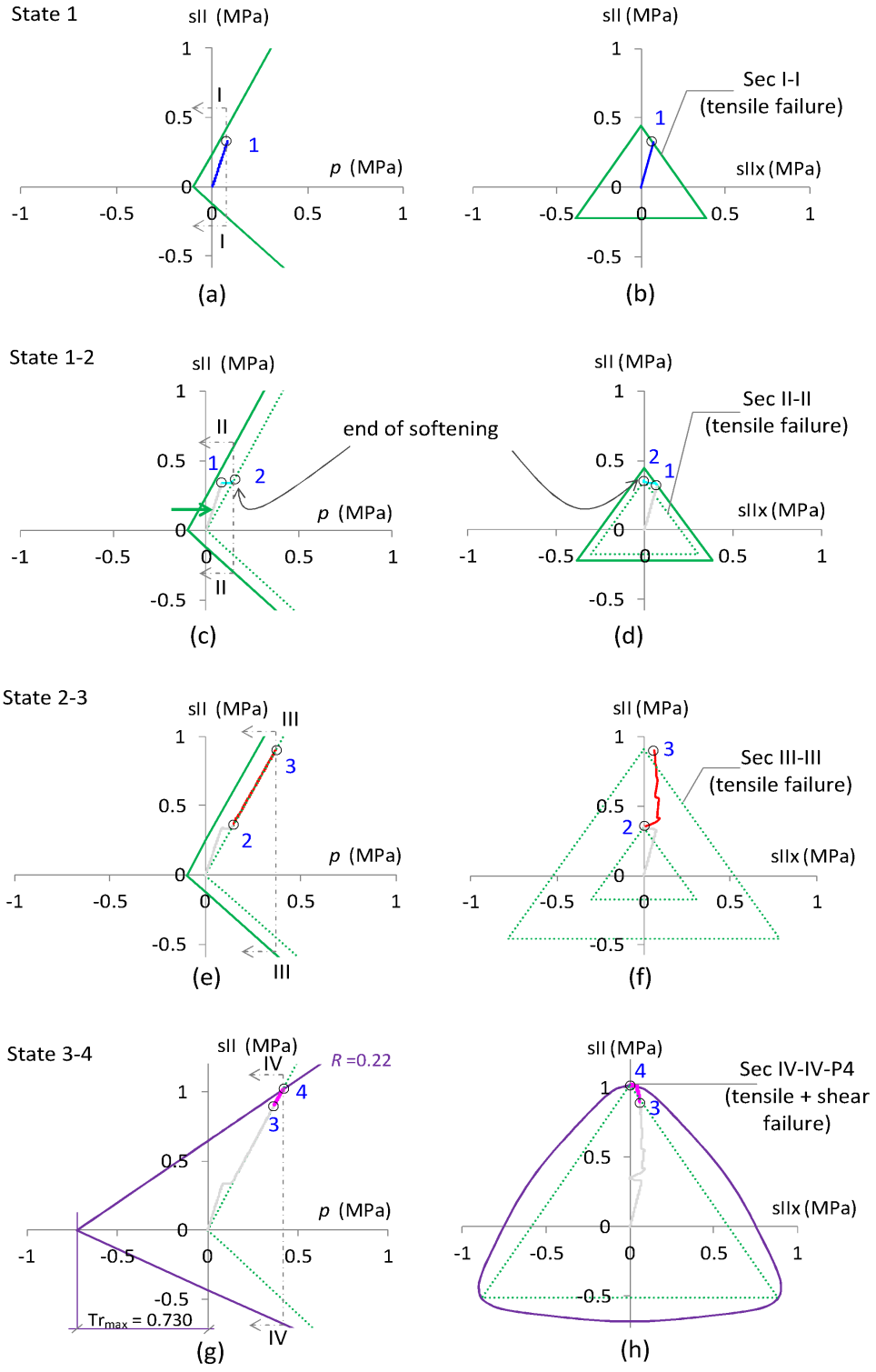

FIGURE 4.10: Stress path of an element in a simulated diagonal compression test (CJS-RE1).

was obtained with a correct value, the overall resistance at large deformation obtained throughout the diagonal compression test is highly overestimated. A higher order of CJS-RE is then required to better model phenomena at large deformations.

The result of the simulation may be mesh size dependent and even more when strong discontinuities of behavior are generated in a system when failure is reached. A mesh sensitivity study was then performed and is shown in Appendix D.1 but we showed that, considered the size of the mesh chosen herein a greater refinement does not modify excessively the general response.

4.2.3 Validation: Pushover test

To investigate the resistance of the wallet against lateral load, the simulation of a quasi-static pushover test is carried out. In this test, a wallet is pushed laterally until it reaches failure. The model parameters are taken from the one in the simulation of the diagonal compression test involving MAT-1. The three dimensional model of the pushover test is shown in Figure 4.11. The bottom part of the wallet is restrained in the three principal directions while in the upper part just the vertical direction is set free. Since, the lateral direction is restrained while vertical direction is free to move, thus the upper part of the wallet is able to rotate.

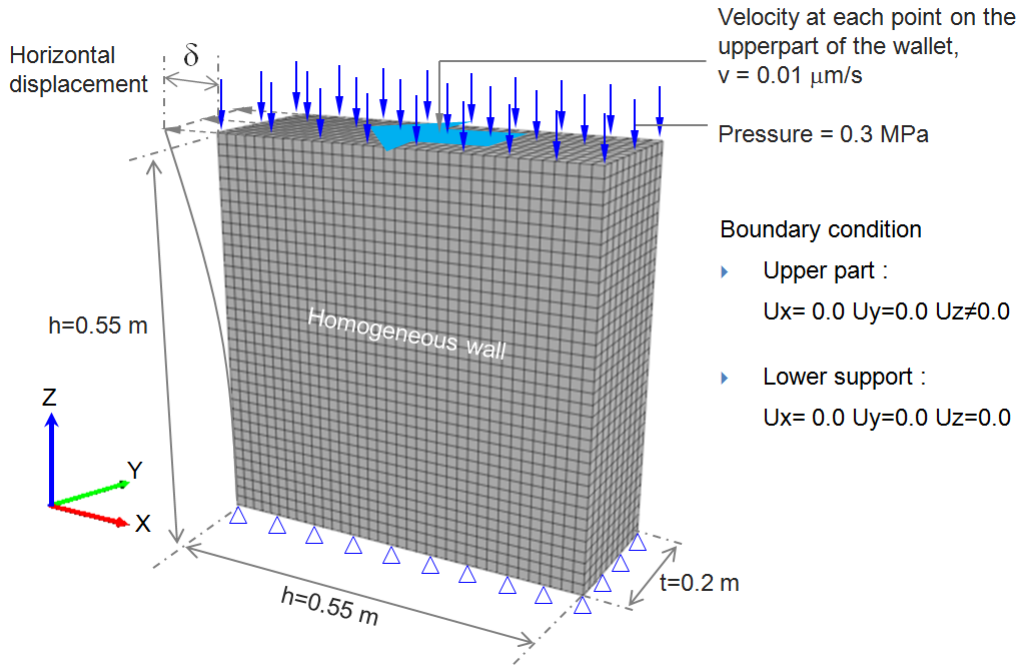

FIGURE 4.11: 3D-Model for the pushover test on a wallet

In this pushover test simulation, the wallet is first loaded by a vertical pressure of 0.3MPa on the upper part. This vertical pressure is supposed to model a normal stress acting on the wall in a typical 2-storeys rammed earth building. After the system reaches equilibrium, the lateral load is then applied on the upper part of the wallet with a velocity rate of 0.01 μm/s. In the experiments, a beam is usually used as a casket for the wall and will transfer the movement of the actuator to the wallet. Herein, the loading is directly applied to the top wallet nodes with a rigid body movement.

Throughout the simulation, the wallet resistance is obtained by cumulating the reaction forces at the top wallet nodes while the lateral displacement is measured on the upper left side of the wallet. Figure 4.12 shows the load displacement curve of the wallet where three different states are put out. The simulation with CJS-RE1 model shows a global resistance of 13kN for the wallet (MAT-1) associated to a displacement of about 1mm.

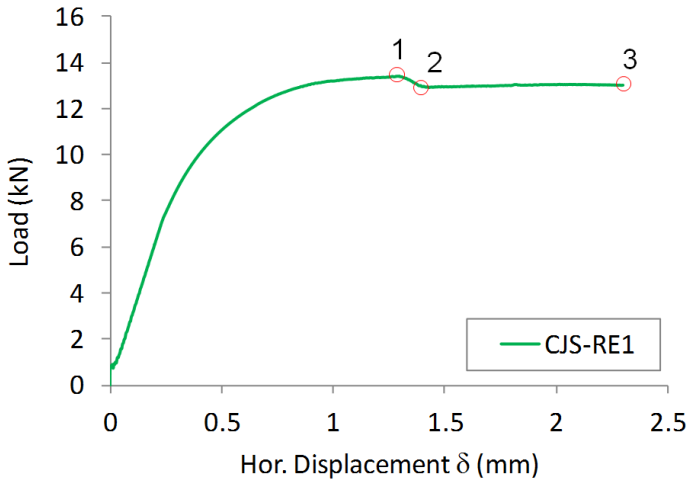

FIGURE 4.12: Load-displacement response from a simulated pushover test on a wallet; MAT-1

The evolution of the plastic points throughout the test are shown in Figure 4.13 at state 1 to 3 (Figure 4.12). At state 1, a tensile failure is obtained at the bottom right of the wallet. Such detachment of the wallet base was also found in actual experiments [EN17]. Along with the propagation of detachments at the bottom right, the wallet exhibits a rotation counterclockwise (Figure 4.14). This condition induces a further compression load at the left side of the wallet and shear failure can be observed at the bottom left. Then, at state 2, a tensile failure can be observed vertically on the left part of the wallet. Finally at state 3, the tensile failure propagated upwards and crosses the whole sample.

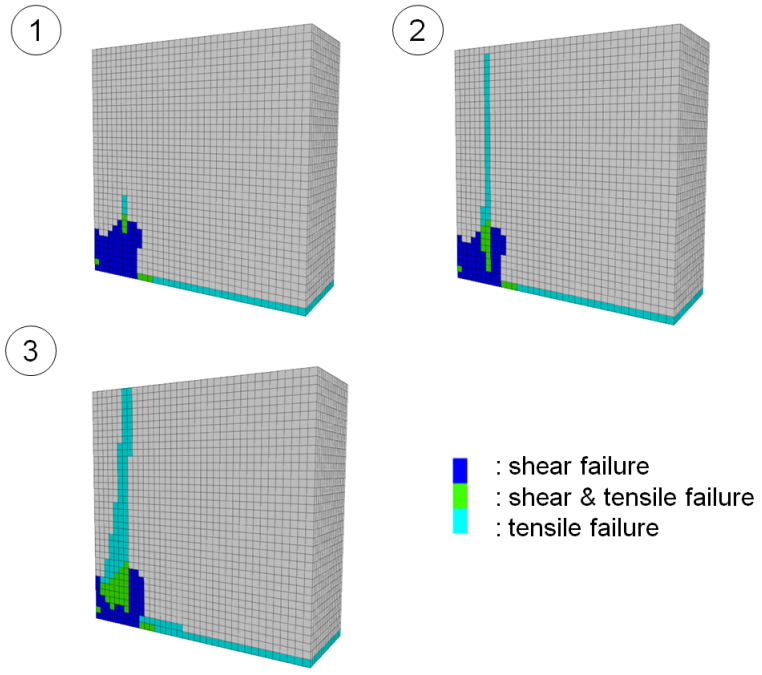

FIGURE 4.13: Evolution of the plasticity states in a simulated pushover tests using CJS-RE1 at different computation stages

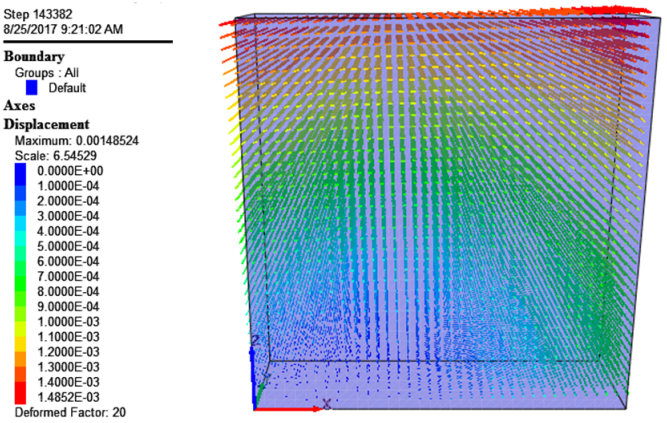

FIGURE 4.14: Rotation of the wallet (state 1)

The results of a simulated pushover test using CJS-RE1 show some basic features that can be observed in actual pushover tests where the wallet exhibits some detachments at the bottom part and also an overturning movement. Since no actual experimental tests were performed on this material it is difficult to draw a conclusion concerning the type of failure (more tensile type or shear type).

4.3 Validation of CJS-RE2 model for MAT-1

4.3.1 Further identification of parameters

The second level of the model need four additional parameters apart from those which were already identified in the first level of the model. These parameters are the initial elastic radius (R_{ini}) of the yield surface which gives the extent of the elastic domain, the isotropic hardening parameter A, and α_s which control the shear softening curves. R_{ini} can be identified from a compression test as the zone where a linear behavior is observed. A and α_s are determined by a trial-and-error method. From the analysis of different experiments and due to the less significance of the volumetric deformations in the behavior of quasi brittle materials, the maximum volumetric contraction state is stated to be equal to $R_{\text{mvc}} = 0.85 R_{\text{fail}}$. The set of model parameters for CJS-RE2 model are given in Table 4.5. Simulation with the second level of the model need twelve parameters to be identified with two elastic parameters (E and ν) and ten plastic parameters (γ, R_{fail}, $T^{\text{ini}}_{\text{r max}}$, $T^{\text{res}}_{\text{r max}}$, T^{ini}_{r}, β, R_{ini}, A, α_s and α_t). Two plastic parameters ($T^{\text{res}}_{\text{r max}}$ and α_t) are stated therefore not need to be identified.

The result of the identification process is shown in Figure 4.15. It can be seen that the second level of the model and specially the isotropic hardening function which is exponential has been able to capture the nonlinear behavior before reaching failure.

The basic features for CJS-RE2 obtained throughout the simulation of different triaxial stress paths is given in Appendix C.2.

TABLE 4.5: Identified CJS-RE2 model parameters for MAT-1; experiments from [SOS+14]

Elastic		Plastic	
E	= 1036 MPa	β	= 3.0
v	= 0.25 MPa	γ	= 0.84
		R_{fail}	= 0.22
		T^{ini}_{r}	= 100.8 kPa
		$T^{\text{ini}}_{\text{r max}}$	= 730 kPa
		$T^{\text{res}}_{\text{r max}}$	= 146 kPa
		R_{ini}	= 0.08
		A	= 0.00013
		α_t	= -0.5
		α_s	= -0.0003

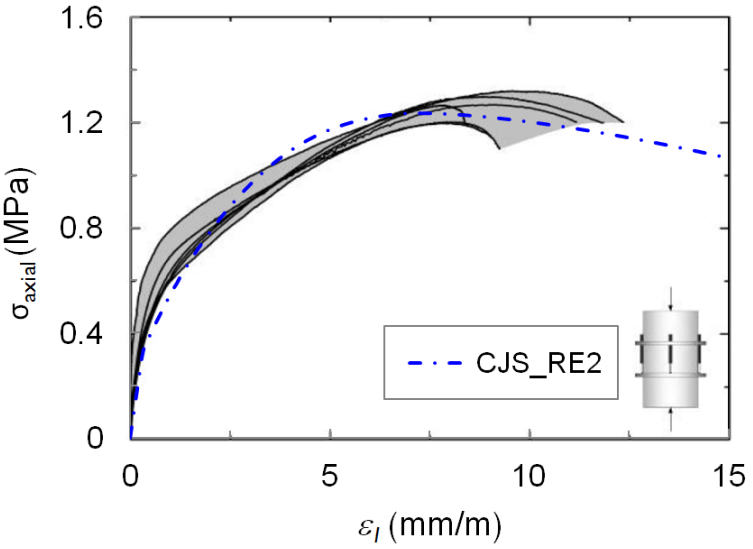

FIGURE 4.15: Simulation of a compression test with CJS-RE2 (MAT-1); experiments from [SOS+14]

4.3.2 Validation: Diagonal compression test

A numerical simulation of the diagonal compression test on the wallet is simulated as in the level-1 model. The global response of the wallet is given in Figure 4.16. The initial stiffness is similar to the one found with CJS-RE1, which means that the limited dimension of the elastic domain and the possible plastic behavior generated when the actual stress state reaches the shear yield surface may not greatly contribute to the overall behavior of the wallet. Accordingly, the first local peak dropped from 0.15 MPa with CJS-RE1 to 0.13 MPa (15% drop). This local peak of resistance is followed by a small drop of resistance as previously found with CJS-RE1. The main difference between the simulation using CJS-RE1 and CJS-RE2 lies in the limited increase of shear stress with CJS-RE2 which remains in the range of values found throughout actual experiments. It may be due to the existence of softening for the shear failure surface in CJS-RE2.

Figure 4.17 shows the evolution of the plasticity states during the simulation of diagonal compression test. Many elements in the vertical central zone of the wallet reached first the shear yield surface before the central elements at the surface of the wallet reached the tensile failure surface (state 1). Between state 1 and state 2, the tensile failure (elements are at the junction of the yield surface and the tensile failure surface) propagated to the upper and lower part of the wallet. At state 3, there is a continuous chain of elements at tensile failure (while at shear yield). It can be seen that some plastic points at state 3 are consistent with the crack pattern observed in the wall (Figure 4.3b). Finally, at state 4, the tensile

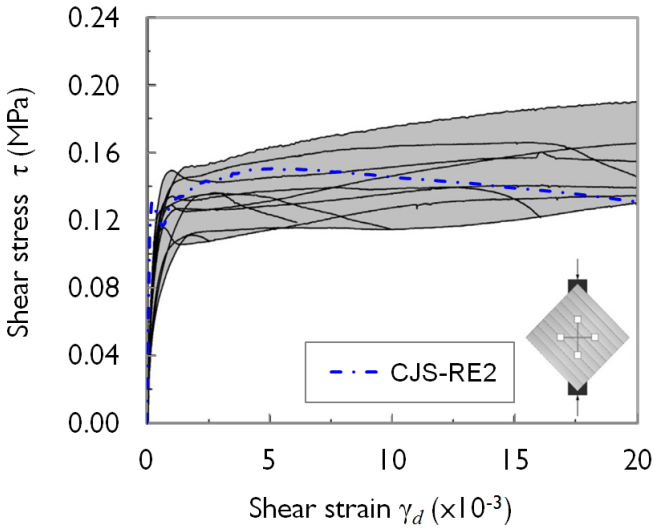

FIGURE 4.16: Stress-train response from a simulated diagonal compression test using CJS-RE2; experiments from [SOS+14]

failure extents with a larger domain than at state 3.

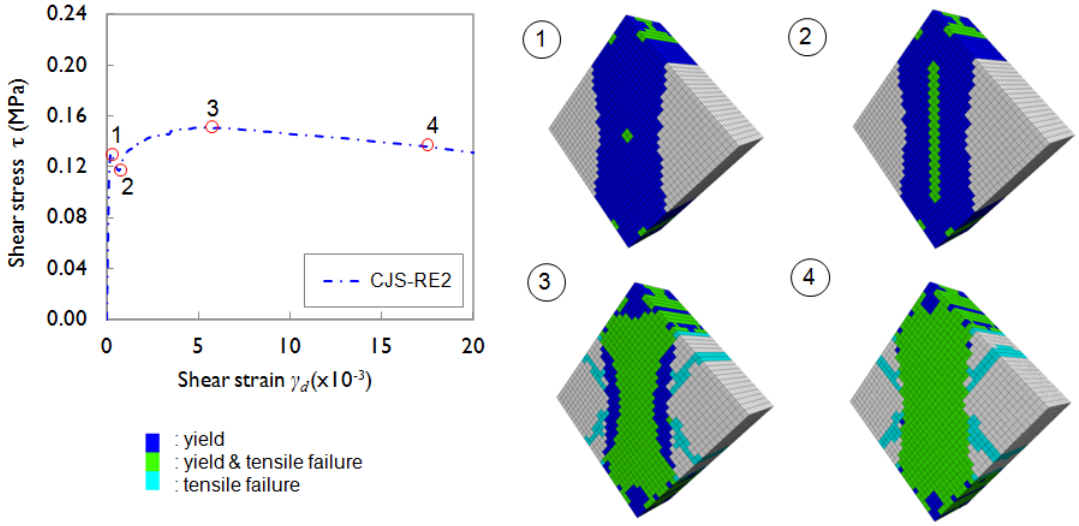

FIGURE 4.17: Evolution of the plasticity states in a simulated diagonal compression tests using CJS-RE2 at different computation stages.

Figure 4.18 shows the evolution of stress path in the central surface element of the wallet. Figures 4.18a-c-e-g are view sections of stress path in the meridian plane and Figure 4.18b-d-f-h are sections in the deviatoric plane.

The stress state reached first the yield surface. Eventually, tensile failure started at the central core of the wallet before the studied element. It led to a relaxation of stresses and then to a drop of the mean pressure before the stress path of the studied element reaches state 1 (Figure 4.18a-b). This deviation of the mean stress

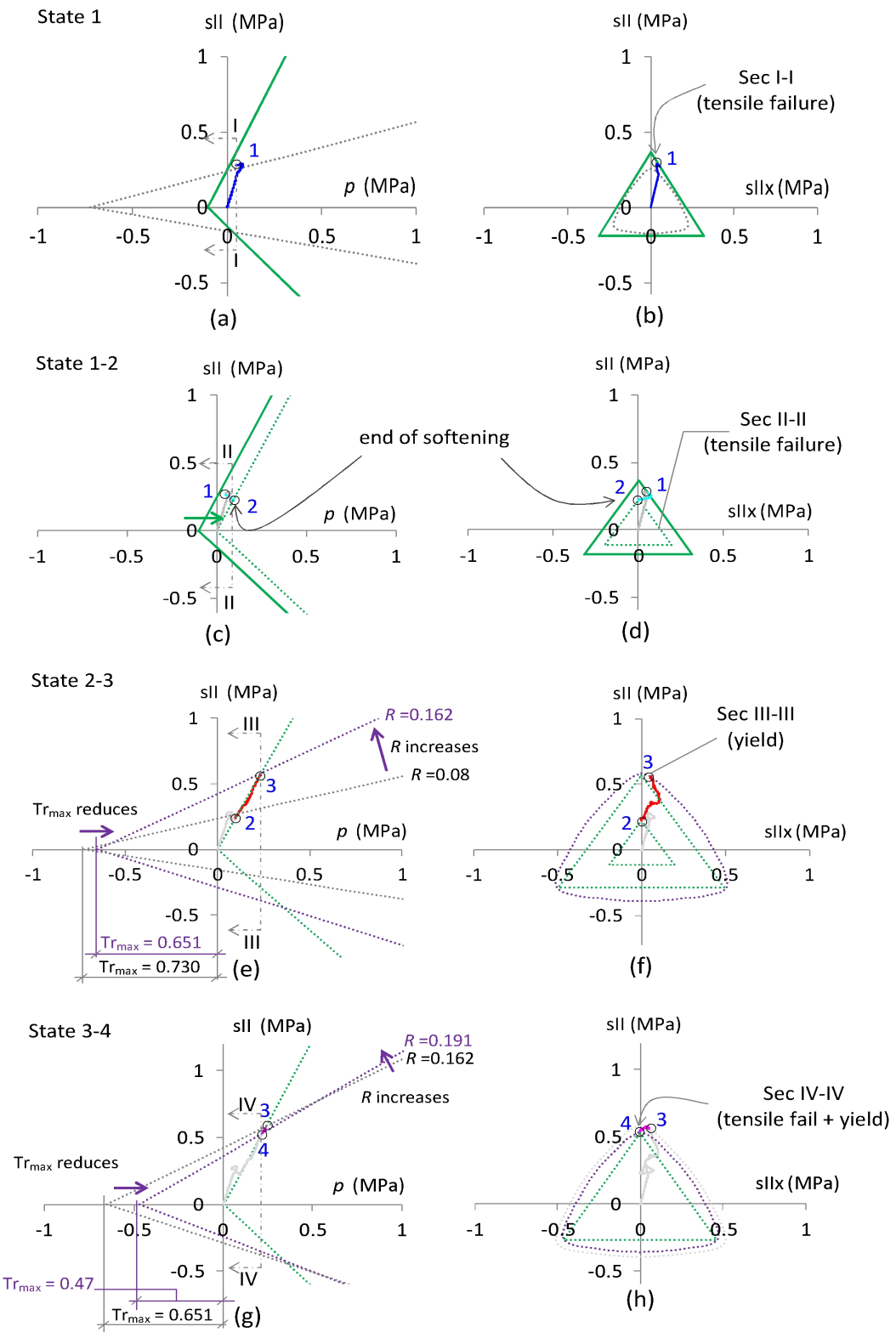

FIGURE 4.18: Stress path of an element in a simulated diagonal compression test (CJS-RE2).

towards smaller values explains why the tensile failure surface is reached by the studied element for a smaller value of s_{II} which is revealed in Figure 4.16 than in the case of CJS-RE1. From point state to state 2 (Figure 4.18c-d), the tensile failure surface softens (same feature for the yield surface) but during this period, the average radius of the yield surface keeps constant (softening is obtained by a reduction of the tensile resistance T_{r} and of the maximum tensile resistance T_{rmax}).

From state 2 to state 3 (Figure 4.18e-f), the stress path keeps on the tensile failure surface and just a small increase of the mean pressure is required to reach the shear yield surface. From now on, the stress path keeps at the junction of the tensile failure surface and of the shear yield surface. The softening of $T_{\mathrm{r\,max}}$ (that started previously when the tensile failure surface was reached) and the hardening of the mean radius R (the mean pressure increases due to the reserve of resistance of the wallet) are then again activated. Note that between state 2 to state 3, the rate of hardening (rotation of yield surface) is greater than the shear softening (translation of the yield surface).

From state 3 to state 4 (Figure 4.18g-h), the rate of hardening is getting slower (as plastic deformation are generated) than throughout the previous stage, while the shear softening process keep moving. This condition force the stress path to move from point 3 to point 4. From state 3 to 4, the softening of $T_{\mathrm{r\,max}}$ monitored the behavior of the element which can also be noticed at the scale of the wallet (many of the elements in the wallet hold this behavior). The drop is supposed to go on until the residual value for $T_{\mathrm{r\,max}}$ is reached.

To conclude, the shear softening in CJS-RE2 model has an important contribution to limit the re-increase of the shearing resistance which is excessive when using CJS-RE1 model. In CJS-RE2, the shear plastic mechanism (together with the shear failure surface) is coupled with the tensile plastic mechanism through the softening law driving the loss of the maximum resistance $T_{\mathrm{r\,max}}$. CJS-RE2 model was able to retrieve the average stress strain curve obtained throughout experiments within a wide range of deformations. However, one can note that the general ductility of the wallet is not well modeled with CJS-RE2 model with in particular a too high initial stiffness and a peak of the curve that is obtained for smaller deformations than in actual experiments. This effect may be attributed to the absence of interfaces when modeling the wallet [BBLM16].

4.3.3 Validation: Pushover test

A further simulation is carried out for the pushover test on a wallet with MAT-1 set of parameters as previously done with CJS-RE1. The resulting load-displacement responses is shown in Figure 4.19. It can be observed that the peak response is reached at a larger deformation than in the level-1 model (2mm with CJS-RE2 while 1mm with CJS-RE1). This higher ductility provided by CJS-RE2 is due to the limited domain of elasticity and the generation of plasticity earlier in the simulation.

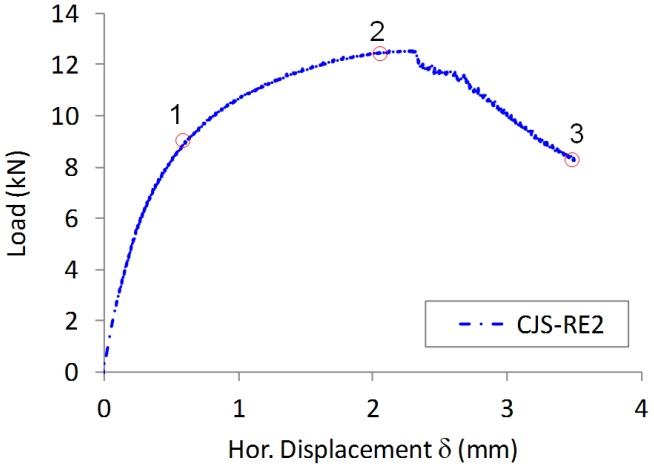

FIGURE 4.19: Load-displacement response from a simulated pushover test on wallet; MAT-1

The evolution of plastic points throughout the test is shown in the Figure 4.20 using the reference points in Figure 4.19. At state 1, the majority of the elements in the wallet are at shear yield. Nevertheless, there are some elements at tensile failure at the bottom right of the wallet like. At state 2, the tensile failure develops further at the bottom right. The tensile failure propagates vertically (pale blue elements). At this state, the wallet has lost more than 50% of its footholding compared to the beginning of the test. The value of the load carrying capacity is similar to what was found with CJS-RE1. Finally, at state 3, the wallet has exhibited a loss of its load carrying capacity while a large extent of elements have reached the tensile failure at the left side of the wallet. The zones affected by tensile failure are more extended in the case of CJS-RE2 than for CJS-RE1 but the capacity to resist to the horizontal loading is not greatly different (decrease of 10%) than with CJS-RE1.

For conclusion, CJS-RE2 model gives a general load-displacement softer than the one simulated by CJS-RE1 model without a significant modification of the loading

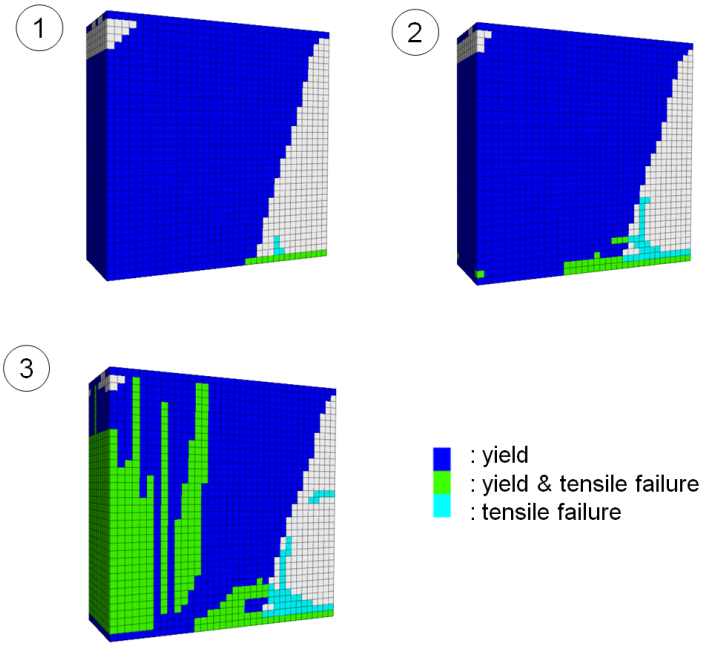

FIGURE 4.20: Evolution of the plasticity states in a simulated pushover tests using CJS-RE2 at different computation stages.

capacity. A general softening of the load carrying capacity is obtained, that was not observed in the simulation using CJS-RE1 model.

4.4 Simulations with interfaces for MAT-1

The interfaces existing in the actual wallet result from the construction technique (successively compacted layers of earth of about 10cm each one). In this section, interfaces will be modeled to identify their possible contribution to the overall behavior of the wallet during a diagonal compression test and pushover test. A Mohr-Coulomb model will be used as the constitutive model for the interfaces [Ita09]. For the homogeneous material constituting the layers, a CJS-RE2 model will be used together with the set of model parameters previously identified. The geometrical model is shown in Figure 4.21 where nine earth layers separated by interfaces are depicted.

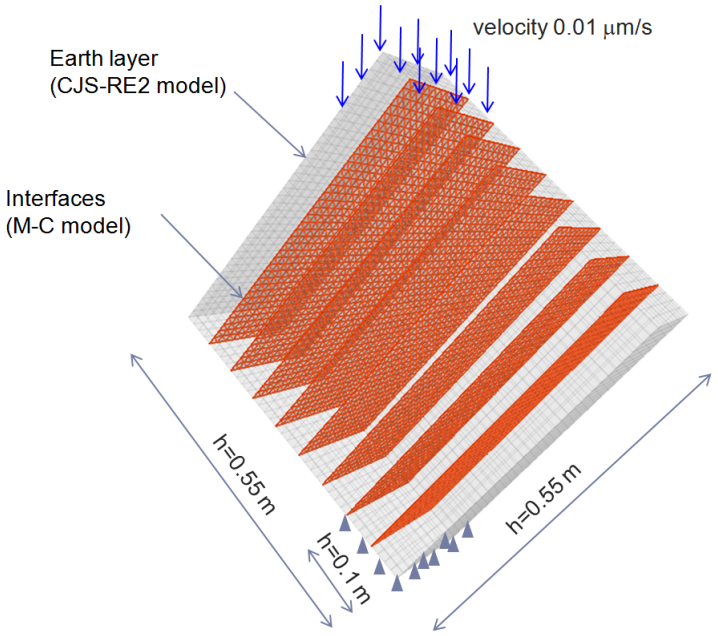

FIGURE 4.21: Model of diagonal test with interfaces

4.4.1 Identification of the interface parameters

Two sets of parameters will be used for the interfaces. The first one corresponds to the recommendation of Miccoli et al. [MOS+14]. In fact, there is no available data for the interfaces for MAT-1 since no experimental tests to identify their behavior were carried out. The elastic normal stiffness k_n is then equal to $100E$, E being the Young modulus of the material constituting the layers. As recommended by the same authors, we suppose that $k_s{=}k_n/2(1+\nu)$.

The second set is derived from recommendation by Itasca [Ita09] but considering that interfaces provide ductility in the system. Then, it is stated that the elastic

stiffness k_n is equal to 1/5 times the usual recommended value given by the relationship:

$$k_n = \max \left[\frac{(K^e + 4/3G^e)}{\Delta z_{min}} \right] \tag{4.3}$$

where Δz_{min} is the smallest element size within the modelling. In this case, k_n is found equal to $15E$. It models the loss of stiffness within interface as shearing takes place. Indeed, a Mohr-Coulomb model generally provides a too stiff behavior.

The interface angle of friction ϕ_i was assumed to be 37° and the dilatancy angle ψ_i equal to zero according to Miccoli et al. [MOS+14]. As recommended by these authors, the cohesion (C_i) was estimated as a function of the tensile strength, namely as $1.8f_t$. By using this relationship, the cohesion of the interfaces is about 60% of the layers cohesion. Finally, the tensile strength of the interface (f_t^i) is set equal to 90% of the layers tensile strength [MOS+14]. The set of model parameters for the interfaces model are given in Table 4.6.

TABLE 4.6: Parameters assumed for the Mohr-Coulomb type model for the interfaces

Elastic (Int 1†)		Elastic (Int 2‡)		Plastic‡)	
k_n	= 104 GPa	k_n	= 16.3 GPa	ϕ_i	= 37°
k_s	= 41.4 GPa	k_s	= 6.5 GPa	C_i	= 181.4 kPa
				f_t^i	= 90.72 kPa
				ψ_i	= 0

† ref [MOS+14]
‡ k_n equation (4.3) reduced by 5

4.4.2 Diagonal compression test

The geometry and boundary condition for diagonal compression test are imposed as in the homogeneous model (Figure 4.7). The global stress-strain response of the model CJS-RE2 without interfaces and with interfaces (set 1: CJS-RE2+int 1 and set 2: CJS-RE2+int 2) are given in Figure 4.22. The simulation (CJS-RE2+int 1) does not bring about news features in the global response of the wallet with a ductility of the overall system which is quite similar to that was previously found in Figure 4.16. In the case of model (CJS-RE2+int 2), the initial stiffness is less steep than what was found in Figure 4.16 and closer to what was found in the experiments. For the set of parameters that are equal for set 1 and set 2 except the elastic stiffnesses of the interfaces, one can note that the overall strength of the

wallet decreased for set 2 but keeps in the range of values found in the different actual tests.

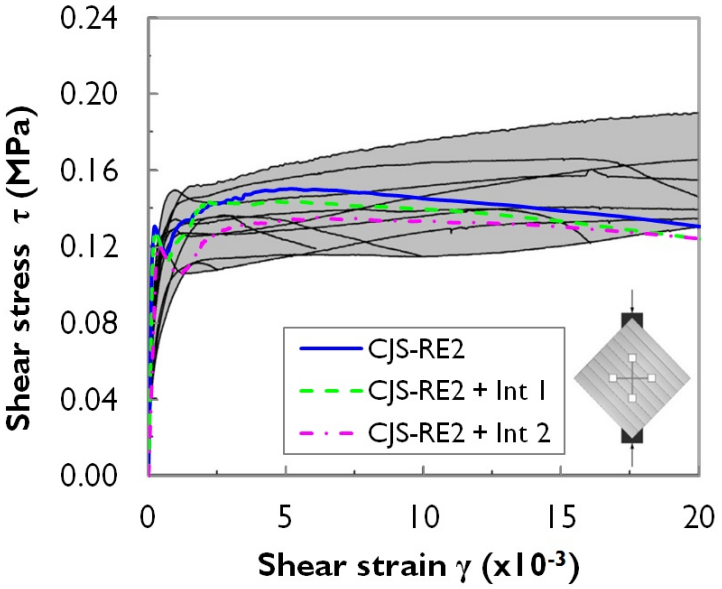

FIGURE 4.22: Diagonal compression test of CJS-RE2 model without and with interfaces results; experiments from [SOS+14]

Figure 4.23 depict the interfaces stress state (shear stress-normal stress) for model CJS-RE2+int 2 together with the Mohr Coulomb criterion associated to the interfaces. The interfaces are grouped into four separated groups. Group 1 contains the two interfaces in the lower part of the system, group 2 and 3 at the midheight of the wallet (Figure 4.23a) and group 4 two interfaces at the top of the system. Two references state are defined in the Figure 4.23b which are the state at the first peak (state A) and the state at the end of simulation (state B). Each point in Figure 4.23c,d represent the shear-normal stress state at a point of an interface belonging to a group i. At state A and B, no interfaces failed either in a shearing or in a tensile mode. Moreover, one can note that the stress states on interface 1 and on interface 4 are similar. The same condition also observed between stress states on interface 2 and 3. This inferred that the boundary condition and also the loading condition are symmetrical.

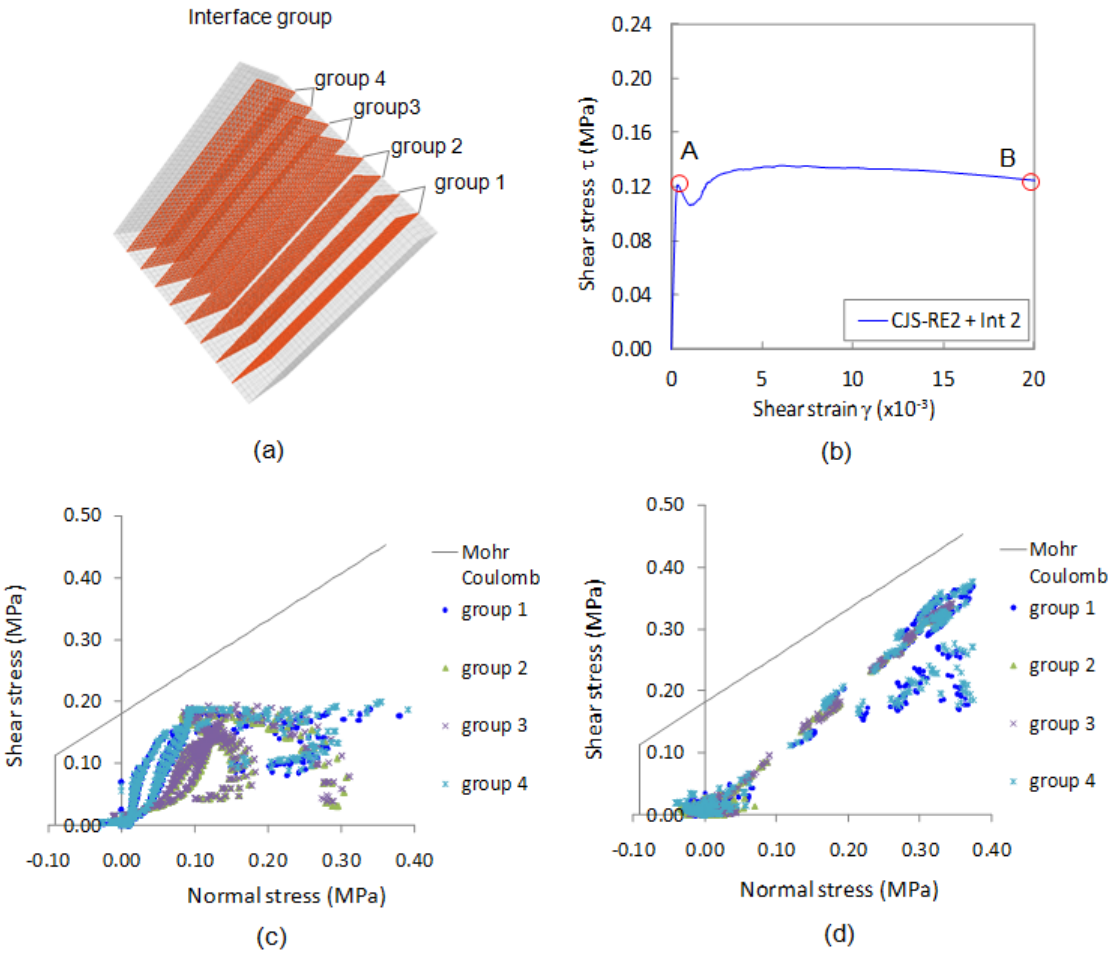

FIGURE 4.23: Stress state on the interfaces together with Mohr-Coulomb criterion for the interfaces in the diagonal compression test; a: interface group, b: reference states A and B, c: state A, d: state B.

4.4.3 Pushover test

A pushover test is simulated with the set of parameters corresponding to MAT-1. The geometry is similar to the one previously used but here interfaces are also modelled (Figure 4.24). Two different simulations are carried out by using two levels of the model and interfaces with set 2.

The global load-displacement response is given in Figure 4.25. As expected CJS-RE2, gives a softer behaviour than CJS-RE1 model. It can be observed that after the peak of response, CJS-RE1 curve presents a small drop followed by a stabilisation. On the other hand, CJS-RE2 curve exhibit a huge softening. This implies that the shear softening plays a role in the post peak behaviour.

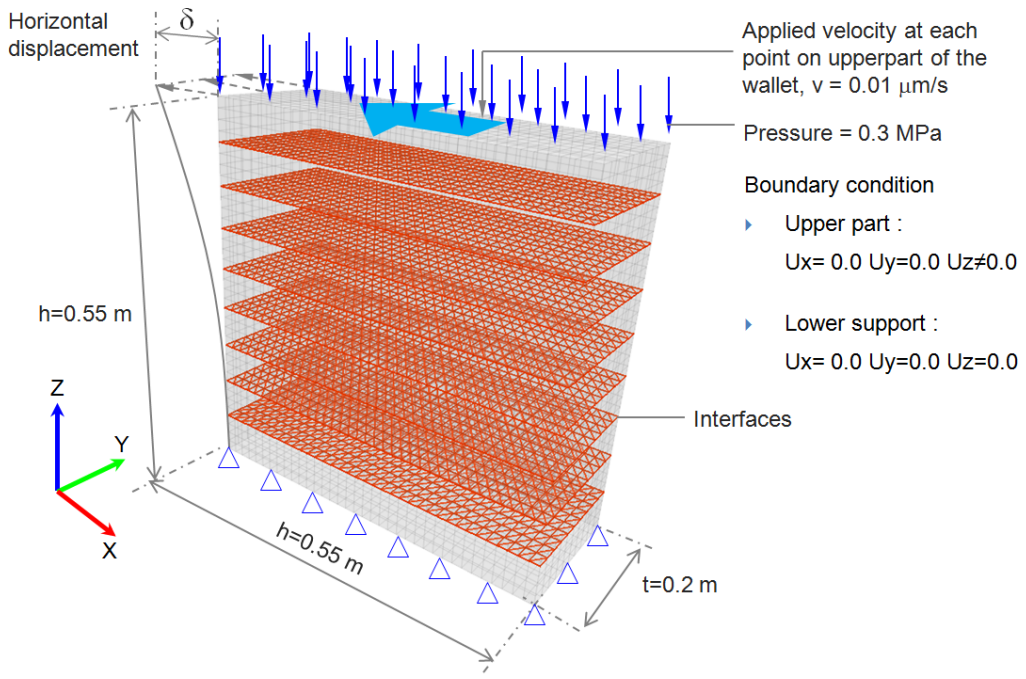

FIGURE 4.24: Model of pushover test on wallet with interfaces

Figure 4.26 depicts the corresponding plastic points at displacement of 3mm (point A in the Figure 4.25). Simulation with CJS-RE1 + int2 shows a tensile failure propagating from the bottom left to the upper right (Figure 4.26a). It is also seen detachments at the bottom right of the wall as previously can be observed in the homogeneous model. Using CJS-RE2 + int2 (Figure 4.26b), the tensile failure appears to be along a vertical on the left side of the wall.

Figure 4.27 shows a comparison between model CJS-RE2 and CJS-RE2 + int2. It can be seen that interfaces contribute to give a softer response than the corresponding homogeneous model. It results from the reduced stiffness parameters

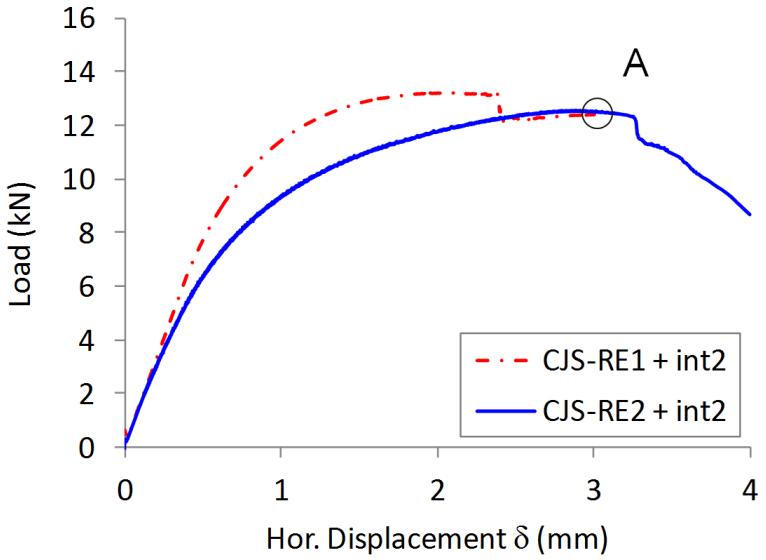

FIGURE 4.25: Simulation of a pushover test with CJS-RE1 and CJS-RE2 model with interfaces; set 2

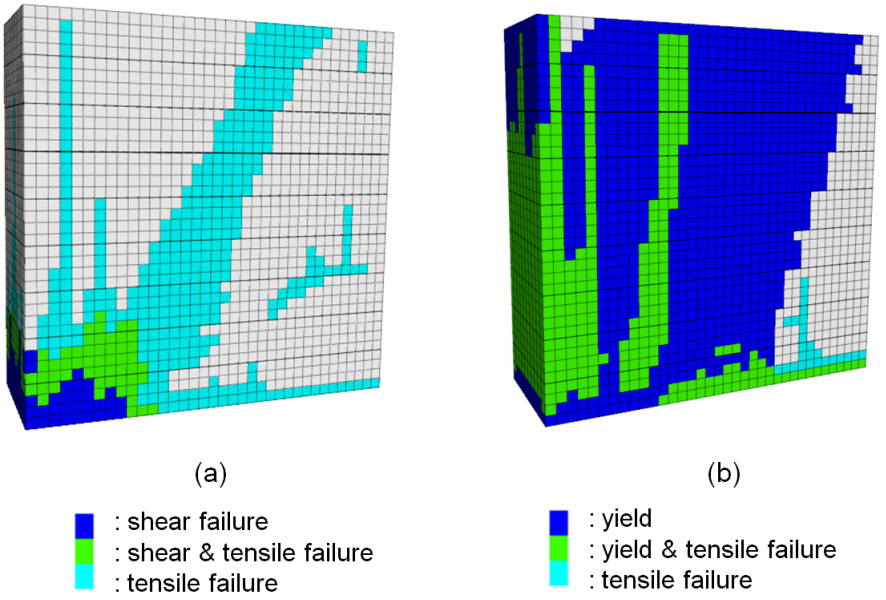

FIGURE 4.26: Plastic points in the wallets at the peak response; (a): CJS-RE1 + int2 (b): CJS-RE2 + int2

chosen for the interfaces. Nevertheless, they do not modified the overall resistance of the wallet to the lateral loading.

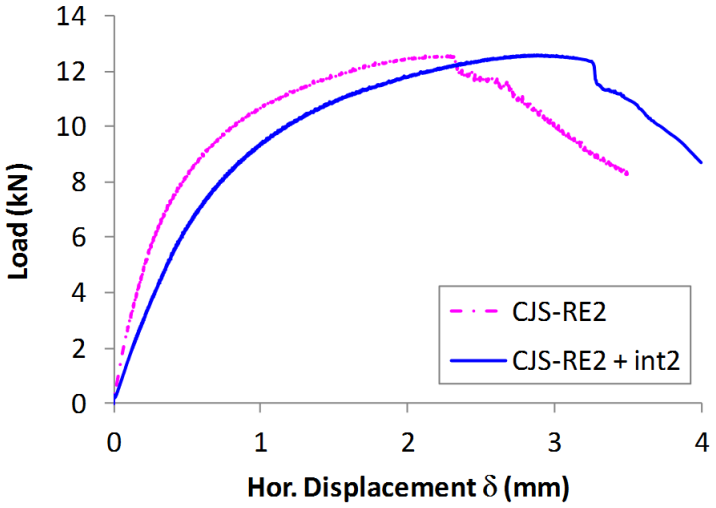

FIGURE 4.27: Simulation of a pushover test with CJS-RE2 with and without the modelling of the interfaces

Figure 4.28 shows the stress state (shear vs normal stress) at the different points of the interfaces for state A and state B. The groups are similar to the ones defined in subsection 4.4.2. According to Figure 4.28c, at peak state, the interfaces that exhibits most shearing belong to group 1 while the interface stress points that are closer to the maximum tensile resistance belongs to group 2. In Figure 4.28d, as expected, the influence of the shear softening in the layers is visible in the interfaces. This softening tends

As a conclusion to this part, if one follows the recommendations by Miccoli et al.[MOS+14] where the interface parameters are very different from those of the layers, there is no clear influence of the interfaces in the behavior since the Mohr-Coulomb model used to model their behavior remains very stiff before reaching the Mohr-Coulomb criterion. A decrease of the normal and tangential stiffnesses interfaces seems to be necessary to better model the actual behavior of a wallet in a diagonal compression tests inducing a softer behavior at the beginning of the test. However, it does not significantly modifies the simulated resistance of the wallet. Therefore, in practice, due to the uncertainties in the experiments related to the intrinsic heterogeneity of the wallets and to the lack of a straightforward procedure to identify the parameters for the interfaces, the use of a homogeneous model to simulate the behavior of a diagonal compression test in a rammed earth context is recommended.

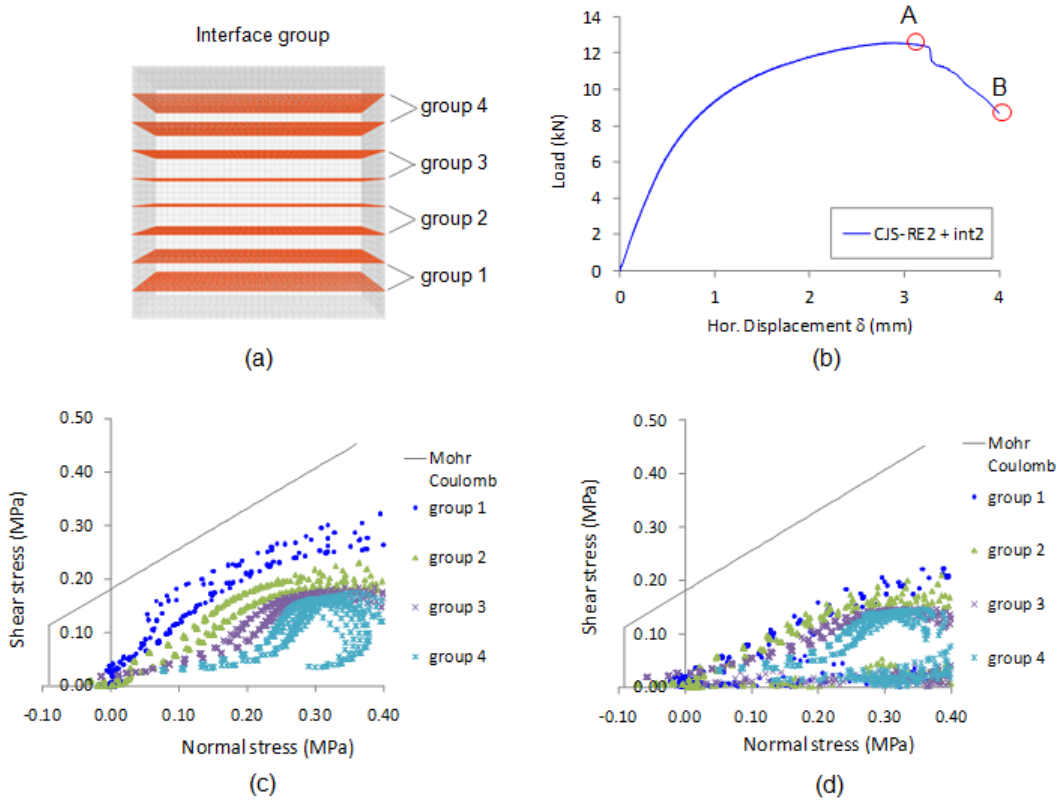

FIGURE 4.28: Stress state of the interfaces compare with Mohr Coulomb criterion in the pushover test; a: interface group, b: reference state, c: interface stress state A, and d: interface stress state B.

The resistance of the wall is not modified when interfaces are taking into account in the modelling of a pushover test. However, the effect of interfaces is more clear than through a diagonal compression test where they allows to greatly increase the ductility of the system. Here again, when the global resistance of the wallet is investigated, we do not recommend the use of interfaces.

4.5 Validation of CJS-RE1 for MAT-2

To get a better insight into the relevance of the previous validations, a second validation is provided using MAT-2. The first level of the model (CJS-RE1) is first used with the appropriated set of parameters for MAT-2. Some parameters are identified from compression tests and also from a direct shear test. Because of the deficiency of available experiment tests required to identify all the model parameters, some relationships with the Mohr-Coulomb model are used (Appendix B.2). Then, the validation of the model is undertaken on the pushover test.

4.5.1 Identification of the model parameters

Following the procedure given in subsection 4.2.1 and the data given in subsection 4.1.2, the set of model parameters for CJS-RE1 model was identified and is given in Table 4.7.

TABLE 4.7: Identified CJS-RE1 model parameters for MAT-2; experiments from [EN17]

Elastic		Plastic	
E	= 760MPa	β	= 1.0
ν	= 0.25MPa	γ	= 0.85
		R_{fail}	= 0.39
		T_r	= 160kPa
		T_{rmax}	= 350kPa
		α_t	= -1.0

The result of the identification process for a compression test is given in Figure 4.29. There is no available curve for the experiment in compression.

4.5.2 Pushover test

A simulation of a pushover test, with the material, the geometry and the boundary conditions imposed by El Nabouch [EN17] is carried out (Figure 4.30).

Figure 4.31 shows the load-displacement curve of the pushover test with three reference states and also the response recorded throughout the experiments. The simulation with CJS-RE1 reaches its peak at the level of 50kN with a corresponding displacement of 7mm. The curve is generally stiffer than in the experiments which was expected and the estimation of the ultimate loading capacity is higher

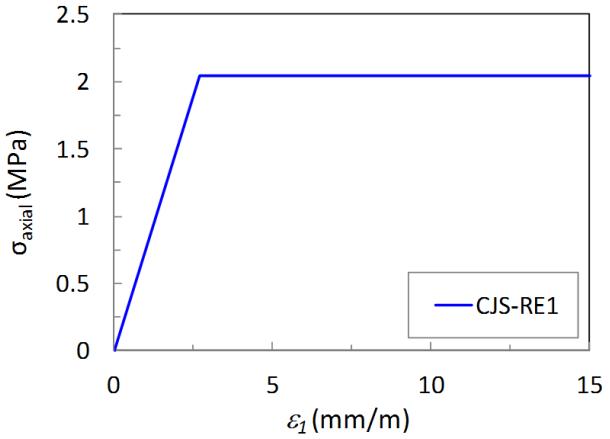

FIGURE 4.29: Result of the identification of CJS-RE1 parameters; simulation of a compression test; experiments from [EN17]

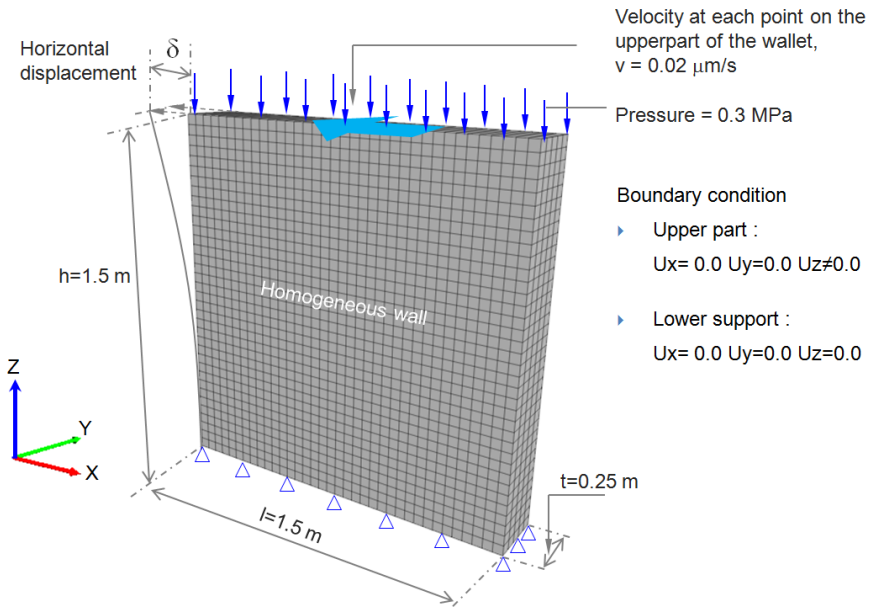

FIGURE 4.30: 3D-Model for the pushover test on a wallet with MAT-2

25% than the average of the experiments. The use of CJS-RE1 may be useful to have a first estimate of the loading capacity of the system with few effort to identify the model parameters.

Figure 4.32 depicts the plastic states at three different computation stages (reference states given in Figure 4.31. At state 1, a detachment at the wallet bottom right is noticeable together with a zone at shear failure in the bottom left part. At state 2, a tensile failure is found to propagate from the bottom left to top left of the wallet. This condition is stabilise until state 3. The general failure mode is quite the same as in the wallet of MAT-1. Nevertheless, the pattern of plastic

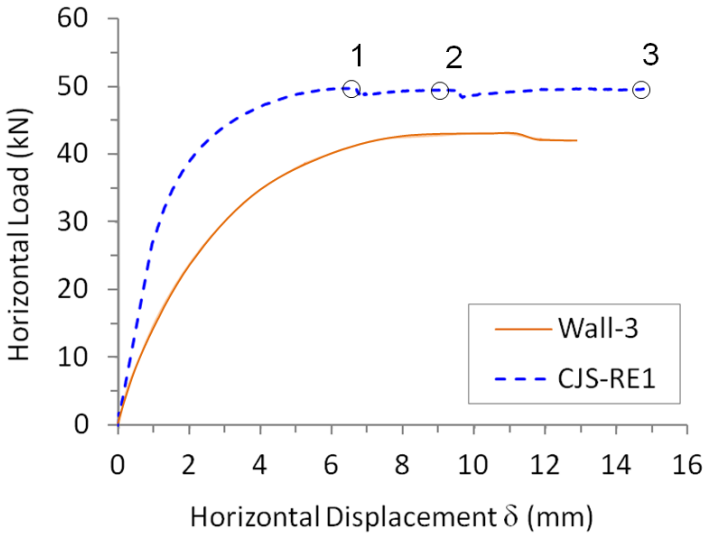

FIGURE 4.31: Load-displacement response from a simulated pushover test on a wallet vs experiments; MAT-2

points is different with the experimental evidences where a quasi diagonal crack was observed for wall-3.

4.6 Validation of CJS-RE2 for MAT-2

4.6.1 Further identification of parameters

Three further model parameters must be identified for CJS-RE2: R_{ini} which gives the limit of the elastic domain, the isotropic hardening parameter A, and α_s which controls the shear softening curves. Due to the limited data of compression stress-strain curve, A and α_s are defined as in the MAT-1. It will seen that these parameters are of less influence in the result of the simulation (Appendix F). The set of model parameters for CJS-RE2 model are given in Table 4.8. A simulation of a compression test is also given in Figure 4.33.

4.6.2 Pushover test

Figure 4.34 shows the result of the simulation of the pushover test performed by El Nabouch [EN17] with three reference states. The result is closer to the experimental curve than for CJS-RE1 qualitatively and quantitatively. The response is softer than first level of the model. In addition, the maximum resistance is lower

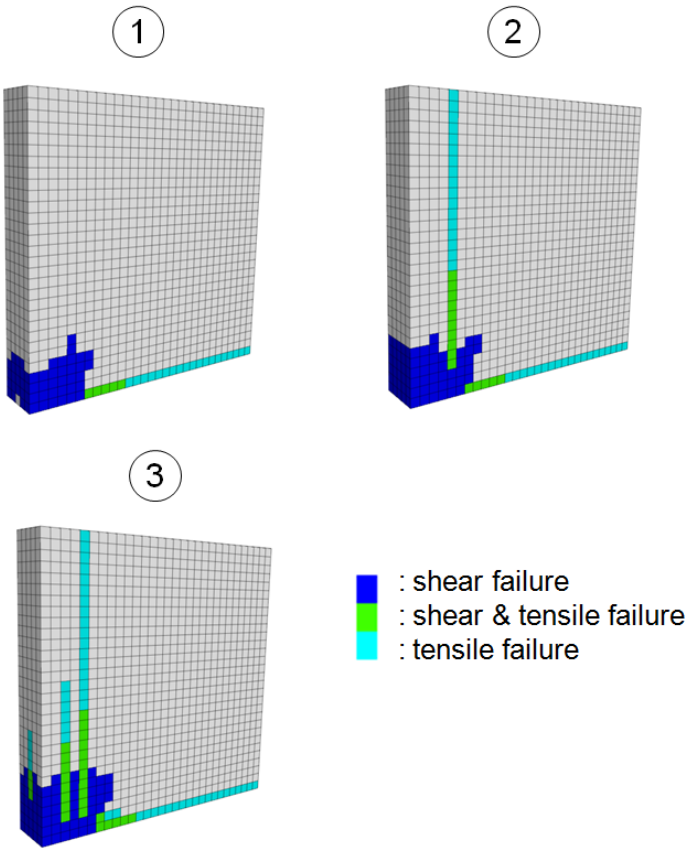

FIGURE 4.32: Plasticity states in a simulated pushover tests using CJS-RE1 at different computation stages; MAT-2

TABLE 4.8: Identified CJS-RE2 model parameters for MAT-2; experiments from [EN17]

Elastic		Plastic	
E	= 760MPa	β	= 1.0
v	= 0.25MPa	γ	= 0.85
		R_{fail}	= 0.39
		T_r^{ini}	= 160.0kPa
		$T_{\text{r max}}^{\text{ini}}$	= 350kPa
		$T_{\text{r max}}^{\text{res}}$	= 70kPa
		R_{ini}	= 0.16
		A	= 0.00013
		α_t	= -0.5
		α_s	= -0.0003

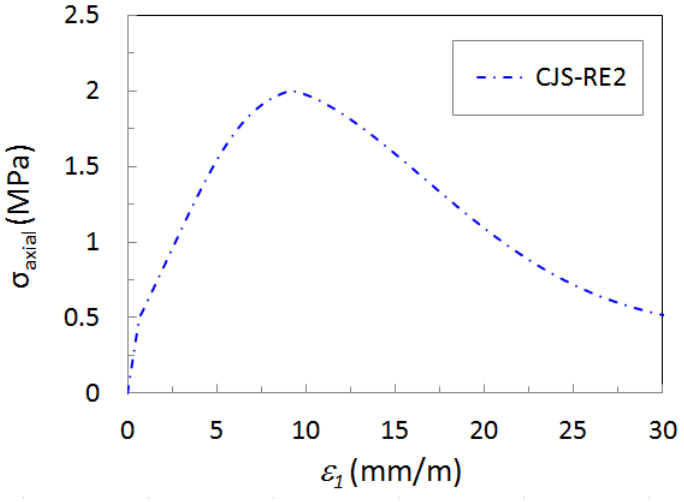

FIGURE 4.33: Result of the identification of CJS-RE2 parameters for MAT-2; simulation of a compression test

than CJS-RE1.

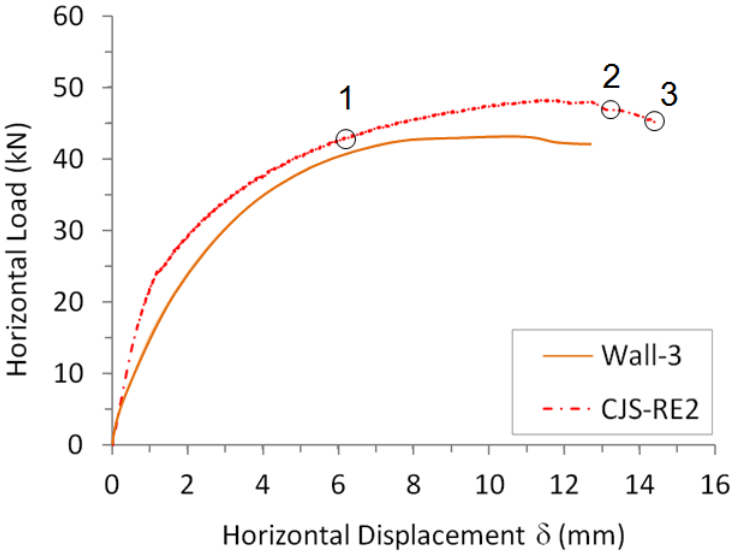

FIGURE 4.34: Load-displacement response from a simulated pushover test on wallet; MAT-2

Figure 4.35 depict the plastic states at three different computation stages (point 1,2, and 3 in the Figure 4.34). At state 1, most of the wall is at shear yield. Detachment (tensile failure) is here again found at the bottom right of the wallette. At state 2 and 3, a tensile failure appears at the bottom left of the wallette, then it develop vertically at the left part of the wallette. The pattern of plastic points are still different from the experimental evidences where a quasi diagonal crack was observed in wall-3.

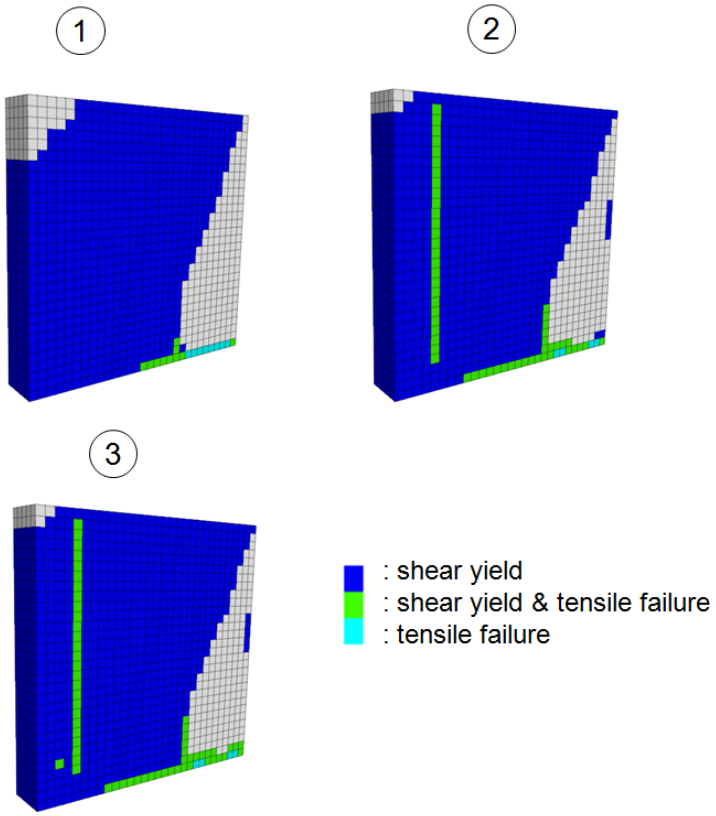

FIGURE 4.35: Plasticity states in a simulated pushover tests using CJS-RE2 at different computation stages; MAT-2

For conclusion, CJS-RE2 model gives a general load-displacement which is softer than CJS-RE1 with a slightly lower load carrying capacity. Simulation with CJS-RE2 model gives a result closer to the actual experimental curve compared with CJS-RE1, but the features of failure are different than those found in the experiments. Further effort is to see whether the interfaces might have a role in the case of the pushover test.

4.6.3 Pushover test with the modelling of interfaces

Two set of parameters is proposed for the interfaces. The first set is taken by using interfaces elastic stiffness derived from the reduced elastic properties of the layer with reduction factor of 5. The second set is taken by using a reduction factor of 2.

The interface friction angle ϕ_i was assumed to be equal to 45° as in the layer. This assumption is based on the results of direct shear test (large shear box) from El Nabouch [EN17], where the interface friction angle and layer friction angle are found to be almost the same. The interface dilatancy angle ψ_i is taken as zero as

in the MAT-1. The interfaces cohesion (C_i) was taken as 80% of the layer cohesion according to the direct shear test result with large shear box [EN17]. Finally, the tensile strength of the interface (f_t^i) is set equal to 90% of the layers tensile strength. The set of model parameters for the interfaces model (Mohr-Coulomb model with linear elasticity) are given in Table 4.9.

TABLE 4.9: Parameters assumed for the Mohr-Coulomb type model for the interfaces

Elastic (Int 1†)		Elastic (Int 2‡)		Plastic‡)	
k_n	= 4.38GPa	k_n	= 10.9GPa	ϕ_i	= 45°
k_s	= 1.75GPa	k_s	= 4.4GPa	C_i	= 160kPa
				f_t^i	= 144kPa
				ψ_i	= 0

† k_n equation (4.3) reduced by 5
‡ k_n equation (4.3) reduced by 2

Figure 4.36 depicts the result for the simulation of the pushover test for MAT-2 with interfaces. Based on the Figure 4.36, it is shown that interfaces significantly influences the ductility of the system without any important effect in terms of the loading capacity. It seems that, a reduction of the interface elastic stiffnesses derived from the layers properties by a factor of 2 would be more suitable to conform the experimental results.

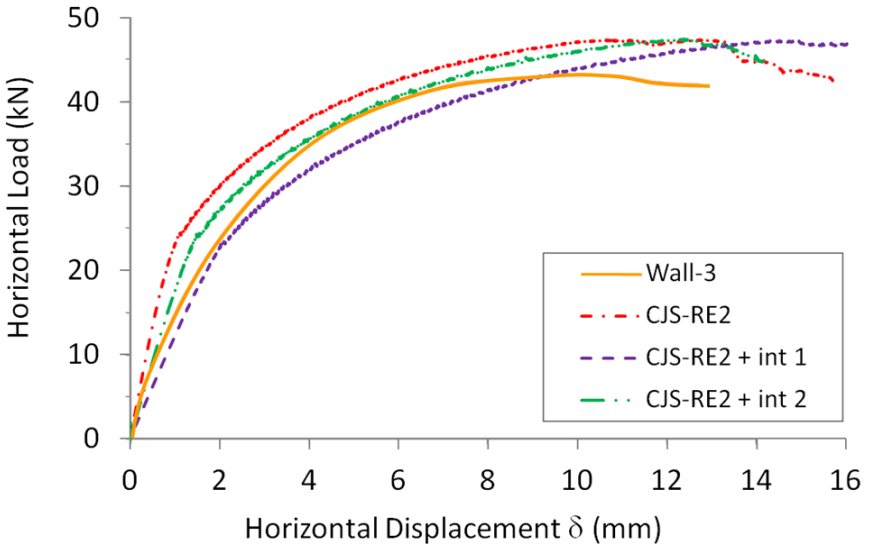

FIGURE 4.36: Pushover test with CJS-RE2 model with interfaces for MAT-2

Figure 4.37 depict plastic states at the end of simulation by using two differents model. The first is modelled by using CJS-RE1 + interfaces set 2 and the second CJS-RE2 + interfaces set 2. It is shown that the result is similar to what was found for the simulation of the pushover with homogeneous system.

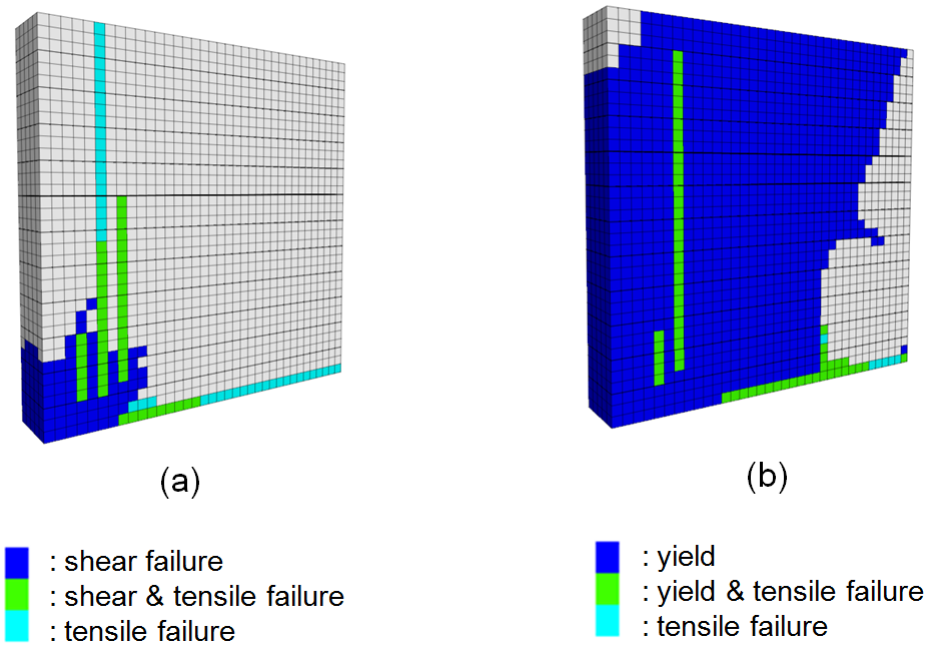

FIGURE 4.37: Plastic points in the wallettes at failure; (a) CJS-RE1 + int 2, (b) CJS-RE2 + int 2

To conclude this chapter, a validation of CJS-RE was proposed by simulating two different boundary value problems after an identification of the model parameters on homogeneous tests. These reference experimental tests involve a diagonal compression test and a pushover test on wallettes. CJS-RE1 was able to qualitatively retrieve the resistance of the rammed earth systems and may be used as a first estimate of the problem (in terms of initial stiffness and loading capacity). CJS-RE2 model allowed a fairly good estimate of the resistance of the rammed earth systems. However, in the simulations, the cracking pattern was different than the one observed in the experiments.

The modelling of interfaces was carried out to refine the simulations even if in experiments their properties were not found that different than those of the layers. The Mohr-Coulomb model used for modelling their mechanical behavior being too stiff. A reduction of the elastic interface stiffness was proposed. Even if the chosen value was excessively low, interfaces may only give some extra ductility without playing a significant role in terms of redistribution of stresses. A more refined model for them would have give more precise information of their role.

A parametric study shown in Appendix F is undertaken to better understand the sensitivity of the model parameters of the layer throughout the diagonal compression test and the pushover test.

Chapter 5

Conclusion and perspectives

General conclusion
In this works, an elastoplastic plastic model for studying the mechanical behaviour of rammed earth has been presented and implemented in a commercial code (FLAC and FLAC 3D). This model holds two plastic mechanisms of deformation, one related to phenomena associated to purely deviatoric stresses and the other related to tensile phenomena. Two levels of complexity of the model are designed and can be selected according to the amount of information available to identify the model parameters. The first level holds the features of an elastic perfectly plastic model, the second level is an elasto-plastic model with hardening and softening rule. They are supposed to be used for context where only monotonous loadings are acting on the system.

The identification of the model parameters was performed on the basis of some experiments existing in the literature related to rammed earth. Generally, four experiments are required to identify the set of model parameters. Two compression tests with different confining pressures, a uniaxial tensile test, and an extension test for a enough high confining pressure. Nevertheless, in this study, just some of the parameters could be obtained from experiments due to limited kinds of available experiments. Then, some parameters were stated from relationships existing with the Mohr-Coulomb model.

A validation is then proposed by using a diagonal compression test and pushover test on a homogeneous and non-homogeneous system (taking into account interfaces) of a wallet. Based on the simulation, the simple elasto-plastic CJS-RE1 model was able to capture some basic features of the diagonal compression test at low deformations related to a tensile failure. But, subsequently a large reincrease of the resistance is observed. In the case of the pushover test, the first level of model can fairly capture the mechanism of failure with a detachment at the base

of the wallet and an overturning movement.

A better prediction of loading capacity of the wallet is obtained using CJS-RE2 model. More ductility is obtained by the existence of a limited domain of elasticity and by a softening of the shear yield surface. The shear softening law creates a coupling between the tensile failure surface and the shear yield surface (and also with the shear failure surface) where both the yield surface evolution and the maximum shear resistance are influenced by the existence of a tensile failure in the material.

Finally, the role of interfaces on the behaviour of rammed earth in diagonal compression test is considered. If the identification is processed according to the recommended values by [MOS+14], the modelling of the interfaces does not bring about much in the prediction of the ultimate loading capacity of the system or on its ductility. A reduction of the interface elastic stiffness may be required to better reflect the apparent reduction of ductility of the interfaces throughout loading. An elasto-plastic model for the modelling the behavior of interface would be more relevant. On the overall, we found that the modelling of interfaces in rammed earth systems is oversized if the loading capacity is the only property that needs to be estimate. The use of a homogenous system may be quite sufficient in most of cases for rammed earth systems loaded monotonously.

Perspectives

The simulation results of this study is based on the hypothesis that rammed earth behaves like a quasi brittle material (ie:concrete). Further experimental tests will be require to clearly identify the dissymetry of the deviatoric failure surface. Compression tests showed that the material may experience a degradation of the elastic properties when subjected to cycles together with permanent deformations. This aspect can only be retrieved if a damage elasticity is involved in the model. A further sophistication of CJS-RE (a third level) could then be introduced with a CJS-RE3 model, where the cyclic behavior of the material could be taken into account. In that case, a kinematic harding should be introduced together with damage elasticity. Finally, the use of a more refined model (than a Mohr-Coulomb model) for the interfaces between layers may improve the quality of the prediction. More precisely, there is a need to model the decrease of the apparent stiffness of the interfaces when they are loaded together with the possibility of irreversible slippage within the interfaces.

Appendix A

Identification of CJS-RE parameters

This section provides the method to identify the model parameters. Most of the parameters can be identified through experiments and only two parameters need to be obtained by a trial-and-error method. In all the cases, two compression tests with two different confining pressures, a tensile test and an extension test would be required. If some experiments are not available, it is possible to estimate some parameters from correlations involving the Mohr-Coulomb model or to use usual relationships. In the latter case, it may just give a rough estimate for them. Herein, the presentation of the identification process is given according to the nature of the parameters, related to the elastic mechanism or the plastic mechanism.

A.1 Elastic parameters

A.1.1 Young modulus E

The Young modulus can be identified from the initial slope of the stress-strain curves in the uniaxial compression test (Figure 3.11a). Therefore, it can be expressed as:

$$E = \frac{\dot{\sigma}^{+}_{axial}}{\dot{\varepsilon}_1} \tag{A.1}$$

with σ^{+}_{axial} is the axial compressive stress (MPa) and ε_1 is the corresponding axial strain.

A.1.2 Poisson ratio ν

The Poisson ratio is identified from the initial slope of the volumetric deformation curve in the uniaxial compression test (Figure 3.11b). This ratio is equal to:

$$(1 - 2\nu) = \frac{\dot{\varepsilon}_v}{\dot{\varepsilon}_1} \tag{A.2}$$

with $\dot{\varepsilon}_v$ the increment of the volumetric deformation and $\dot{\varepsilon}_1$ the increment of the axial strain.

A.2 Plastic parameters

There exists five plastic parameters for CJS-RE1 and eight plastic parameters for CJS-RE2. The identification of the plastic parameters must be done in a sequential way as shown in the following section.

A.2.1 Maximum tensile strength T_{rmax}

This parameter is associated to the apex of CJS-RE model. It is necessary to have at least two compression tests as indicated in Figure A.1 to identify $T_{\mathrm{r\,max}}$. Figure A.1 shows a triaxial stress path with a zero confining pressure ($p = 0$) and another one with a non-zero confining pressure ($p \neq 0$). Both are depicted in the S_{II} and I_1 stress space.

A.2.2 Dissymetry of the failure surface γ

Parameter γ which gives the intensity of the dissymmetry of the shear yield surface, the maximum volumetric contraction surface and the shear failure surface can be determined through a triaxial compression and extension test for a same confining pressure. Parameter γ can obtained by following expression:

$$\gamma = \frac{1 - F^6}{1 + F^6} \qquad \text{with} \qquad F = \frac{s^e_{II}(I^c_1 + 3T_{\mathrm{r\,max}})}{s^c_{II}(I^e_1 + 3T_{\mathrm{r\,max}})} \tag{A.3}$$

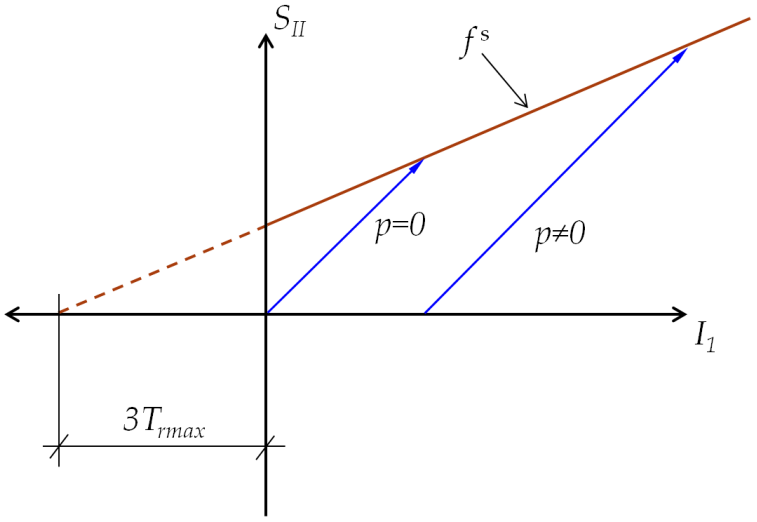

FIGURE A.1: Identification of $T_{\mathrm{r\,max}}$ by two compression triaxial tests

In Equation (A.3), $s_{II} = \sqrt{\frac{2}{3}}|\sigma_1 - \sigma_3|$ and $I_1 = \sigma_1 + 2\sigma_3$ for triaxial axissymmetric conditions. Superscripts c corresponds to a compression stress path and e to an extension stress path.

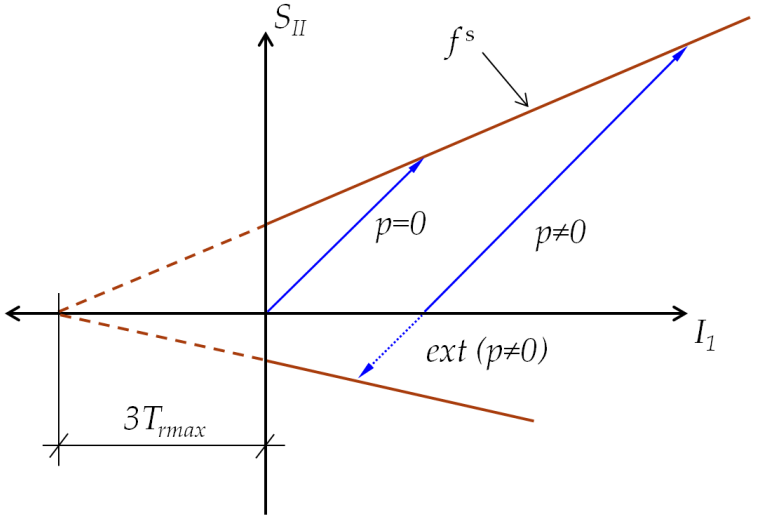

FIGURE A.2: Identification of γ by a triaxial compression and extension test or a same confining pressure

A.2.3 Failure radius R_{fail}

Once $T_{\mathrm{r\,max}}$ and the parameter dissymmetry (γ) determined, then the radius at failure (R_{fail}) can be obtained by using failure criteria in shearing as:

$$R_{\text{fail}} = \sqrt{\frac{2}{3}}\left(\frac{q^{\text{fail}}(1-\gamma)^{\frac{1}{6}}}{I_1^{\text{fail}} + 3T_{\text{r max}}}\right) \tag{A.4}$$

where q^{fail} is a deviatoric stress at failure and I_1^{fail} is the first invariant of stress tensor at failure. In the unconfined compression test $q^{\text{fail}} = f_c$ and $I_1^{\text{fail}} = f_c$.

A.2.4 Initial elastic radius R_{ini}

The determination of the initial radius of the shear yield surface that delimits the initial extent of the elastic deformations can be approximated from the state in the stress-strain curve when there is a loss of linearity between stress and deformation. However, in the case of rammed earth, this limit state occurs when the compression stress reaches approximately 25% - 30% of the compression resistance of the sample. Therefore, the value of R_{ini} is roughly equal to 25% - 30% of R_{fail}.

A.2.5 Radius of the maximum volumetric contraction R_{mvc}

This value can be identified as the maximum of the volumetric deformation when contractancy takes place. However, due to the less importance of this volumetric deformations in a quasi-brittle material, this parameter can be roughly estimate to 0.85.

A.2.6 Parameter of dilatancy β

The parameter of dilatancy included in the flow rule of the shear plastic mechanism can be determined from the volumetric deformation curve. In fact, most of dilatancy appears in the experiences is related to the opening of the larger cracks that cross the sample. Then, dilatancy is mainly related to structural deformations and not related to phenomena experienced by the material. However, we can consider that before failure dilatancy that may generated can be related to phenomena that take place uniformly in the sample due to the decohesion of grains and to micro-cracks.

Parameter β can be obtained from the state of stress at failure [Bag11]:

$$\dot{\boldsymbol{\varepsilon}}_v^{sp} = \beta\left(\frac{s_{II}^{\text{fail}}}{s_{II}^{\text{mvc}}} - 1\right)\frac{|\boldsymbol{s}\dot{\boldsymbol{e}}^{sp}|}{s_{II}} \tag{A.5}$$

By simplifying the terms $|\boldsymbol{se}^{\dot{sp}}|$ for triaxial condition we get:

$$|\boldsymbol{se}^{\dot{sp}}| = \frac{6}{9}(\sigma_1 - \sigma_3)(\dot{\varepsilon}_1 - \dot{\varepsilon}_3) \qquad \text{with} \qquad \dot{\varepsilon}_3 = \frac{\dot{\varepsilon}_v - \dot{\varepsilon}_1}{2} \tag{A.6}$$

and injecting equation (A.6) into equation (A.5) we have:

$$\beta\left(\frac{s_{II}^{fail}}{s_{II}^{mvc}} - 1\right)\sqrt{\frac{6}{9}} = \frac{2g_v}{3 - g_v} \qquad \text{with} \qquad g_v = \frac{\dot{\varepsilon}_v}{\dot{\varepsilon}_1} \tag{A.7}$$

with $s_{II}^{\text{fail}} = \sqrt{\frac{2}{3}}|\sigma_1^{\text{fail}} - \sigma_3^{\text{fail}}|$ and $s_{II}^{\text{mvc}} = \sqrt{\frac{2}{3}}|\sigma_1^{\text{mvc}} - \sigma_3^{\text{mvc}}|$.

Figure A.3 shows the effect of the variation of β on the compression behaviour. According to Figure A.3a, β has little effect on the stress strain response. On the other hand, as expected, it greatly influences the dilatancy rate in the volumetric deformation curve (Figure A.3b).

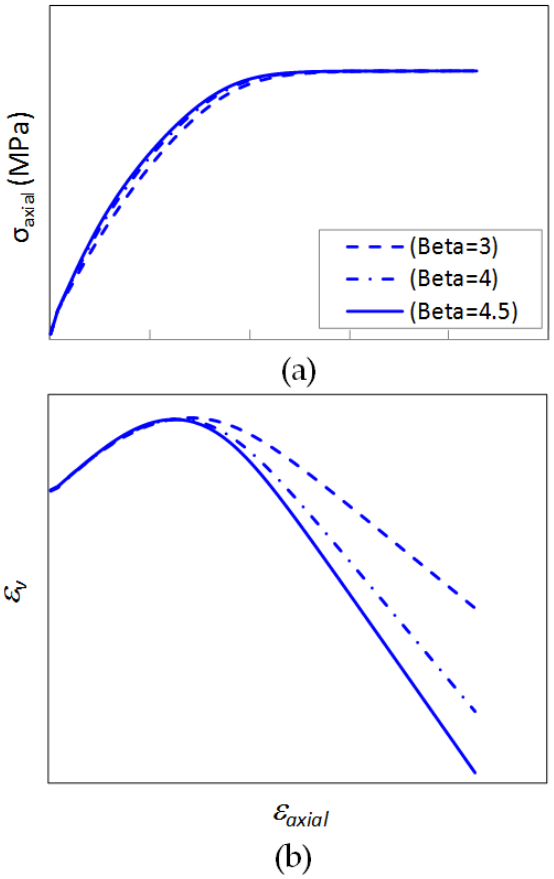

FIGURE A.3: Influence of the parameter of dilatancy β in the behaviour through the simulation of a compression test; (a): stress-strain, (b): volumetric deformation-strain

A.2.7 Isotropic hardening A

The parameter ruling the isotropic hardening (A) can be obtained by means of a trial-and-error method. This can be done by fitting the nonlinear part of the stress strain curve of a compression test prior it reaches failure. Figure A.4 shows the effect of parameter A on the stress-strain curve. Based on Figure A.4a, the larger A, the stiffer response will be obtained. Since it influences the stress strain response, it necessarily influences the volumetric deformation path through the flow rule of the shear mechanism (Figure A.4b).

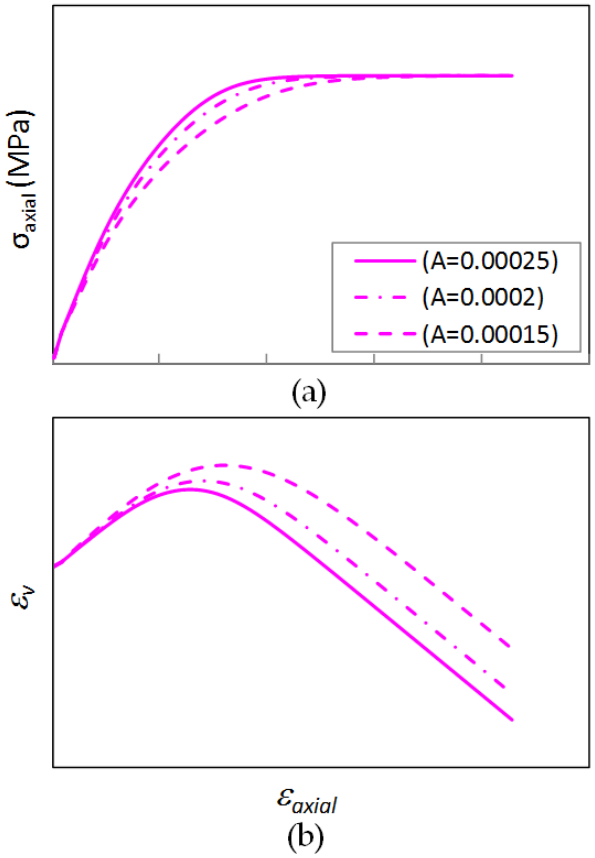

FIGURE A.4: Effect of the variation of isotropic hardening parameter A; (a): stress-strain, (b): volumetric deformation

A.2.8 Shear softening parameter α_s

α_s can be determined by a trial-and-error method on the basis of the softening part of the compression stress strain curve. Figure A.5 shows the influence of α_s on the stress-strain curve. After a parametric study, the acceptable value of α_s for unstabilised rammed earth ranges between -0.0001 to -0.0005.

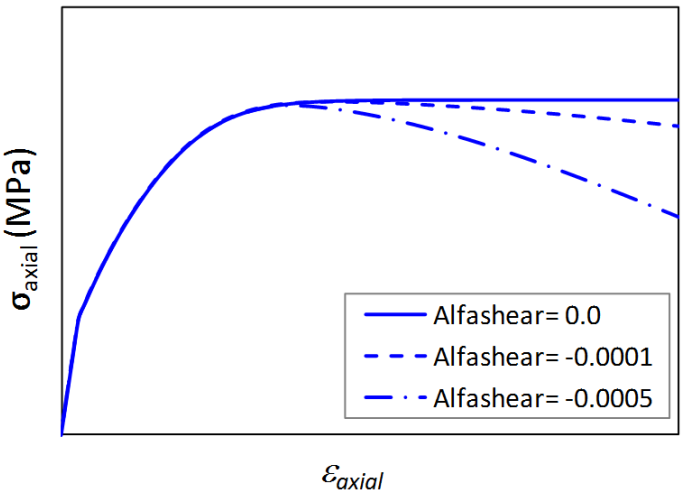

FIGURE A.5: Influence of the shear softening parameter α_s on the stress strain curve of a compression test

A.2.9 Tensile strength T_r

The tensile strength of earthen layer can be identified from a Brazilian test or uniaxial tensile test. If no tensile experiment is available, then the tensile strength of the rammed earth can be taken in the range of 5%-12.5% of the compression strength [AKS16].

A.2.10 Tensile softening parameter α_t

Tensile softening parameter α_t possible to be identified by using trial and error method from Brazilian test. α_t related with the descending part of the stress strain in Brazilian test.

Appendix B

Relationship between CJS-RE and Mohr-Coulomb model

Mohr Coulomb model which parameters may be easier to identify can help for the determination of some parameters of CJS-RE. Four CJS-RE parameters can be estimated with the help of Mohr-Coulomb model: T_{rmax}, γ, R_{fail}, and β.

B.1 MAT-1

Maximum tensile strength parameter (T_{rmax}) can be obtained by comparing the apex of the CJS-RE model and the Mohr Coulomb model as

$$T_{\text{rmax}} = \sqrt{3}(c)\cot(\phi) \tag{B.1}$$

where cohesion (c) is estimated based on the Plasticity Index (PI)[FH73] as

$$\frac{f_t}{c} = 0.34 + 0.01(PI) \tag{B.2}$$

Therefore, by setting the tensile strength in the range of $5\%f_c$-$12.5\%f_c$ [AKS16] and given the Plasticity Index from the experiments references (PI=0.7), we will get acceptable cohesion between 182 - 454kPa. Finally, the value of C = 318kPa was taken according to the average value of the acceptable cohesion. By using this value, we get T_{rmax} equal to 730kPa.

Parameter of dissymmetry γ can be estimated by comparing the ratio of the radius at failure in the tensile and compression meridian (R_t/R_c) between the

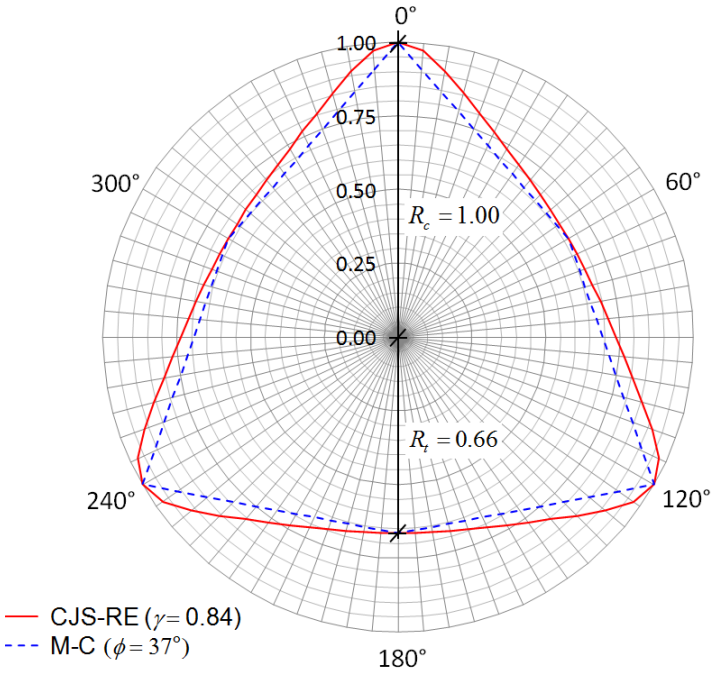

FIGURE B.1: Shape of the Mohr Coulomb model ($\phi = 37°$) and CJS-RE model ($\gamma = 0.84$) in the deviatoric plane

model (Equation (B.3)). This method however is only an approximation based on the comparison between the radius at the corner state. Thus, it will produce a surface of failure that coincides with the six corner points of Mohr-Coulomb model. For example, Figure B.1 shows a comparison between the shape of the Mohr-Coulomb model with $\phi = 37°$ and the corresponding shear failure surface of CJS-RE model ($\gamma = 0.84$). It can be seen that the shape of the CJS-RE model gives more convexity than Mohr-Coulomb model. This convexity assures a stable material behaviour according to the postulate of Drucker [Dru57].

$$\begin{aligned} \left(\frac{R_t}{R_c}\right)^{\text{CJS-RE}} &= \left(\frac{1-\gamma}{1+\gamma}\right)^{\frac{1}{6}} \\ \left(\frac{R_t}{R_c}\right)^{\text{MC}} &= \frac{(3-\sin\phi)}{(3+\sin\phi)} \end{aligned} \tag{B.3}$$

Radius at failure can be deduced by comparing the shear failure surface of CJS-RE model and Mohr-Coulomb model. Mohr-Coulomb criterion is written as:

$$\sigma_1 = \sigma_3(N_\phi) - 2c\sqrt{N_\phi} \qquad \text{with} \qquad N_\phi = \frac{(1+\sin\phi)}{(1-\sin\phi)} \tag{B.4}$$

By using the shear failure criterion from CJS-RE model (Equation (3.4)) for R_{fail}, assuming $s_{II} = \sqrt{\frac{2}{3}}|\sigma_1 - \sigma_3|$, $I_1 = \sigma_1 + 2\sigma_3$ (triaxial axissymmetry condition), and injecting Equation (B.1) and (B.4) in R_{fail} relationship we obtain

$$R_{\text{fail}} = \sqrt{\frac{2}{3}}\left(\frac{(\sigma_3(N_\phi - 1) - 2c\sqrt{N_\phi})(1-\gamma)^{\frac{1}{6}}}{\sigma_3(N_\phi + 2) - 2c\sqrt{N_\phi} + 3\sqrt{3}(c)\cot(\phi)}\right) \tag{B.5}$$

We can also directly obtained R_{fail} by using T_{rmax} and γ that was already identified as:

$$R_{\text{fail}} = \sqrt{\frac{2}{3}}\left(\frac{q^{fail}(1-\gamma)^{\frac{1}{6}}}{I_1^{fail} + 3T_{\text{rmax}}}\right) \tag{B.6}$$

where q^{fail} the deviatoric stress at failure and I_1^{fail} the first invariant of stress tensor. In an unconfined compression test, $q = \sigma_1 = f_c$ and $I_1 = \sigma_1 = f_c$.

.

Parameter of dilatancy β can be correlated with the dilatancy angle (ψ) according to [Pur06] as

$$\beta = \frac{2\sqrt{6}\sin\psi}{(r-1)(3-\sin\psi)} \qquad \text{with} \qquad r = \frac{R_{\text{fail}}}{R_{\text{mvc}}} \tag{B.7}$$

According to our definition that the Maximum Volumetric Contraction (MVC) state reaches when $R_{\text{mvc}} = 0.85R_{\text{fail}}$, then we have r = 1.18. By taking the dilatancy angle (ψ) between 0° and 20° whether dealing with soils, concrete, or rocks [VDB84] then we will get acceptable β value around 0.0 - 3.5. However, the dilatancy angle did not play an important role in the behavior of rammed earth walls [BBLM16].

B.2 MAT-2

Experiments reference are taken from [EN17]. Elastic modulus (E) is taken from the average of the three compression test (on cylinder) which is equal to 760 MPa. Poisson ratio is taken to be equal to 0.25.

The plastic parameters are estimated from known cohesion (C) which is around 135 - 260 kPa, ϕ between $44° - 45°$ (small shear box tests [EN17]), and average compression strength on tested rammed earth cylinder of 2.0 MPa[EN17].

Maximum tensile strength parameter (T_{rmax}) can be obtained by comparing the apex of the CJS-RE model and the Mohr Coulomb model as

$$T_{\text{rmax}} = \sqrt{3}(c)\cot(\phi) \tag{B.8}$$

where cohesion (c) is obtained from experiments of direct shear tests which is around 135 - 260 kPa. Using this ranges of value then T_{rmax} will fall between 233 and 450 kPa for $\phi = 45°$. Finally, the average value of T_{rmax} of 350 kPa is taken.

Parameter of dissymmetry (γ) is stated considering the maximum convexity of shear criterion to be equal to 0.85.

Radius at failure calculated from the known value of T_{rmax} and γ using equation (B.6), where $q^{\text{fail}} = \sigma_1 = f_c$ and $I_1^{\text{fail}} = \sigma_1 = f_c$. According to the average of compression strength on cylinder of tested rammed earth of 2 MPa, then R_{fail} is equal to 0.39.

Parameter of dilatancy (β) is taken as 1.0 considering that the density of MAT-2 is lower than MAT-1. Nevertheless, dilatancy did not play a role in rammed earth wall. Note that dilatancy in rammed earth is mainly related with structural increases of volume due to opening of cracks and not related to the material itself.

Appendix C

A parametric study for compression-extension tests

In order to give some trends for the behavior of rammed earth through CJS-RE, some simulations of a compression and extension path are performed. The model for the triaxial test is shown in Figure C.1 where the earth sample is represented by a brick element. The compression stress path test shown in Figure C.1a. In this test, a confining pressure is first applied laterally in the direction y+ and x-, before a deviatoric stress compresses the specimen vertically. A similar method is used for extension tests (Figure C.1b), but with a vertical stress that tends to decrease.

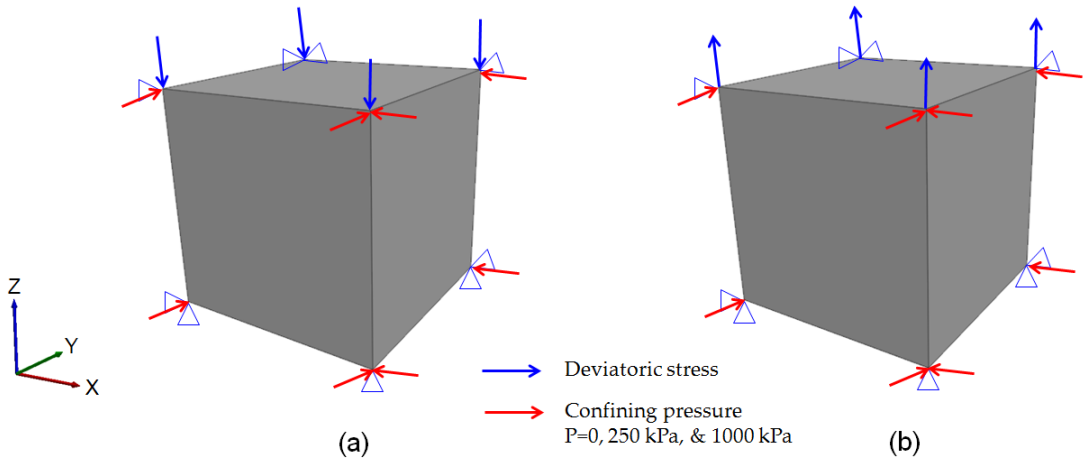

FIGURE C.1: Model of the compression and extension tests

C.1 CJS-RE1

Two simulations with CJS-RE1 for a compression stress path with two different confining pressures (p=250kPa and p=1MPa in Figure C.3) were performed and the result is given in Figure C.2. As expected, the maximum resistance increases as the confining pressure increases. In general, CJS-RE1 gives a large domain of elasticity which is the drawback of this model. This gives a stiff response along the compression stress path. Nevertheless, this model is sufficient for the prediction of the limit load of quasi brittle materials in compression.

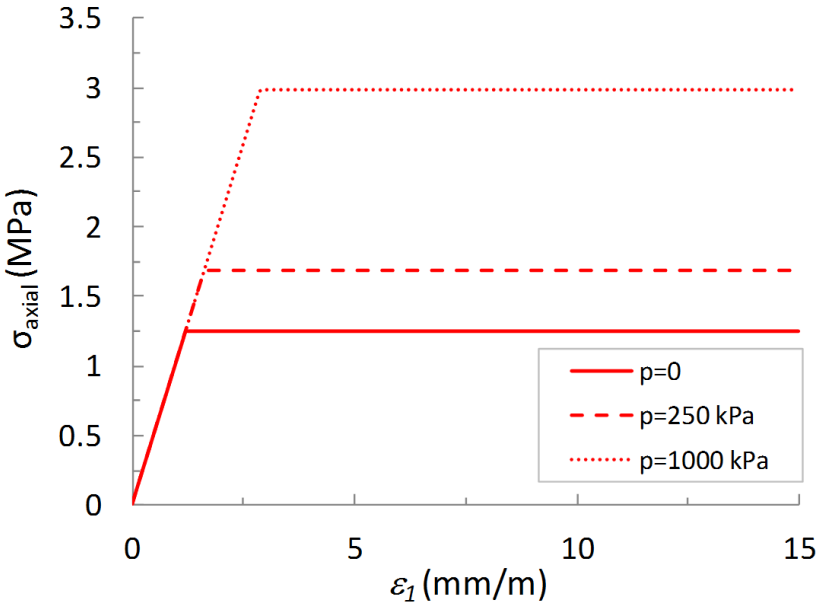

FIGURE C.2: Response along a compression stress path for CJS-RE1 model

Then, the results for an extension loading path are depicted in Figure C.4. In the extension tests, the stress path can either lead to a tensile failure or a shear failure depending on the confining pressure. For the case of zero confining pressure, the tensile resistance reaches the peak at 0.1MPa (T_r) and then a softening towards zero is activated. In the case of a confining pressure of 250kPa, the tensile failure reaches at higher level of stress (0.35MPa) and then it drops until the residual stress state associated with to the confining stress. With a confining pressure of 1MPa, the extension path leads the system to fail in shearing without any softening (Figure C.3 and Figure C.4).

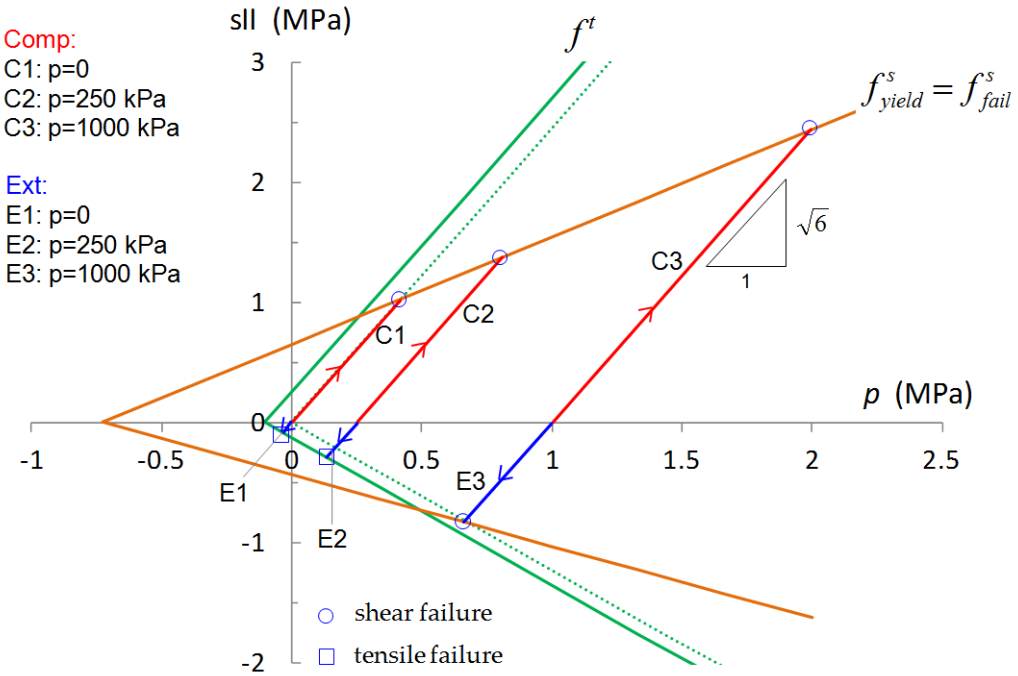

FIGURE C.3: Triaxial stress path in the meridian $s_{II} - p$ plane for CJS-RE1 model

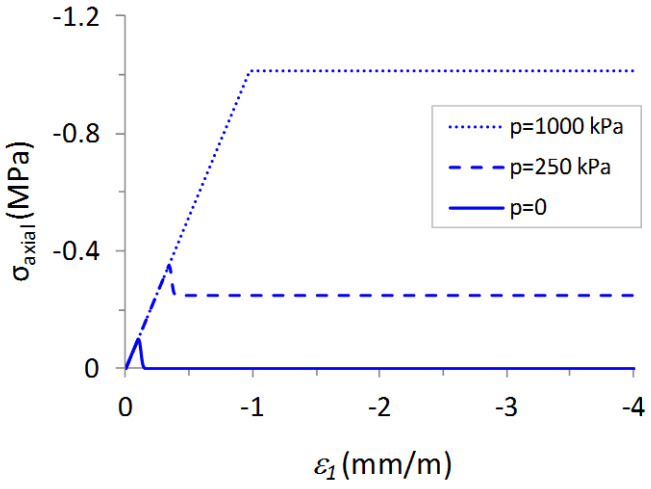

FIGURE C.4: Responses in the extension stress path for CJS-RE1 model

C.2 CJS-RE2

As in the first level of the model, a simulation along a compression and an extension stress path is performed. The same geometrical model and loading condition are used as depicted in Figure C.1. Figure C.5 gives the results for the compression stress path, whereas Figure C.6 shows the results for the extension loading path.

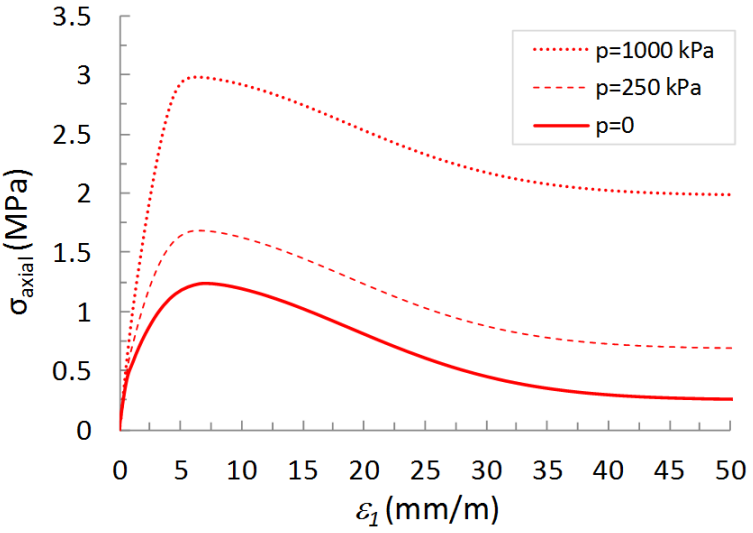

FIGURE C.5: Response along a compression stress path for CJS-RE2 model

As expected, the second level of the model induces a non linear behavior earlier when loading than CJS-RE1 does which is more consistent with experiment evidence. It is also seen that confining pressure gives an influence on the global stiffness of the system and also on the maximum resistance. All the three systems fail by shearing as for CJS-RE1 but with a lower residual stress due to the shear softening.

Along the extension loading path, a different stress-strain pattern can be observed for each loading condition. For unconfined tensile test (p=0), the system reaches a tensile failure at the level of 0.1MPa before it drops to zero strength. In the case of an extension test with a confining pressure of p=250kPa, the system exhibits a certain hardening before reaching a tensile failure at the level of 0.35MPa before it softens (tensile softening) and stabilizes. Finally, for a higher confining pressure (p=1MPa), the element fails in shearing at a level of 1MPa before softening (shear softening).

The corresponding triaxial stress path in the meridian plane can be seen in Figure C.7. The distinguished feature compared to CJS-RE1 is that the final points of

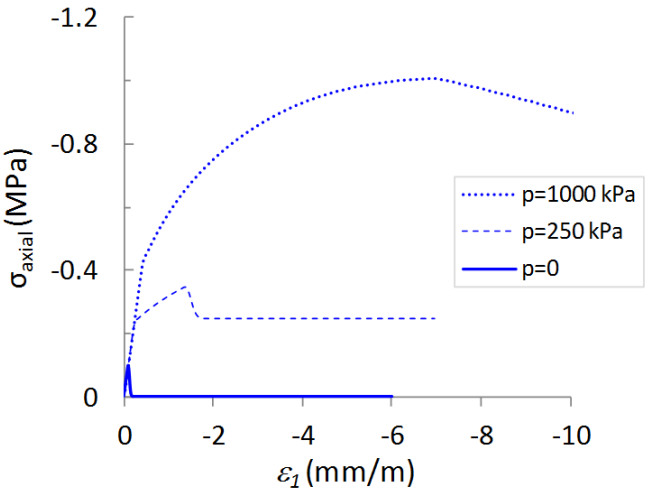

FIGURE C.6: Response along an extension stress path for CJS-RE2 model

shear failure (C1, C2, C3, and E3) are not at the intersection of the stress path and of the shear failure surface (f^s_{fail}), but on the crossing between the stress path and the residual shear failure surface (f^s_{res}) which represents the final state after the shear softening process.

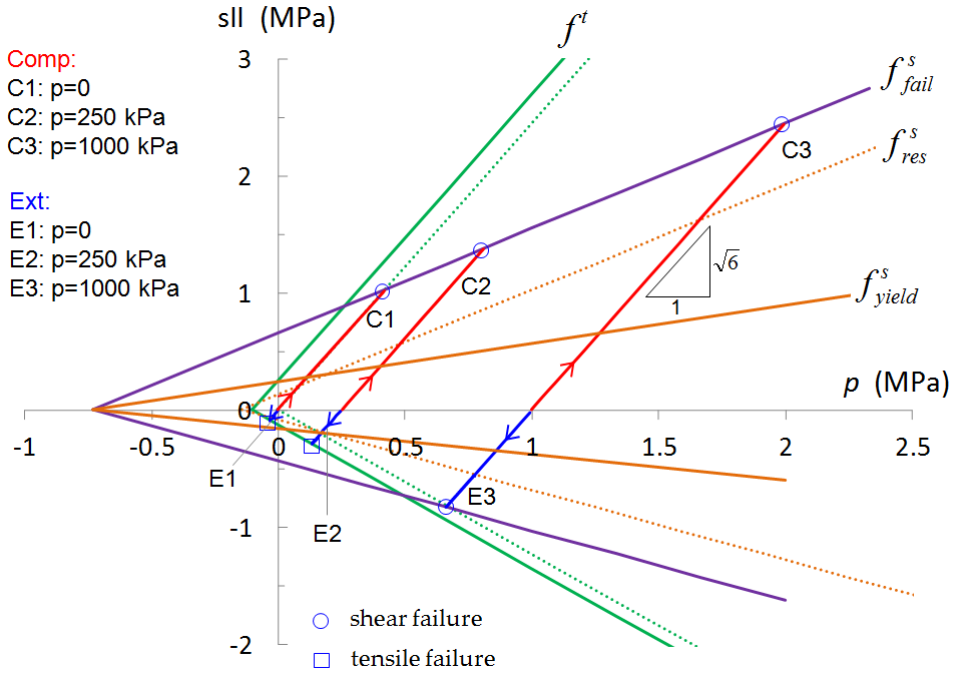

FIGURE C.7: Triaxial stress path with CJS-RE2 model

Appendix D

Mesh sensitivity

D.1 Mesh sensitivity

A too refine mesh can be time consuming process if it involves a complex geometrical model. To get an acceptable numerical result with optimum time, a mesh sensitivity study is taken. In this work, the mesh study is carried out by performing different diagonal compression tests for different refining for the meshing: 20x20x10, 30x30x15, and 40x40x20 in the wall (Figures D.1). For the sake of simplicity, CJS-RE1 is used for the simulation.

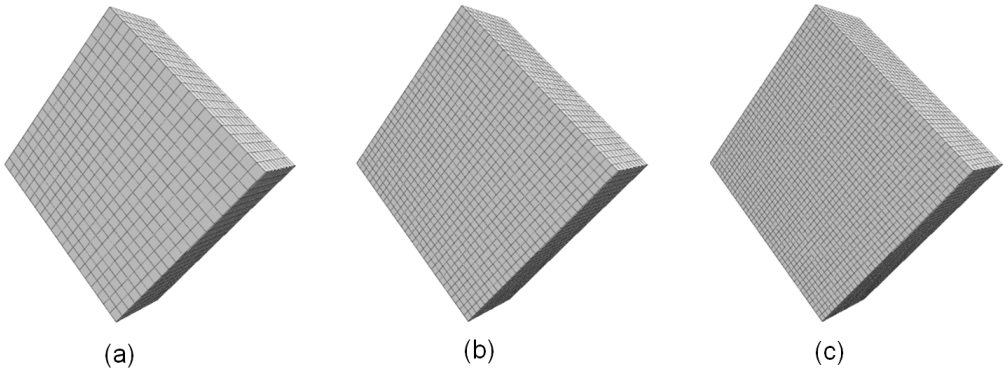

FIGURE D.1: 3D numerical model of a diagonal compression test with three different mesh sizes; a: 20x20x10, b: 30x30x15, c: 40x40x20

Figures D.2 give the strain stress curve of a simulation of a diagonal compression test with three different mesh sizes. Until the shear strain of 0.05%, the model with the mesh size of 20x20 gives the largest first peak response following by the mesh 30x30 and the mesh 40x40. However, the difference is unsignificant. This difference is a little bit more significant when the tensile softening is triggered

though acceptable. Therefore, considering the quality of results and the computation time, the minimum 30x30 mesh will be generally used to address boundary value problems such that of a diagonal compression test with a wallet size similar to the one that was simulated herein.

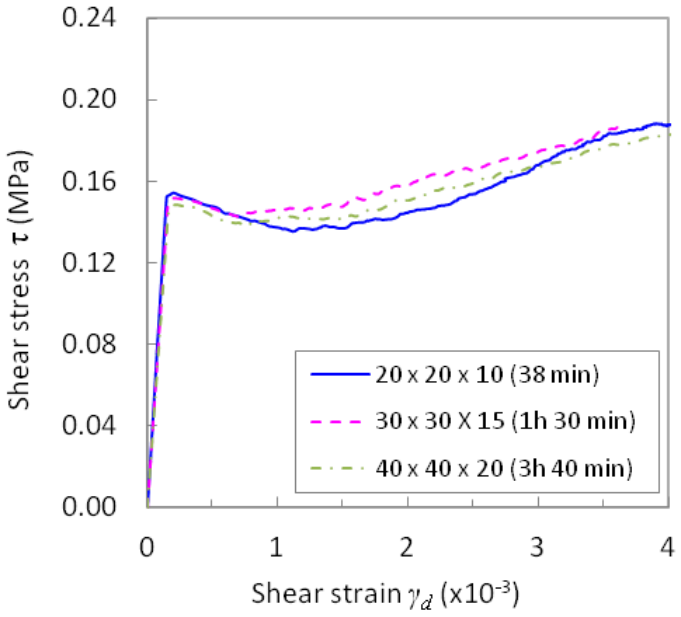

FIGURE D.2: Stress-train response in a simulated diagonal compression test with different mesh sizes (CJS-RE1)

Appendix E

Computational procedure

In CJS-RE model, the shearing failure criterion (f_t) is written with the stress invariants (s_{II} and I_1) which does not require the computation of the principal stresses, whereas the tensile failure criterion (f_t) involves the minor principal stress σ_3. This difference of the reference coordinates needs to be handle in the computation. For the sake of simplicity, all of the stress states were defined in the principal axes of stress which will be identified when plasticity is generated. The general computation procedure of the constitutive model is given in the form of flowchart shown in Figure E.1 with some part of important step explained in the following section.

E.1 Calculation of the principal stresses

Principal stresses for three dimensional problem case can be calculated by using following formula:

$$\begin{aligned} \sigma_1 &= \frac{I_1}{3} + \frac{2}{3}\left(\sqrt{I_1^2 - 3I_2}\right)\cos\phi \\ \sigma_2 &= \frac{I_1}{3} + \frac{2}{3}\left(\sqrt{I_1^2 - 3I_2}\right)\cos\left(\phi - \frac{2\pi}{3}\right) \\ \sigma_3 &= \frac{I_1}{3} + \frac{2}{3}\left(\sqrt{I_1^2 - 3I_2}\right)\cos\left(\phi - \frac{4\pi}{3}\right) \end{aligned} \tag{E.1}$$

where

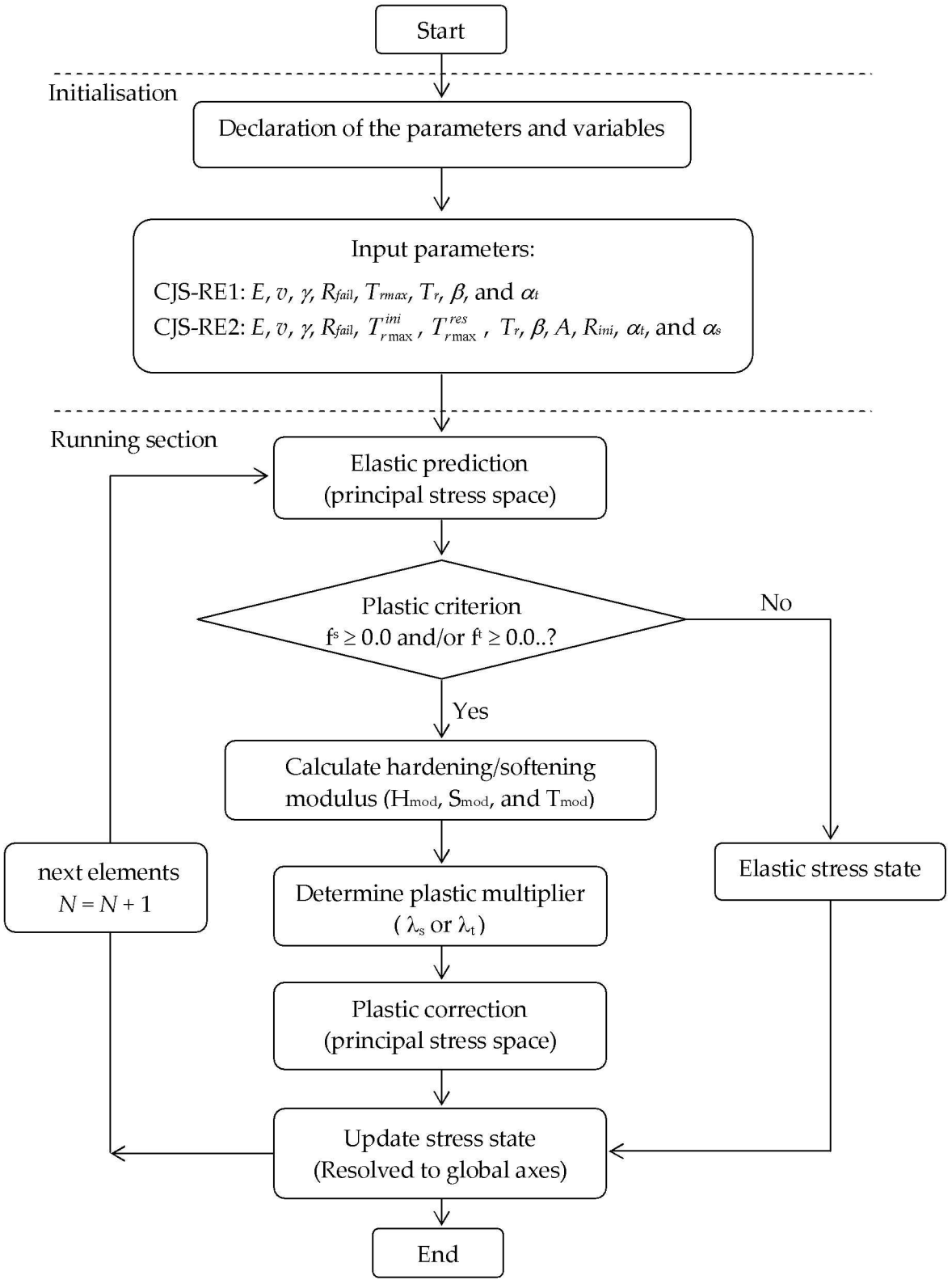

FIGURE E.1: Flowchart implementation of the constitutive model

$$\begin{aligned}
\phi &= \frac{1}{3} cos^{-1}\left(\frac{2I_1^3 - 9I_1I_2 + 27I_3}{2(I_1^2 - 3I_2)^{3/2}}\right) \\
I_1 &= \sigma_{11} + \sigma_{22} + \sigma_{33} = \mathrm{tr}(\sigma) \\
I_2 &= \sigma_{11}\sigma_{22} + \sigma_{22}\sigma_{33} + \sigma_{33}\sigma_{11} - \sigma_{12}^2 - \sigma_{23}^2 - \sigma_{13}^2 \\
I_3 &= \sigma_{11}\sigma_{22}\sigma_{33} - \sigma_{11}\sigma_{23}^2 - \sigma_{22}\sigma_{13}^2 - \sigma_{33}\sigma_{12}^2 + 2\sigma_{12}\sigma_{13}\sigma_{23} = \det(\sigma)
\end{aligned} \tag{E.2}$$

Minor principal stresses σ_3 is determined by using some conditional as follows:

$$\begin{aligned}
&\text{if } \sigma_{33} > \sigma_1 \quad \text{then} \quad \sigma_{33} = \sigma_1 \implies \text{(major principal stress)} \\
&\text{if } \sigma_{33} < \sigma_3 \quad \text{then} \quad \sigma_{33} = \sigma_3 \implies \text{(minor principal stress)} \\
&\text{else} \quad \text{then} \quad \sigma_{33} = \sigma_2 \implies \text{(intermediate principal stress)}
\end{aligned} \tag{E.3}$$

E.2 Calculation of hardening and softening modulus

The movement of the yield or failure surface is controlled by the hardening/softening modulus. The determination of the hardening/softening modulus can be obtained by using the consistency relationship.

E.2.1 Hardening modulus (H_{mod})

Consistency equation in the hardening process can be written as

$$\dot{f}^s = \frac{\partial f^s}{\partial \boldsymbol{\sigma}} \dot{\boldsymbol{\sigma}} + \frac{\partial f^s}{\partial R} \dot{R} = 0 \tag{E.4}$$

Failure criteria is written as

$$f^s(\boldsymbol{\sigma}, R) = q_{II} h(\theta_q) - R(I_1 + 3T_{\mathrm{r\,max}}) \leq 0 \tag{E.5}$$

and the increments of the yield radius given as

$$\dot{R} = A(R_{\mathrm{fail}} - R_{\mathrm{ini}}) \mathrm{exp}(-Ap)\dot{p} \tag{E.6}$$

The increment of hardening of variable $\dot{p}$ is given by the normality relationship:

$$\dot{p} = -\dot{\lambda}_s \frac{\partial f^s}{\partial R} = \dot{\lambda}_s (I_1 + 3T_{\mathrm{r\,max}}) \tag{E.7}$$

So from (E.4),(E.6) and (E.7) we get

$$\frac{\partial f^s}{\partial \boldsymbol{\sigma}} \dot{\boldsymbol{\sigma}} = -\frac{\partial f^s}{\partial R} \dot{R} \tag{E.8}$$

$$\frac{\partial f^s}{\partial \boldsymbol{\sigma}} \dot{\boldsymbol{\sigma}} = \dot{\lambda}_s A (I_1 + 3T_{\mathrm{r\,max}})^2 (R_{\mathrm{fail}} - R_{\mathrm{ini}}) \exp(-Ap) \tag{E.9}$$

with

$$H_{\mathrm{mod}} = A (I_1 + 3T_{\mathrm{r\,max}})^2 (R_{\mathrm{fail}} - R_{\mathrm{ini}}) \exp(-Ap) \tag{E.10}$$

E.2.2 Shear softening modulus (S_{mod})

Consistency equation in the shear softening process can be written as

$$\dot{f}^s = \frac{\partial f^s}{\partial \boldsymbol{\sigma}} \dot{\boldsymbol{\sigma}} + \frac{\partial f^s}{\partial T_{\mathrm{r\,max}}} \dot{T}_{\mathrm{r\,max}} = 0 \tag{E.11}$$

Degradation of $T_{\mathrm{r\,max}}$ is written as an exponential function as

$$T_{\mathrm{r\,max}} = (T^{\mathrm{ini}}_{\mathrm{r\,max}} - T^{\mathrm{res}}_{\mathrm{r\,max}}) \exp(\alpha_s \varepsilon^p_{\mathrm{diff}}) + T^{\mathrm{res}}_{\mathrm{r\,max}} \tag{E.12}$$

Because the shear softening defined as a function of plastic shear deformation then we get the derivation with plastic shear deformation as follows

$$\frac{\dot{T}_{\mathrm{r\,max}}}{\dot{\varepsilon}^p_s} = \alpha_s (T^{\mathrm{ini}}_{\mathrm{r\,max}} - T^{\mathrm{res}}_{\mathrm{r\,max}}) \exp(\alpha_s \varepsilon^p_{\mathrm{diff}}) \tag{E.13}$$

with

$$\dot{\varepsilon}^p_s = \dot{\lambda}_s \left\| \frac{\partial \boldsymbol{g}^s}{\partial \boldsymbol{\sigma}} \right\| \tag{E.14}$$

and

$$\varepsilon_{\text{diff}}^{sp} = \|\boldsymbol{\varepsilon}^{sp} - \boldsymbol{\varepsilon}_s^{\text{p fail}}\| \tag{E.15}$$

$$\frac{\partial f^s}{\partial T_{\text{r max}}} = -3R \tag{E.16}$$

So from (E.11),(E.13) and (E.16) we get

$$\dot{f}^s = \frac{\partial f^s}{\partial \boldsymbol{\sigma}}\dot{\boldsymbol{\sigma}} = -\frac{\partial f_s}{\partial T_{\text{r max}}}\dot{T}_{\text{r max}} \tag{E.17}$$

$$\dot{f}^s = \frac{\partial f^s}{\partial \boldsymbol{\sigma}}\dot{\boldsymbol{\sigma}} = \dot{\lambda}_s\left(\alpha_s(3R)(T_{\text{r max}}^{\text{ini}} - T_{\text{r max}}^{\text{res}})\exp(\alpha_s\varepsilon_{\text{diff}}^p)\left\|\frac{\partial \boldsymbol{g}^s}{\partial \boldsymbol{\sigma}}\right\|\right) \tag{E.18}$$

with

$$S_{\text{mod}} = \alpha_s(3R)(T_{\text{r max}}^{\text{ini}} - T_{\text{r max}}^{\text{res}})\exp(\alpha_s\varepsilon_{\text{diff}}^p)\left\|\frac{\partial \boldsymbol{g}^s}{\partial \boldsymbol{\sigma}}\right\| \tag{E.19}$$

E.2.3 Tensile softening modulus (T_{mod})

The expression of the consistency equation for the tensile failure can be written as follows:

$$\dot{f}^t = \frac{\partial f^t}{\partial \boldsymbol{\sigma}}\dot{\boldsymbol{\sigma}} + \frac{\partial f_t}{\partial T_r}\dot{T}_r = 0 \tag{E.20}$$

with

$$\frac{\partial f^t}{\partial T_r} = -1 \tag{E.21}$$

Degradation of T_r is made as a function of plastic tensile strain and described by using exponential function as follows

$$T_r = T_r^{\text{ini}}\exp(\alpha_t\int \dot{\varepsilon}^{tp}dt) \tag{E.22}$$

The derivation of (E.22) with respect of plastic tensile deformation gives

$$\frac{\dot{T}_r}{\dot{\varepsilon}_t^p} = \alpha_t T_r^{\text{ini}}\exp(\alpha_t\int \dot{\varepsilon}^{tp}dt) \tag{E.23}$$

with

$$\dot{\varepsilon}_t^p = \dot{\lambda}_t \frac{\partial \boldsymbol{g}^t}{\partial \sigma_3} = \dot{\lambda}_t \tag{E.24}$$

Combining equation (E.23) and also equation (E.21) into consistency equation gives:

$$\frac{\partial f^t}{\partial \boldsymbol{\sigma}} \dot{\boldsymbol{\sigma}} = -\frac{\partial f^t}{\partial T_r} \dot{T}_r \tag{E.25}$$

$$\frac{\partial f^t}{\partial \boldsymbol{\sigma}} \dot{\boldsymbol{\sigma}} = \dot{\lambda}_t \left(\alpha_t T_r^{\text{ini}} \exp(\alpha_t \int \dot{\varepsilon}^{tp} dt) \right) \tag{E.26}$$

$$\dot{\lambda}_t = \frac{1}{T_{\text{mod}}} \left(\frac{\partial f^t}{\partial \boldsymbol{\sigma}} \dot{\boldsymbol{\sigma}} \right) \tag{E.27}$$

Where T_{mod} is a plastic tensile modulus expressed as

$$T_{\text{mod}} = (\alpha_t T_r^{\text{ini}}) \exp(\alpha_t \int \dot{\varepsilon}^{tp} dt) \tag{E.28}$$

E.3 Determination of plastic multiplier

The plastic strain increment is defined by a derivation of the plastic potential ∂g with respect to the stress tensor:

$$\dot{\varepsilon}^p = \dot{\lambda} \frac{\partial g}{\partial \boldsymbol{\sigma}} \tag{E.29}$$

Using the hardening/softening rules and the consistency condition in Equation (E.29), we obtain the following expression for the plastic strain increment [NM07]:

$$\dot{\varepsilon}^p = \frac{(\partial f / \partial \sigma) \dot{\sigma}}{H} \left(\frac{\partial g}{\partial \sigma} \right) \tag{E.30}$$

At the moment when the stress state passes away the failure criterion (explicit scheme), then it is necessary to perform a stress correction. It can be done by substracting to the current stress state the plastic correction part as follows:

$$\begin{aligned} f^s(\sigma - \dot{\sigma}) &= f^s(\sigma) - \frac{\partial f^s}{\partial \sigma}\dot{\sigma} \\ f^t(\sigma - \dot{\sigma}) &= f^t(\sigma) - \frac{\partial f^t}{\partial \sigma}\dot{\sigma} \end{aligned} \tag{E.31}$$

The elastic stress increment can be written as

$$\dot{\sigma} = \underset{=}{C}(\dot{\varepsilon}^{total} - \dot{\varepsilon}^{p}) \tag{E.32}$$

where $\underset{=}{C}$ is an elastic stiffness tensor for the three dimensional case. By expanding the increments of plastic strain in Equation (E.32) as a summation of the flow rule of the shearing and of the tensile plastic deformation, we obtain

$$\dot{\sigma} = \underset{=}{C}\left(\dot{\varepsilon}^{total} - \dot{\lambda}_s\frac{\partial g^s}{\partial \sigma} - \dot{\lambda}_t\frac{\partial g^t}{\partial \sigma}\right) \tag{E.33}$$

The variables $\dot{\lambda}_s$ and $\dot{\lambda}_t$ may now be defined by requiring that the new stress point must be located on the yield or failure surface. This implies that the left terms in Equation (E.31) must equal to zero. By multiplying the Equation (E.33) with $(\partial f^s/\partial\sigma)$ for shearing and $(\partial f^t/\partial\sigma)$ for tensile and replace $(\partial f/\partial\sigma)\dot{\sigma}$ with $\dot{\lambda}_s H$ where H is a hardening/softening modulus. Then we have:

$$\begin{aligned} \dot{\lambda}_s(H_{mod} + S_{mod}) &= \underset{=}{C}\frac{\partial f_s}{\partial \sigma}\left(\dot{\varepsilon}^{total} - \dot{\lambda}_s\frac{\partial g^s}{\partial \sigma} - \dot{\lambda}_t\frac{\partial g^t}{\partial \sigma}\right) \\ \dot{\lambda}_t T_{mod} &= \underset{=}{C}\frac{\partial f_t}{\partial \sigma}\left(\dot{\varepsilon}^{total} - \dot{\lambda}_s\frac{\partial g^s}{\partial \sigma} - \dot{\lambda}_t\frac{\partial g^t}{\partial \sigma}\right) \end{aligned} \tag{E.34}$$

by arrangements we have

$$\begin{aligned} \dot{\lambda}_s\left(H_{mod} + S_{mod} + \underset{=}{C}\frac{\partial f_s}{\partial \sigma}\frac{\partial g^s}{\partial \sigma}\right) + \dot{\lambda}_t\left(\underset{=}{C}\frac{\partial f_s}{\partial \sigma}\frac{\partial g^t}{\partial \sigma}\right) &= \underset{=}{C}\frac{\partial f_s}{\partial \sigma}\dot{\varepsilon}^{total} \\ \dot{\lambda}_s\left(\underset{=}{C}\frac{\partial f_t}{\partial \sigma}\frac{\partial g^s}{\partial \sigma}\right) + \dot{\lambda}_t\left(T_{mod} + \underset{=}{C}\frac{\partial f_t}{\partial \sigma}\frac{\partial g^t}{\partial \sigma}\right) &= \underset{=}{C}\frac{\partial f_t}{\partial \sigma}\dot{\varepsilon}^{total} \end{aligned} \tag{E.35}$$

Suppose that

$$\begin{aligned}
\left(H_{mod} + S_{mod} + \underset{=}{C}\frac{\partial f_s}{\partial \sigma}\frac{\partial g^s}{\partial \sigma}\right) &= A \\
\left(\underset{=}{C}\frac{\partial f_s}{\partial \sigma}\frac{\partial g^t}{\partial \sigma}\right) &= B \\
\left(\underset{=}{C}\frac{\partial f_t}{\partial \sigma}\frac{\partial g^s}{\partial \sigma}\right) &= C \\
\left(T_{mod} + \underset{=}{C}\frac{\partial f_t}{\partial \sigma}\frac{\partial g^t}{\partial \sigma}\right) &= D \\
\underset{=}{C}\frac{\partial f_s}{\partial \sigma}\dot{\varepsilon}^{total} &= f_s(\sigma) \\
\underset{=}{C}\frac{\partial f_t}{\partial \sigma}\dot{\varepsilon}^{total} &= f_t(\sigma)
\end{aligned} \tag{E.36}$$

where $\underset{=}{C}$ is an elastic stiffness matrix (Hooke's law) and note that A,B,C, and D are scalar quantity which can be obtained from

$$\mathrm{A} = \mathrm{H}_{\mathrm{mod}} + S_{\mathrm{mod}} + \begin{bmatrix} \alpha_1 & \alpha_2 & \alpha_2 & 0 & 0 & 0 \\ \alpha_2 & \alpha_1 & \alpha_2 & 0 & 0 & 0 \\ \alpha_2 & \alpha_2 & \alpha_1 & 0 & 0 & 0 \\ 0 & 0 & 0 & 2G & 0 & 0 \\ 0 & 0 & 0 & 0 & 2G & 0 \\ 0 & 0 & 0 & 0 & 0 & 2G \end{bmatrix} \begin{bmatrix} \partial g_{s11}/\partial \sigma_{11} \\ \partial g_{s22}/\partial \sigma_{22} \\ \partial g_{s33}/\partial \sigma_{33} \\ \partial g_{s12}/\partial \sigma_{12} \\ \partial g_{s13}/\partial \sigma_{13} \\ \partial g_{s23}/\partial \sigma_{23} \end{bmatrix} \begin{bmatrix} \partial f_{s11}/\partial \sigma_{11} \\ \partial f_{s22}/\partial \sigma_{22} \\ \partial f_{s33}/\partial \sigma_{33} \\ \partial f_{s12}/\partial \sigma_{12} \\ \partial f_{s13}/\partial \sigma_{13} \\ \partial f_{s23}/\partial \sigma_{23} \end{bmatrix} \tag{E.37}$$

$$B = \begin{bmatrix} \alpha_1 & \alpha_2 & \alpha_2 & 0 & 0 & 0 \\ \alpha_2 & \alpha_1 & \alpha_2 & 0 & 0 & 0 \\ \alpha_2 & \alpha_2 & \alpha_1 & 0 & 0 & 0 \\ 0 & 0 & 0 & 2G & 0 & 0 \\ 0 & 0 & 0 & 0 & 2G & 0 \\ 0 & 0 & 0 & 0 & 0 & 2G \end{bmatrix} \begin{bmatrix} \partial g_{t11}/\partial \sigma_{11} = 0.0 \\ \partial g_{t22}/\partial \sigma_{22} = 0.0 \\ \partial g_{t33}/\partial \sigma_{33} = 1.0 \\ \partial g_{t12}/\partial \sigma_{12} = 0.0 \\ \partial g_{t13}/\partial \sigma_{13} = 0.0 \\ \partial g_{t23}/\partial \sigma_{23} = 0.0 \end{bmatrix} \begin{bmatrix} \partial f_{s11}/\partial \sigma_{11} \\ \partial f_{s22}/\partial \sigma_{22} \\ \partial f_{s33}/\partial \sigma_{33} \\ \partial f_{s12}/\partial \sigma_{12} \\ \partial f_{s13}/\partial \sigma_{13} \\ \partial f_{s23}/\partial \sigma_{23} \end{bmatrix} \tag{E.38}$$

$$C = \begin{bmatrix} \alpha_1 & \alpha_2 & \alpha_2 & 0 & 0 & 0 \\ \alpha_2 & \alpha_1 & \alpha_2 & 0 & 0 & 0 \\ \alpha_2 & \alpha_2 & \alpha_1 & 0 & 0 & 0 \\ 0 & 0 & 0 & 2G & 0 & 0 \\ 0 & 0 & 0 & 0 & 2G & 0 \\ 0 & 0 & 0 & 0 & 0 & 2G \end{bmatrix} \begin{bmatrix} \partial g_{s11}/\partial\sigma_{11} \\ \partial g_{s22}/\partial\sigma_{22} \\ \partial g_{s33}/\partial\sigma_{33} \\ \partial g_{s12}/\partial\sigma_{12} \\ \partial g_{s13}/\partial\sigma_{13} \\ \partial g_{s23}/\partial\sigma_{23} \end{bmatrix} \begin{bmatrix} \partial f_{t11}/\partial\sigma_{11} = 0.0 \\ \partial f_{t22}/\partial\sigma_{22} = 0.0 \\ \partial f_{t33}/\partial\sigma_{33} = 1.0 \\ \partial f_{t12}/\partial\sigma_{12} = 0.0 \\ \partial f_{t13}/\partial\sigma_{13} = 0.0 \\ \partial f_{t23}/\partial\sigma_{23} = 0.0 \end{bmatrix} \tag{E.39}$$

$$D = T_{mod} + \begin{bmatrix} \alpha_1 & \alpha_2 & \alpha_2 & 0 & 0 & 0 \\ \alpha_2 & \alpha_1 & \alpha_2 & 0 & 0 & 0 \\ \alpha_2 & \alpha_2 & \alpha_1 & 0 & 0 & 0 \\ 0 & 0 & 0 & 2G & 0 & 0 \\ 0 & 0 & 0 & 0 & 2G & 0 \\ 0 & 0 & 0 & 0 & 0 & 2G \end{bmatrix} \begin{bmatrix} \partial g_{t11}/\partial\sigma_{11} = 0.0 \\ \partial g_{t22}/\partial\sigma_{22} = 0.0 \\ \partial g_{t33}/\partial\sigma_{33} = 1.0 \\ \partial g_{t12}/\partial\sigma_{12} = 0.0 \\ \partial g_{t13}/\partial\sigma_{13} = 0.0 \\ \partial g_{t23}/\partial\sigma_{23} = 0.0 \end{bmatrix} \begin{bmatrix} \partial f_{t11}/\partial\sigma_{11} = 0.0 \\ \partial f_{t22}/\partial\sigma_{22} = 0.0 \\ \partial f_{t33}/\partial\sigma_{33} = 1.0 \\ \partial f_{t12}/\partial\sigma_{12} = 0.0 \\ \partial f_{t13}/\partial\sigma_{13} = 0.0 \\ \partial f_{t23}/\partial\sigma_{23} = 0.0 \end{bmatrix} \tag{E.40}$$

The value of H_{mod}, S_{mod}, and T_{mod} can be calculated from the equation (E.10), equation (E.19), and equation (E.28). Therefore, by using assumptions from equation (E.36) and put it into equation (E.35), we have two equations with two unknowns ($\dot{\lambda}_s$ and $\dot{\lambda}_t$) as follows

$$\begin{aligned} \dot{\lambda}_s A + \dot{\lambda}_t B &= f_s(\sigma) \\ \dot{\lambda}_s C + \dot{\lambda}_t D &= f_t(\sigma) \end{aligned} \tag{E.41}$$

Some possible solutions of the equations (E.41) can be solved by certain condition as follows

$$\begin{aligned} &\text{if } f_s(\sigma) \geq 0.0 \text{ and } f_t(\sigma) \geq 0.0 \qquad \text{then} \\ &\qquad \dot{\lambda}_s = \frac{f_s(\sigma)D - f_t(\sigma)B}{AD - BC} \\ &\qquad \dot{\lambda}_t = \frac{f_t(\sigma)A - f_s(\sigma)C}{AD - BC} \end{aligned} \tag{E.42}$$

$$\begin{aligned} &\text{if } f_s(\sigma) \geq 0.0 \text{ and } f_t(\sigma) \leq 0.0 \qquad \text{then} \\ &\qquad \dot{\lambda}_s = \frac{f_s(\sigma)}{A} \\ &\qquad \dot{\lambda}_t = 0.0 \end{aligned} \tag{E.43}$$

$$\begin{aligned} &\text{if } f_s(\sigma) \leq 0.0 \text{ and } f_t(\sigma) \geq 0.0 \qquad \text{then} \\ &\qquad\qquad \dot{\lambda}_s = 0.0 \\ &\qquad\qquad \dot{\lambda}_t = \frac{f_t(\sigma)}{D} \end{aligned} \tag{E.44}$$

$$\begin{aligned} &\text{if } f_s(\sigma) < 0.0 \text{ and } f_t(\sigma) < 0.0 \qquad \text{then} \\ &\qquad\qquad \dot{\lambda}_s = 0.0 \\ &\qquad\qquad \dot{\lambda}_t = 0.0 \end{aligned} \tag{E.45}$$

E.4 Plastic corrections in principal stress base

The computation of the new stresses is made by adding to the old stress components the plastic correction part as follows:

$$\begin{aligned} \sigma_1^{new} &= \sigma_1^{old} - \lambda_t \alpha_2 + \lambda_s \Big(2G_e(\mathbf{G}_{11}) + \alpha_2 tr(\mathbf{G}) \Big) \\ \sigma_2^{new} &= \sigma_2^{old} - \lambda_t \alpha_2 + \lambda_s \Big(2G_e(\mathbf{G}_{22}) + \alpha_2 tr(\mathbf{G}) \Big) \\ \sigma_3^{new} &= \sigma_3^{old} - \lambda_t \alpha_1 + \lambda_s \Big(2G_e(\mathbf{G}_{33}) + \alpha_2 tr(\mathbf{G}) \Big) \end{aligned} \tag{E.46}$$

where G_e is the shear modulus and $\mathbf{G}$ is the derivation of the plastic potential of the shear mechanism with respect to stress tensor.

Appendix F

A parametric study in the boundary value problem

A parametric study is carried out to see the effect of some layer parameters on the behaviour of wallette throughout the diagonal compression test and pushover test. The main objective of this study is to investigate the impact of these parameters and how they affect the response of the calibrated homogeneous system. The parametric study was performed by changing parameters accounting in the plastic shear mechanism and plastic tensile mechanism.

F.1 Diagonal compression test

Table F.1 shows parameters that considered in the parametric study in the diagonal compression test. The references value are taken from the calibrated homogeneous system. The lower and upper value are taken considering the possible variability in the identification of the parameters.

Figure F.1 shows the result of the diagonal compression test by using three differents hardening parameter (A). According to Figure F.1, A gives small influence on the first peak and slightly at the second part of the curves. In general, the global impact is not significant in the diagonal compression test. Figure F.2 depict influence of the radius at failure R_{fail}. It is shown that the higher R_{fail} gives a more ductile responses and higher resistance. On the other hand the lower R_{fail} makes peak responses reached earlier. The role of α_s (Figure F.3) shows no effect at the first part of the curves, but it gives an impact at the second part of the curves.

In terms of tensile strength, Figure F.4 depict influence of tensile parameter T_{r}. As expected, T_{r} gives an important effect on the first peak in the diagonal compression test. This is due to the governing mechanism in the diagonal compression test which is tensile mechanism. Finally, variations on the tensile softening parameter α_t (Figure F.5) shows no effect in the global behaviour of the pushover test.

TABLE F.1: Parameters considered in the parametric study for diagonal compression test

Parameters	reference value	lower value	upper value
A	0.00013	0.00010	0.00016
R_{fail}	0.22	0.18	0.26
α_s	-0.0003	-0.0001	-0.0005
T_{r}	8%f_c	5%f_c	12%f_c
α_t	-0.5	-0.02	-1.0

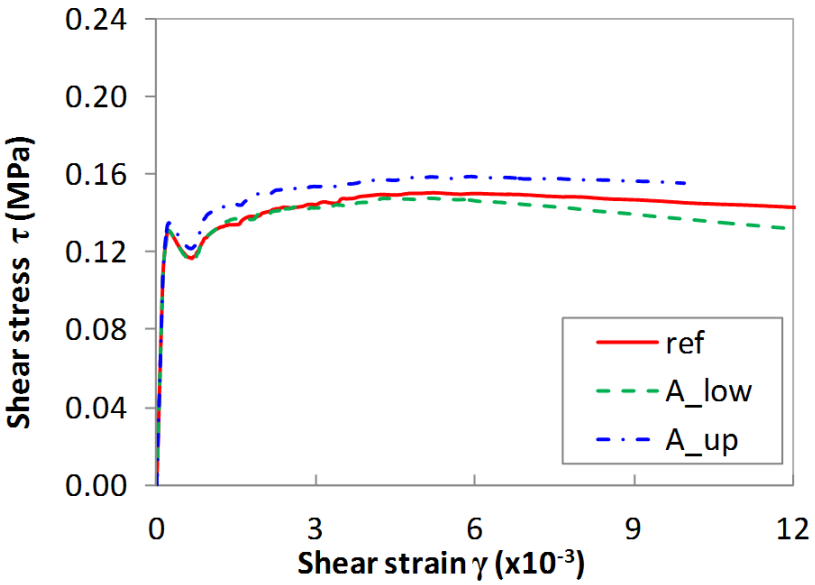

FIGURE F.1: Effect of the isotropic hardening parameter A in the diagonal compression test

Figure F.6 depict the non-dimensional measure of first peak in diagonal compression test (normalised by the first peak in the calibrated system (τ/τ_{ref})) compared with the non-dimensional parameters tested in the parametric study (normalised by the respective parameter of the calibrated system ($\mathrm{x}/\mathrm{x}_{\mathrm{ref}}$)). According to the Figure F.6, the parameter R_{fail}, T_{r}, and α_t are the parameters with the important impact in terms of the first peak in diagonal compression test. Similar results also found in [MOS+14] where compression strength, tensile strength, and tensile fracture energy are the parameters with the greatest influence on the maximum shear stress. Nevertheless, parameter A and α_s gives a little effect in terms of first

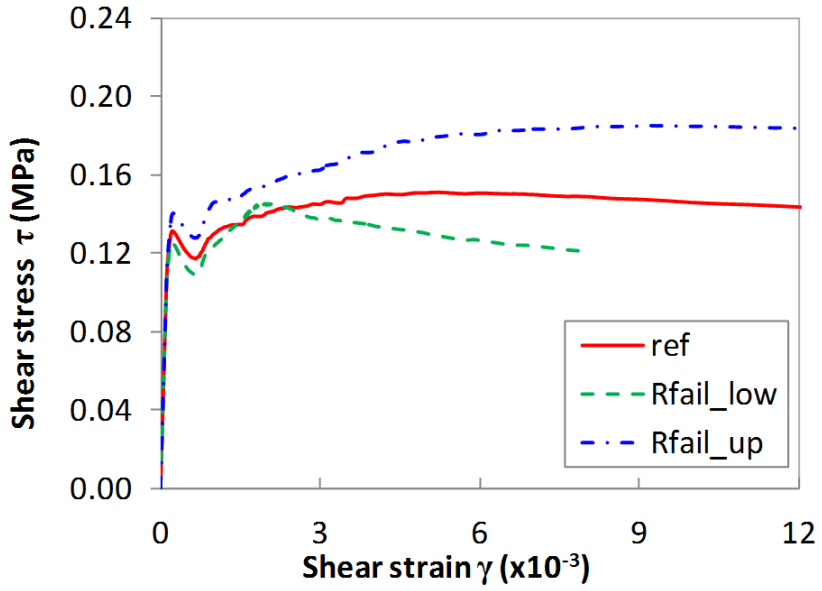

FIGURE F.2: Effect of the radius at failure R_{fail} in the diagonal compression test

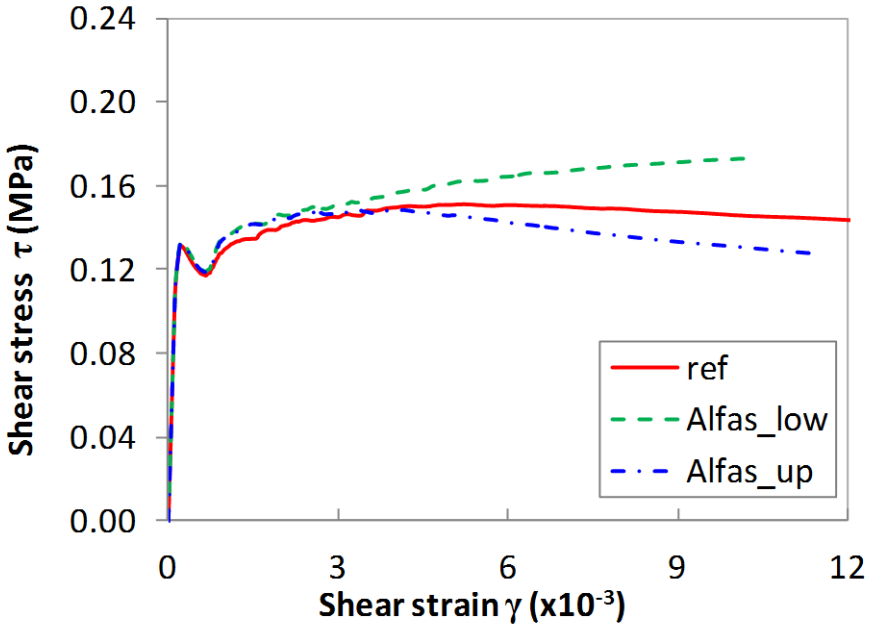

FIGURE F.3: Effect of shear softening parameter α_s in the diagonal compression test

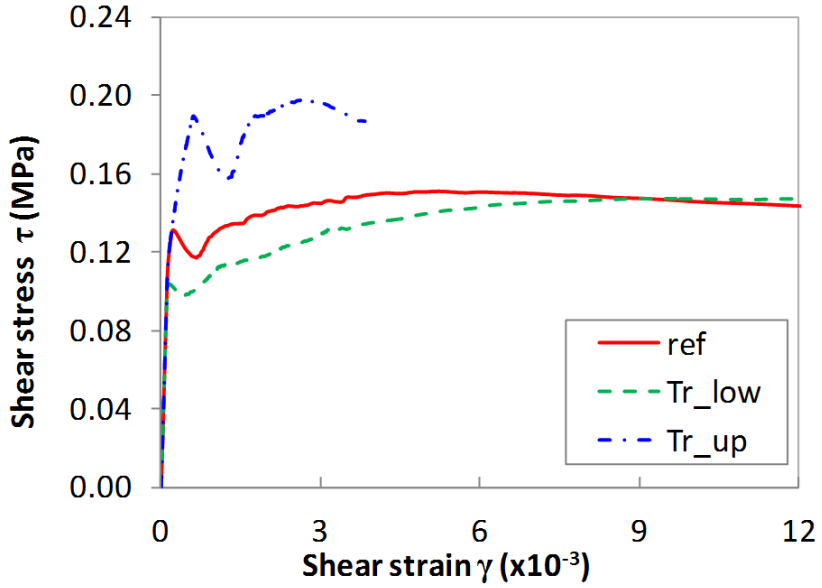

FIGURE F.4: Effect of tensile parameter T_r in the diagonal compression test

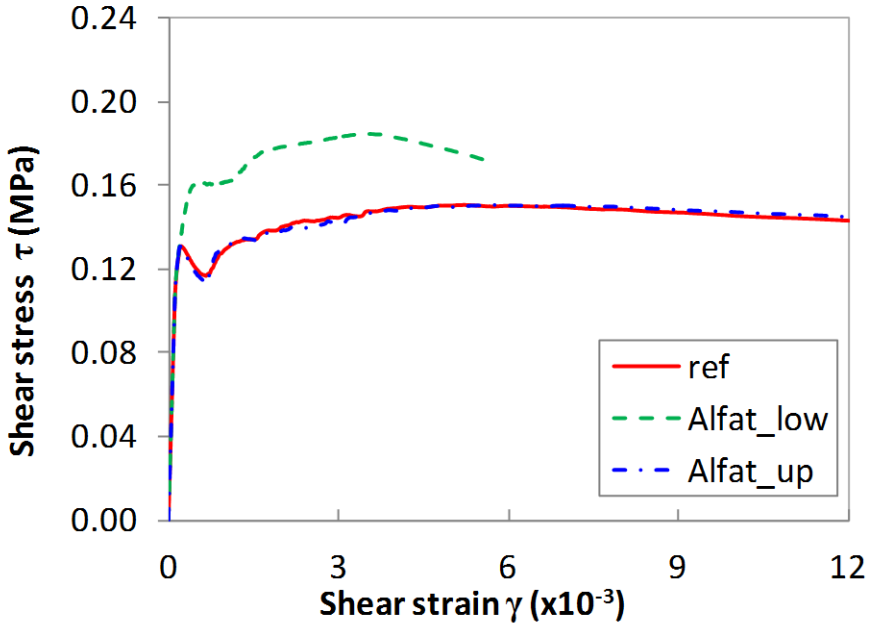

FIGURE F.5: Effect of tensile softening parameter α_t in the diagonal compression test

peak in the diagonal compression test.

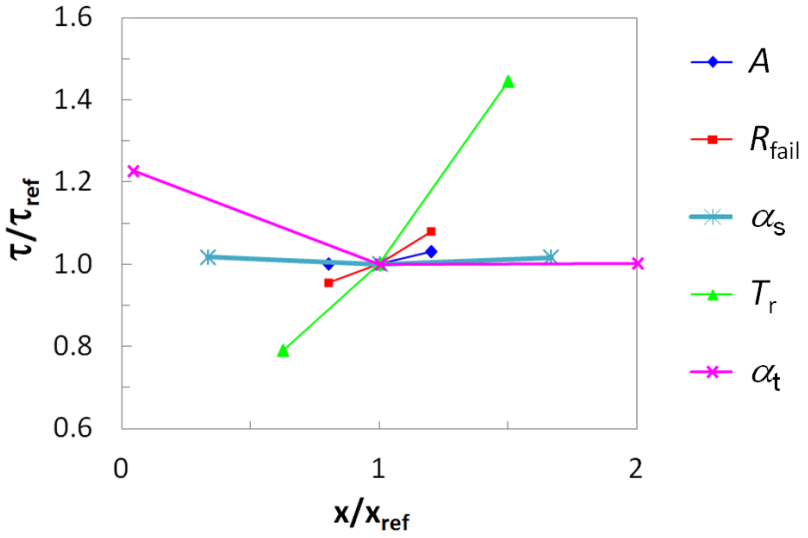

FIGURE F.6: Non-dimensional relationship between the maximum shear stress and the parameters assessed (x) for the homogeneous system in the diagonal compression test.

F.2 Pushover test

The next part is the parametric study on the pushover test. The reference parameters are taken from calibrated homogeneous system in the context of experiments from El Nabouch [EN17]. Table F.2 shows parameters considered in the parametric study in the pushover test.

TABLE F.2: Parameters considered in the parametric study for pushover test

Parameters	reference value	lower value	upper value
A	0.00013	0.00010	0.00016
R_{fail}	0.39	0.38	0.41
α_s	-0.0003	-0.0001	-0.0005
T_{r}	8%f_c	5%f_c	12%f_c
α_t	-0.5	-0.02	-1.0

Figure F.7 shows the result of pushover test by using differents hardening parameter A. It can be seen that A not gives significant impact in terms of maximum responses. Figure F.8 depict simulation with differents of the radius at failure R_{fail}. It is shown that the higher R_{fail} gives a higher resistance. Variations on the tensile softening parameters α_t (Figure F.11) shows essentially no effect. Figure F.10 depict influence of tensile parameter T_{r}. It is seen that from tensile strength of 5%fc to 8.0%fc indicate no effects. But, when T_{r} set equal to 12%fc, system failed at higher resistance. Finally, impact of α_s (Figure F.9) is negligible in the pushover test

Figure F.12 shows the non-dimensional maximum horizontal load in the pushover test (normalised by the maximum horizontal load of the calibrated system (H/H_{ref})) compared with the non-dimensional parameters tested in the parametric study (normalised by the respective parameter of the calibrated system (x/x_{ref})). According to the Figure F.12, the parameter R_{fail} and T_{r} are the parameters with important role on the maximum responses in the pushover test. On the other hand the A, α_s, and α_t showed little effect in terms of the maximum responses.

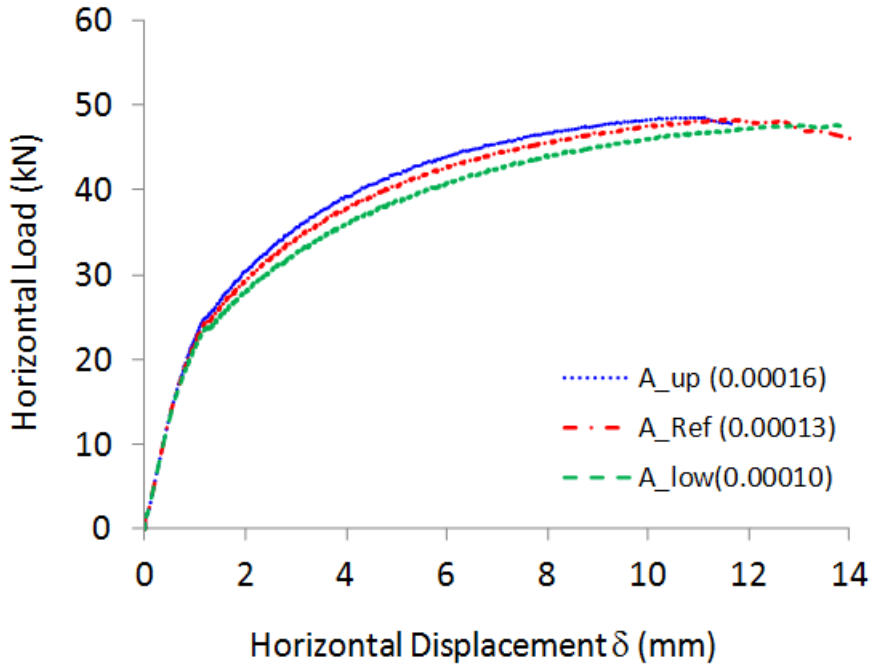

FIGURE F.7: Effect of the isotropic hardening parameter A in the pushover test

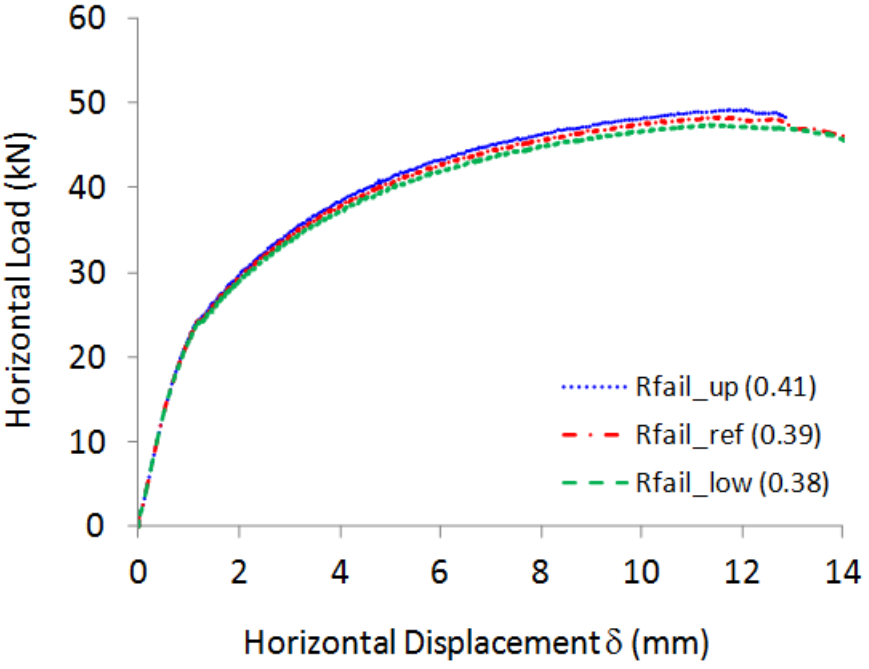

FIGURE F.8: Effect of the radius at failure R_{fail} in the pushover test

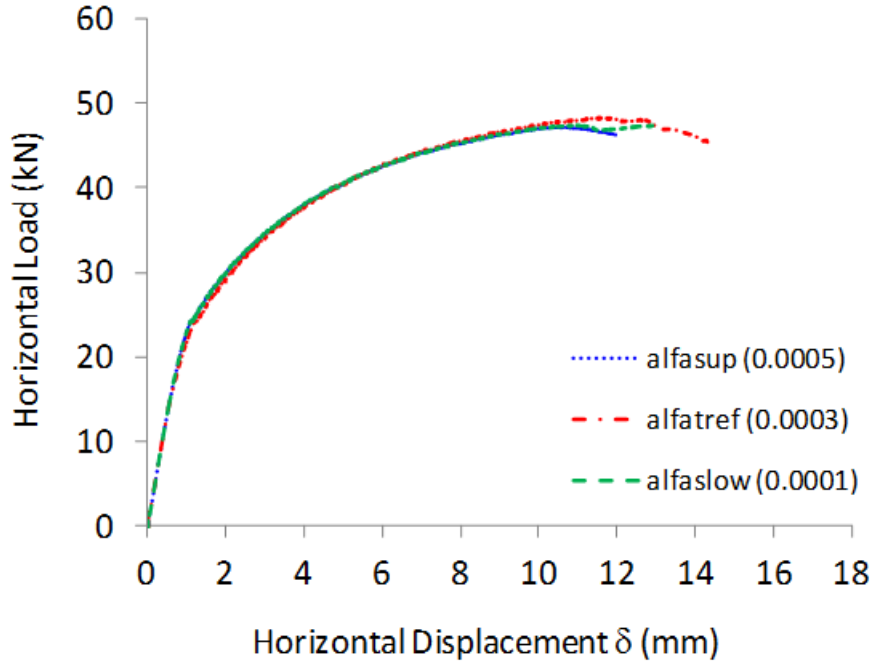

FIGURE F.9: Effect of shear softening parameter α_s in the pushover test

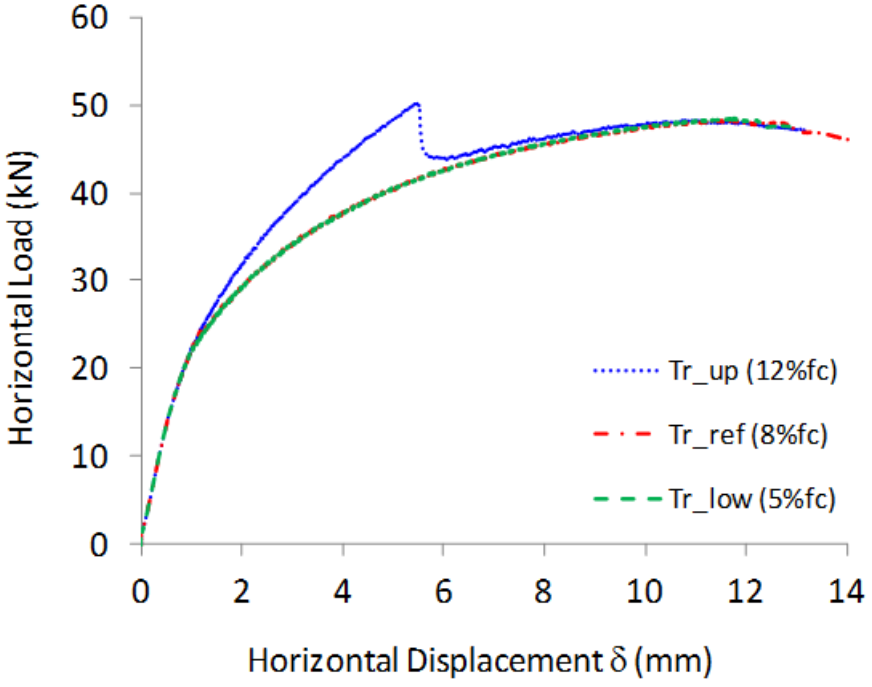

FIGURE F.10: Effect of tensile parameter T_r in the pushover test

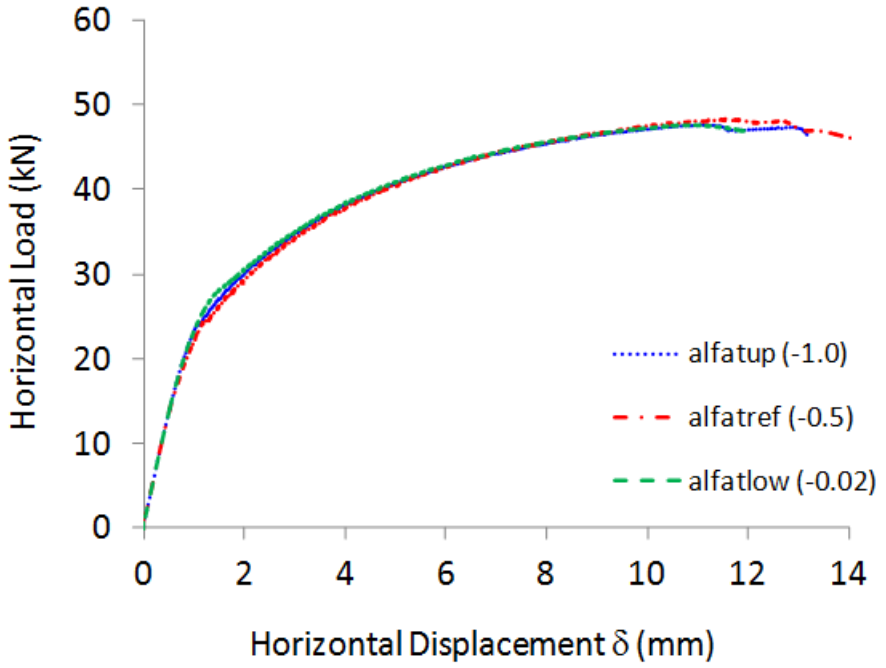

FIGURE F.11: Effect of tensile softening parameter α_t in the pushover test

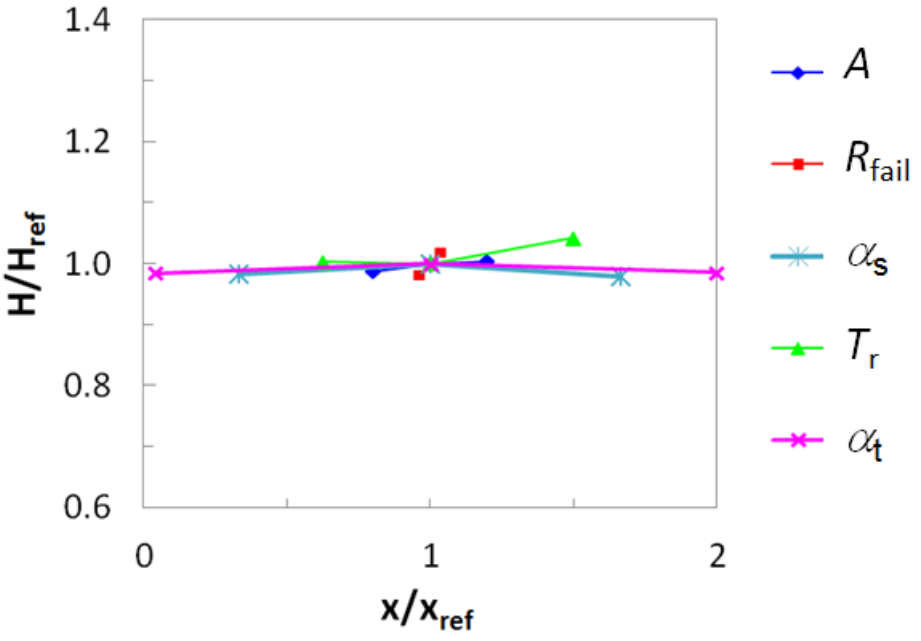

FIGURE F.12: Non-dimensional relationship between the maximum horizontal load and the parameters assessed (x) for the homogeneous system in the pushover test.

Bibliography

[AE02] ASTM-E-519. *Standard test method for diagonal tension (shear) in masonry assemblages*. West Conshohocken, 2002.

[AEY17] M.E. Arslan, M. Emiroglu, and A. Yalama. Structural behavior of rammed earth walls under lateral cyclic loading: A comparative experimental study. *Construction and Building Materials*, 133:433–442, 2017.

[AKS16] H. Araki, J. Koseki, and T. Sato. Tensile strength of compacted rammed earth materials. *Soils and Foundations*, 56(2):189–204, 2016.

[AS95] A.J. Abbo and S.W. Sloan. A smooth hyperbolic approximation to the mohr-coulomb yield criterion. *Computers & structures*, 54(3):427–441, 1995.

[Aur14] Patrimoine Aurhalpin. Inventaire participatif du pisé lyonnais. http://www.patrimoineaurhalpin.org/inventaire-participatif-du-pise-lyonnais/, 2014. Accessed: 2017-03-15.

[Bag11] Y. Bagagli. *Modélisation du comportement cyclique des sols et des interfaces sol-structure*. PhD thesis, Ecole Centrale de Lyon, 2011.

[BBLM14] T.T. Bui, Q.B. Bui, A. Limam, and S. Maximilien. Failure of rammed earth walls: from observations to quantifications. *Construction and Building Materials*, 51:295–302, 2014.

[BBLM16] T.T. Bui, Q.B. Bui, A. Limam, and J.C. Morel. Modeling rammed earth wall using discrete element method. *Continuum Mechanics and Thermodynamics*, 28(1-2):523–538, 2016.

[BM09] Q.B. Bui and J.C. Morel. Assessing the anisotropy of rammed earth. *Construction and building Materials*, 23(9):3005–3011, 2009.

[BMHM09] Q.B. Bui, J.C. Morel, S. Hans, and N. Meunier. Compression behaviour of non-industrial materials in civil engineering by three scale experiments: the case of rammed earth. *Materials and structures*, 42(8):1101–1116, 2009.

[BMHW14] Q.B. Bui, J.C. Morel, S. Hans, and P. Walker. Effect of moisture content on the mechanical characteristics of rammed earth. *Construction and Building Materials*, 54:163–169, 2014.

[BP04] Davide Bigoni and Andrea Piccolroaz. Yield criteria for quasibrittle and frictional materials. *International journal of solids and structures*, 41(11):2855–2878, 2004.

[BV10] TNO DIANA BV. *Diana User Manual-Material Library, Version 9.4*. Netherland, 2010.

[BXR91] Z.P. Bazant, Y. Xi, and S.G. Reid. Statistical size effect in quasi-brittle structures: I. is weibull theory applicable? *Journal of engineering Mechanics*, 117(11):2609–2622, 1991.

[CA13] D. Ciancio and C. Augarde. Capacity of unreinforced rammed earth walls subject to lateral wind force: elastic analysis versus ultimate strength analysis. *Materials and structures*, 46(9):1569–1585, 2013.

[CFM+16] F. Champiré, A. Fabbri, J.C. Morel, H. Wong, and F. McGregor. Impact of relative humidity on the mechanical behavior of compacted earth as a building material. *Construction and Building Materials*, 110:70–78, 2016.

[CG12] D. Ciancio and J. Gibbings. Experimental investigation on the compressive strength of cored and molded cement-stabilized rammed earth samples. *Construction and Building Materials*, 28(1):294–304, 2012.

[Che07] W.F. Chen. *Plasticity in reinforced concrete*. J. Ross Publishing, 2007.

[CJE89] B. Cambou, K. Jafari, and K. Elamrani. An elastoplastic model for granular material using three yielding mechanisms. numerical model in geomechanis. numog iii. proceeding of the 3rd international symposium at niagara falls, canada, 8-11 may 1989. *Elsevier Applied Science Publishers Limited*, 1989.

[CRA17] CRAterre. Le bâti en pisé : un patrimoine à préserver. http://www.leprogres.fr/lyon/2017/03/03/le-bati-en-pise-un-patrimoine-a-preserver, 2017. Accessed: 2017-03-15.

[CVAR07] U. Cicekli, G.Z. Voyiadjis, and R.K.A. Al-Rub. A plasticity and anisotropic damage model for plain concrete. *International Journal of plasticity*, 23(10):1874–1900, 2007.

[CWHM12] J.S.J. Cheah, P. Walker, A. Heath, and T.K.K.B. Morgan. Evaluating shear test methods for stabilised rammed earth. *Proceedings of Institution of Civil Engineers, Construction Materials*, 165(6):325–334, 2012.

[Dis16] Warren County Soil Water Conservation District. Get to know your soil. http://www.warrenswcd.com/education-connection-a-blog/category/earth, 2016. Accessed: 2017-07-14.

[Dru57] D.C. Drucker. A definition of stable inelastic material. Technical report, DTIC Document, 1957.

[DV15] J. Duriez and E. Vincens. Constitutive modelling of cohesionless soils and interfaces with various internal states: An elasto-plastic approach. *Computers and Geotechnics*, 63:33–45, 2015.

[Eas07] D. Easton. *The rammed earth house*. Chelsea Green Publishing, 2007.

[Ela92] K. Elamrani. *Contribution à la validation du modèle C. J. S. pour les matériaux granulaires*. PhD thesis, Ecole Centrale de Lyon, 1992.

[EN17] R. El Nabouch. *Mechanical behaviour of rammed earth under pushover tests*. PhD thesis, Universite de Savoie Mont Blanc, 2017.

[FH73] H.Y. Fang and T.J. Hirst. A method for determining the strength parameters of soils. *Highway Research Record*, 463(1973):45–50, 1973.

[Fig83] J.A. Figueiras. *Ultimate Load analysis of anisotropic and reinforced concrete plates and shells. Swansea*. PhD thesis, Department of Civil Engineering, University College of Swansea, 1983.

[GJ06] P. Grassl and M. Jirásek. Damage-plastic model for concrete failure. *International journal of solids and structures*, 43(22):7166–7196, 2006.

[Gra13] A.N. Gramlich. *A concise history of the use of the rammed earth building technique including information on methods of preservation, repair, and maintenance*. PhD thesis, University of Oregon, 2013.

[Haa09] V.G. Haach. *Development of a design method for reinforced masonry subjected to in-plane loading based on experimental and numerical analysis*. PhD thesis, Universidade do Minho, 2009.

[HC66] B.P. Hughes and G.P. Chapman. The complete stress-strain curve for concrete in direct tension. *Matls & Structures, Res & Testing/Fr/*, 1966.

[HGH94] H. Houben, H. Guillaud, and B.B. Hall. *Earth construction: a comprehensive guide*. Intermediate Technology Publications London, UK, 1994.

[Hil98] R. Hill. *The mathematical theory of plasticity*, volume 11. Oxford university press, 1998.

[Hol16] A. Holur. *Mechanical Testing Procedure for Local Building Materials: Rammed Earth and Laterite Building Stones*. PhD thesis, Ecole Nationale des Travaux Publics de l'Etat, 2016.

[Ita09] Itasca. *Fast Lagrangian Analysis of Continua in 3 Dimensions, Version 4.0*. Minneapolis, Minnesota, Itasca Consulting Group, 2009.

[JAGT09] P.A. Jaquin, C.E. Augarde, D. Gallipoli, and D.G. Toll. The strength of unstabilised rammed earth materials. *Géotechnique.*, 59(5):487–490, 2009.

[Jaq08] P.A. Jaquin. *Analysis of historic rammed earth construction*. PhD thesis, Durham University, 2008.

[JHPCG06] L. Jason, A. Huerta, G. Pijaudier-Cabot, and S. Ghavamian. An elastic plastic damage formulation for concrete: Application to elementary tests and comparison with an isotropic damage model. *Computer methods in applied mechanics and engineering*, 195(52):7077–7092, 2006.

[Jir11] M. Jirásek. Damage and smeared crack models. In *Numerical modeling of concrete cracking*, pages 1–49. Springer, 2011.

[JM05] M. Jirásek and S. Marfia. Non-local damage model based on displacement averaging. *International Journal for Numerical Methods in Engineering*, 63(1):77–102, 2005.

[JZ98] M. Jirásek and T. Zimmermann. Rotating crack model with transition to scalar damage. *Journal of engineering mechanics*, 124(3):277–284, 1998.

[Kea96] J. Keable. *Rammed earth structures: a code of practice*. Intermediate Technology, 1996.

[KJ69] I.D. Karsan and J.O. Jirsa. Behavior of concrete under compressive loadings. *Journal of the Structural Division*, 1969.

[KTN+08] J. Koseki, Y. Tsutsumi, K. Namikawa, S. Mihira, R. Salas-Monge, Y. Sano, and S. Nakajima. Shear and tensile properties of cement-treated sands and their application to mitigation of liquefaction-induced damage. In *Proceedings of the 4th International Symposium*

on Deformational Characteristics of Geomaterials, IS-Atlanta, pages 27–50, 2008.

[LF98] J. Lee and G.L. Fenves. A plastic-damage concrete model for earthquake analysis of dams. *Earthquake engineering & structural dynamics*, 27(9):937–956, 1998.

[LG72] P. Launay and H. Gachon. Strain and ultimate strength of concrete under triaxial stress. *Special publication*, 34:269–282, 1972.

[Maz86] J. Mazars. A description of micro-and macroscale damage of concrete structures. *Engineering Fracture Mechanics*, 25(5-6):729–737, 1986.

[McH84] P.G. McHenry. *Adobe and rammed earth buildings: Design and construction*. University of Arizona Press, 1984.

[MDC00] M. Maleki, P. Dubujet, and B. Cambou. Modélisation hiérarchisée du comportement des sols. *Revue Française de génie civil*, 4(7-8):895–928, 2000.

[MDM16] L. Miccoli, A. Drougkas, and U. Müller. In-plane behaviour of rammed earth under cyclic loading: experimental testing and finite element modeling. *Engineering Structures*, 125:144–152, 2016.

[MHG15] J. Mazars, F. Hamon, and S. Grange. A new 3d damage model for concrete under monotonic, cyclic and dynamic loadings. *Materials and Structures*, 48(11):3779–3793, 2015.

[MLGB13] J. Milosevic, M. Lopes, A.S. Gago, and R. Bento. Testing and modeling the diagonal tension strength of rubble stone masonry panels. *Engineering Structures*, 52:581–591, 2013.

[MMOW01] J.C. Morel, A. Mesbah, M. Oggero, and P. Walker. Building houses with local materials: means to drastically reduce the environmental impact of construction. *Building and Environment*, 36(10):1119–1126, 2001.

[MOS+14] L. Miccoli, D.V. Oliveira, R.A. Silva, U. Müller, and L. Schueremans. Static behaviour of rammed earth: experimental testing and finite element modelling. *Materials and Structures*, pages 1–14, 2014.

[MS88] A. Maji and S.P. Shah. Process zone and acoustic-emission measurements in concrete. *Experimental mechanics*, 28(1):27–33, 1988.

[MW03] V. Maniatidis and P. Walker. A review of rammed earth construction. Technical report, University of Bath, 2003.

[NBP+16] R.A. Nabouch, Q.B. Bui, O. Ple, P. Perrotin, C. Poinard, T. Goldin, and J.P. Plassiard. Seismic assesment of rammed earth walls using pushover tests. *Procedia Engineering*, 145:1185–1192, 2016.

[NM07] T. Namikawa and S. Mihira. Elasto-plastic model for cement-treated sand. *International journal for numerical and analytical methods in geomechanics*, 31(1):71–107, 2007.

[PDBBG98] R.H.J. Peerlings, R. De Borst, W.A.M. Brekelmans, and M.G.D. Geers. Gradient-enhanced damage modelling of concrete fracture. *Mechanics of Cohesive-frictional Materials*, 3(4):323–342, 1998.

[Póv91] R. Póvoas. *Non-linear models of analysis and design*. PhD thesis, University of Porto, 1991.

[Pur06] A. Purwodihardjo. *Modélisation des déformations différées lors du creusement des tunnels*. PhD thesis, Ecole Centrale de Lyon, 2006.

[Ric14] Ricola. herzog de meuron inaugurate ricola herb center in laufen. http://www.designboom.com/architecture/herzog-de-meuron-ricola-herb-center-krauterzentrum-07-07-2014/, 2014. Accessed: 2017-07-14.

[Sar15] I.P. Sarda. An isotropic damage model for geomaterials in the kratos framework. Master's thesis, UPC Barcelona Tech, 2015.

[Sax95] R.H. Saxton. Performance of cob as a building material. *Structural Engineer*, 73(7):111–115, 1995.

[SOM+13] R.A. Silva, D.V. Oliveira, T. Miranda, N. Cristelo, M.C. Escobar, and E. Soares. Rammed earth construction with granitic residual soils: the case study of northern portugal. *Construction and Building Materials*, 47:181–191, 2013.

[SOS+14] R.A. Silva, D.V. Oliveira, L. Schueremans, P.B. Lourenço, and T. Miranda. Modelling the structural behaviour of rammed earth components. In *Twelfth International Conference on Computational Structures Technology*, Stirlingshire, Scotland, 2014. Civil-Comp Press.

[TB12] J. Tejchman and J. Bobiński. *Continuous and discontinuous modelling of fracture in concrete using FEM*. Springer Science & Business Media, 2012.

[Ter80] M. Terrien. Emission acoustique et" comportement mecanique post-critique" d'un beton sollicite en traction. *Bulletin de liaison des laboratoires des ponts et chaussées*, (105), 1980.

[TFL08] P. Taylor, R.J. Fuller, and M.B. Luther. Energy use and thermal comfort in a rammed earth office building. *Energy and buildings*, 40(5):793–800, 2008.

[Tri10] Tripadvisor. Big gate with the rammed earth wall. https://www.tripadvisor.ca/LocationPhotoDirectLink-g181723d1073478-i67304825-NkMip Desert Cultural Centre Osoyoos Okanagan Valley British Columbia.html, 2010. Accessed: 2017-03-15.

[Uni58] *Manual on Stabilised Soil Construction for Housing*, 1958.

[VDB84] P.A. Vermeer and R. De Borst. Non-associated plasticity for soils, concrete and rock. 1984.

[WS13] B. Windstorm and A. Schmidt. A report of contemporary rammed earth construction and research in north america. *Sustainability*, 5(2):400–416, 2013.

[WW74] K.J. William and E.P. Warnke. Constitutive model for the triaxial behaviour of concrete. In *Concrete structures subjected to triaxial stress*, Bergamo,Italy, 1974.

[ZZLY02] W. Zhou, J. Zhao, Y. Liu, and Q. Yang. Simulation of localization failure with strain-gradient-enhanced damage mechanics. *International journal for numerical and analytical methods in geomechanics*, 26(8):793–813, 2002.

dernière page de la thèse

AUTORISATION DE SOUTENANCE

Vu les dispositions de l'arrêté du 25 mai 2016,

Vu la demande du directeur de thèse

Monsieur E. VINCENS

et les rapports de

M. P-Y. HICHER
Professeur - Ecole centrale de Nantes - GeM - Institut de Recherche en Génie Civil et Mécanique - 1 rue de la Noë - BP 92101 - 44321 Nantes cedex 3

et de

M. D. GALLIPOLI
Professeur - Université de Pau - Pays de l'Adour - Institut Supérieur Aquitain du Bâtiment et des Travaux Publics - allée du Parc Montaury - 64600 Anglet

Monsieur ADI RIYONO Winarputro

est autorisé à soutenir une thèse pour l'obtention du grade de **DOCTEUR**

Ecole doctorale MECANIQUE, ENERGETIQUE, GENIE CIVIL ET ACOUSTIQUE

Fait à Ecully, le 21 septembre 2017

P/Le directeur de l'E.C.L.
La directrice des Etudes

M-A. GALLAND

ECOLE CENTRALE DE LYON
Service Scolarité
ECULLY